

Exchange and superexchange interactions in quantum dot systems

Kuangyin Deng

Dissertation submitted to the Faculty of the
Virginia Polytechnic Institute and State University
in partial fulfillment of the requirements for the degree of

Doctor of Philosophy

in

Physics

Edwin Barnes, Chair

Sophia Economou

Jean J. Heremans

James Gray

January 27, 2021

Blacksburg, Virginia

Keywords: Quantum Computing, Quantum Dots, Spin Qubits, Exchange Interaction,
Superexchange, Configuration Interaction, Hubbard Model, Hund's Rule

Copyright 2021, Kuangyin Deng

Exchange and superexchange interactions in quantum dot systems

Kuangyin Deng

(ABSTRACT)

Semiconductor quantum dot systems offer a promising platform for quantum computation. And these quantum computation candidates are normally based on spin or charge properties of electrons. In these systems, we focus on quantum computation based on electron spins since these systems has good scalability, long coherence times, and rapid gate operations. And this thesis focuses on building a theoretical description of quantum dot systems and the link between theory and experiments.

In many quantum dot systems, exchange interactions are the primary mechanism used to control spins and generate entanglement. And exchange energies are normally positive, which limits control flexibility. However, recent experiments show that negative exchange interactions can arise in a linear three-dot system when a two-electron double quantum dot is exchange coupled to a larger quantum dot containing on the order of one hundred electrons. The origin of this negative exchange can be traced to the larger quantum dot exhibiting a spin triplet-like rather than singlet-like ground state. Here we show using a microscopic model based on the configuration interaction (CI) method that both triplet-like and singlet-like ground states are realized depending on the number of electrons. In the case of only four electrons, a full CI calculation reveals that triplet-like ground states occur for sufficiently large dots. These results hold for symmetric and asymmetric quantum dots in both Si and GaAs, showing that negative exchange interactions are robust in few-electron double quantum dots and do not require large numbers of electrons.

Recent experiments also show the potential to utilize large quantum dots to mediate superexchange interaction and generate entanglement between distant spins. This opens up a possible mechanism for selectively coupling pairs of remote spins in a larger network of quantum dots. Taking advantage of this opportunity requires a deeper understanding of how to control superexchange interactions in these systems. Here, we consider a triple-dot system arranged in linear and triangular geometries. We use CI calculations to investigate the interplay of superexchange and nearest-neighbor exchange interactions as the location, detuning, and electron number of the mediating dot are varied. We show that superexchange processes strongly enhance and increase the range of the net spin-spin exchange as the dots approach a linear configuration. Furthermore, we show that the strength of the exchange interaction depends sensitively on the number of electrons in the mediator. Our results can be used as a guide to assist further experimental efforts towards scaling up to larger, two-dimensional quantum dot arrays.

Exchange and superexchange interactions in quantum dot systems

Kuangyin Deng

(GENERAL AUDIENCE ABSTRACT)

Semiconductor quantum dot systems offer a promising platform for quantum computation. And these quantum computation candidates are normally based on spin or charge properties of electrons. In these systems, we focus on quantum computation based on electron spins since these systems has good scalability, long coherence times, and rapid gate operations. And this thesis focuses on building a theoretical description of quantum dot systems and the link between theory and experiments. A key requirement for quantum computation is the ability to control individual qubits and couple them together to create entanglement. In quantum dot spin qubit systems, the exchange interaction is the primary mechanism used to accomplish these tasks. This thesis is about attaining a better understanding of exchange interactions in quantum dot spin qubit systems and how they can be manipulated by changing the configuration of the system and the number of electrons. In this thesis, we show negative exchange energy can arise in large size quantum dots. This result holds for symmetric and asymmetric shape of the large dots. And we also provide a quantitative analysis of how large quantum dots can be used to create long-distance spin-spin interactions. This capability would greatly increase the flexibility in designing quantum processors built by quantum dot spins. The interplay of these systems with different geometry can serve as a guide to assist further experiments and may hopefully be the basis to build two-dimensional quantum dot arrays.

Dedication

To My Father

Acknowledgments

I would like to give special thanks to my great advisor Prof. Edwin Barnes sincerely. He has taught me how to face everything positively. I believe I will hold this altitude through all my life and deliver it to my future students as a legacy. In research, I have learned many approaches and skills from him. He has also taught me how to choose a good research topic and write a paper. Ed is truly patient to me about everything. For the problems in research, he can separate them nicely and explain step by step. For the language of the manuscripts I have written including this thesis, he has pointed my mistakes one by one and given suggestive advice. I truly enjoy the moments in the discussion of our research topics and new ideas. He is not just an advisor of my Ph.D. study and research, but also a guider for all my academic life.

I want to thank Prof. Sophia Economou for her kindness. Her encouragement makes me more confident, and her advice about my presentations of works helps me to gain plenty of skills and manners to deliver information. I also would like to thank my other committee members: Prof. Jean Heremans and Prof. James Gray. They have given a lot of helpful suggestions for my pre-defence presentation. I also enjoy the discussion about Weyl semimetals with Prof. Jean Heremans.

Prof. Tatsu Takeuchi have given so much help to me. I enjoy his class and the discussion afterward. I have learned many things in high energy physics from him. Prof. Djordje Minic has influenced me massively. His passion for physics has lighten my future academic road. I also would like to thank Prof. Lara Anderson for her course: general relativity. She has the magic power to create the best atmosphere for learning with interesting topics. Speaking of courses, I have enjoyed the classes taught by Prof. Eric Sharpe, Prof. Uwe Tauber and Prof.

Shengfeng Cheng, and I thank them for the interesting discussions.

On one hand, I would like to give my thanks to my collaborators in Virginia Tech: Prof. Nicholas J. Mayhall, Dr. Fernando A. Calderon-Vargas and Dr. John Van Dyke. They have helped me a lot with their expertise. I also enjoy the vivid discussions with them. On the other hand, I want to thank my collaborators in the University of Rochester: Prof. John M. Nichol and his group for their kindness. It was a good pleasure to visit their lab and discuss about our research.

I would like to thank my friends in Blacksburg for the good moments together. Juntao Wang, Mi Yan and Bikun Li are sincere friends who taught me a lot. I thank Arian Vezvaeae, Wenzhen Dong, Junkai Zeng, Xinfeng Xu, Shannon Serrao, Andy Andis, Hao Zou, Deheng Song, Chen Sun and Wei Gu for the chance learning and sharing ideas together. I also want to thank Fan Zhang, Zijian Jiang, Zhangjie Qin, Chuanhui Chen, Mengsu Chen, He Feng, George Barron, Fei Zhuang and Linhua Zhu for making my life better in Blacksburg.

I want to give my very special thanks to my girlfriend Giorgia Guaglianone for all the moments we have shared together. Even when we are far away in distance, her support can always make me stronger. Year 2020 is particularly hard for everyone, I truly thank her for the companion in this hardest time.

I would like to thank my friends in China. I thank Jie Zhou and Yiran Shen for the best friendship since our middle school. They have been always supportive no matter in my academic career or personal life. I also want to thank my friends Jiangtao Li, Changqing Wang, Guo Chen and Siqi Liao for sharing the enjoyable moments.

Finally, I would like to thank my family for all the love I have received since the very beginning of my life.

Contents

List of Figures	xi
List of Tables	xxii
1 Introduction	1
1.1 Motivation	1
1.2 Outline	3
1.3 Publication List	4
2 Quantum dot systems	5
2.1 Quantum computing and quantum dot systems	5
2.2 Quantum dot spin systems for quantum simulation	9
2.3 Spin qubits in quantum dot systems	11
2.4 Singlet-triplet exchange energy	14
3 Many-particle theory and experimental controls in quantum dots	18
3.1 Single particle in one quantum dot	18
3.2 Building many particle states	22
3.2.1 Cholesky decomposition	22

3.2.2	Slater-Condon rules for many particle states	24
3.3	From a generic Hamiltonian to the Heisenberg model	27
3.3.1	Ferromagnetic couplings	28
3.3.2	From the tight-binding model to the Heisenberg model	28
3.4	An experiment: Controlling the exchange coupling in a Heisenberg chain	30
4	Negative exchange energy in quantum dots	37
4.1	Introduction	37
4.2	The negative exchange energy experiment	40
4.3	Hubbard model and Hund's rule	41
4.4	Configuration interaction for a multielectron quantum dot	49
4.4.1	Frozen-core approximation	49
4.4.2	Full configuration interaction for a four-electron dot	53
4.5	Full configuration interaction with elliptical potential	53
4.6	Conclusions	55
5	Interplay of exchange and superexchange in triple quantum dots	57
5.1	Introduction	57
5.2	Quantum dot model and exchange energy for double dot	61
5.3	Triangular triple dot with two electrons	65
5.4	Triangular triple dot with four electrons	69

5.5	Linear triple dot with four electrons	75
5.6	Conclusions	82
6	Summary and outlook	84
	Bibliography	88
	Appendices	104
	Appendix A Single-particle densities and mediator detuning values	105
A.1	Triangular triple dot with two electrons (case 2)	105
A.2	Triangular triple dot with four electrons (case 3)	106
A.3	Linear triple dot with four electrons (case 4)	106

List of Figures

2.1	A quantum dot connecting source and drain for (a) a lateral system and (b) a vertical system. The current I could be measured depending on the gate voltage V_G and bias voltage V_{SD} . Adapted from Ref. [1].	7
2.2	Quantum dot with low bias. (a) When the chemical potential of N electrons is not in the range of the bias window $\mu_S \sim \mu_D$, the system can only contain $N-1$ electrons due to Coulomb blockade. (b) When the chemical potential of N electrons is in the bias window, the dot can be filled with $N-1$ or N electrons, which leads to current flow. (c) The current versus gate voltage change. Whenever the chemical potential of the dot μ (controlled by gate voltage V_G) lies in the range of the bias window, there is a current flowing from source to drain. Adapted from Ref. [1].	8
2.3	Quantum dot with high bias. (a) In the bias window, there are not just ground state for N electrons, but also one excited state. Electrons can tunnel through two paths, the ground state and the excited state. (b) The ground state of N and $N+1$ electrons are both in the bias window. Two electrons can tunnel through at the same time to form double-electron tunnelling current. Adapted from Ref. [1].	9

2.4 Measurement of exchange energy in a two-dot system. Detuning ε is defined as the chemical potential difference of the two dots. (A) The process of the experiment. (B) The spectrum as a function of the detuning ε . (C) Reading exchange energy from the strength of the out-of-plane magnetic field B . (D) The zooming up of (B) for negative detunings and a very small magnetic field difference is applied to two dots causing the eigenstates to be $|\uparrow\downarrow\rangle$ and $|\downarrow\uparrow\rangle$ for very negative ε . At $t < 0$ we prepare a singlet in the right dot. At $t = 0$, we adjust the detuning ε adiabatically to any point less than 0, which is the point we want to get the exchange energy for. Do this sweep each time with different magnetic field to scan. Then we wait for the system to evolve for time $t = \tau_S$. In this time interval, a leakage would happen only when the testing point is around the crossing of the $|S\rangle$ and $|T_+\rangle$ states due to the fact that the hyperfine interaction can flip the spins in the dots. After $t = \tau_S$ we change the detuning adiabatically back to the $\varepsilon > 0$ region to get the $(0, 2)$ configuration again. And we test the return probability of the singlet part of $(0, 2)$. If the evolution happens at the crossing point, the leakage will cause the return probability to be significantly less than 1, which can be read from the low probability curve in (C). Therefore, the magnetic field strength of the yellow curve in (C) can be mapped into the magnitude of the exchange energy J_{ex} for any detuning we choose in the ε region. Adapted from Ref. [1]

17

3.1	The exchange procedure. For triplet states including $ T_{\pm}\rangle$ and $ T_0\rangle$, the Pauli exclusion principle prevents hopping. However, for a singlet state, it is allowed for an electron to hop into the neighboring site. The left electron can hop virtually into the right dot and give rise to Coulomb interaction. And the original right electron can hop into the left site. These three processes combine to generate the exchange coupling $J = \frac{t^2}{U}$	29
3.2	(a) Scanning electron micrograph of the quadruple quantum dot device. The upper two plunger gates are sensor quantum dots not shown explicitly. The scale bar is 200 nm. (b) Measured exchange oscillations with virtual barrier gate $B_3 = 30$ mV. Inset: Absolute value of the fast Fourier transform of data shown in (b). As B_2 increases, J_3 decreases.	32
3.3	Electrostatic simulations. (a) Linecuts of the simulated potential associated with dots 2 and 3 vs. the barrier voltage pulse B_2 . The left dip is the potential of dot 2, and the right dip is the potential of dot 3. The dots move closer together as B_2 increases. The dashed lines are guides to the eye. (b) Fitted parameters of the simulated double-dot potential vs. B_2 . Based on the simulated potential of dot 1 (not shown), we also find that dots 1 and 2 move farther apart during the sample pulse.	34
3.4	J_1 vs. B_j . (a) J_1 vs. B_1 . (b) J_1 vs B_2 , for $B_1 = 60$ mV. (c) J_1 vs. B_3 , for $B_1 = 60$ mV. The black data points in each panel are obtained from the fast Fourier transform of a dataset similar to Fig. 3.2(b). In (a)-(c), the dark blue line is the fit to the exponential model, and the light blue line is the fit to the HL model. Panels (d)-(f) show the difference between the fits and the data for the two models.	35

4.1 (a) Device and cartoon illustration. Two small and one large quantum dot with about 100 electrons. In the large dot the electron number is odd. (b) Charge diagram of the system. The experiment was implemented by tuning of the detunings ζ and ε , which alter the dot occupancies as shown. Every point on this path will be tested. (c) and (d) the experiment procedure illustration. We start from the state, in which we have two electrons in the left dot forming a singlet. We then change the detuning to let one electron jump into the middle dot (following the arrow labeled ζ) or the large dot (following the arrow labeled ε) and interact for time τ with the large quantum dot on the right. After the interaction, we change the detuning back to the preparation stage and measure the return probability. Adapted from Ref. [2]. 42

4.2 (a) The measured singlet return probability for different detunings and in-plane magnetic field. The black curve indicates the leakage, which is very similar to the process in Fig. 2.4(C). (b) The mapping to the energy from (a). For $\varepsilon < 0$, the effective exchange energy J between the middle and right dots is positive. But for $\varepsilon > 0$, this J becomes negative, which indicates that singlet $|\uparrow\rangle|S\rangle$ has higher energy than the triplet $|\uparrow\rangle|T_0\rangle$ for the middle and right dot. Adapted from Ref. [2]. 43

4.3 Illustration of the three dot system, where the L and M dots form a two-electron double quantum dot and R is the multielectron quantum dot. In the main text, we analyze the effective exchange interaction, J , between the middle (M) and right (R) quantum dots. 43

4.4	<p>(a) Schematic of the energy levels and charge configuration for the three-dot system. Here, ΔE_i is the difference between two orbitals on the multielectron quantum dot. The schematic only shows the tunnel coupling between the middle and right dot, where $t_{MR,N+1}$ and $t_{MR,N+2}$ are the tunneling amplitudes between the middle dot's single-orbital and the lowest two orbitals above the frozen core in the multielectron quantum dot. (b) Eigenenergy spectrum, calculated as a function of the detuning ϵ, for the three-dot system at the transition between $(1, 1, 2N + 1)$ and $(1, 0, 2N + 2)$ charge configurations. The eigenstates $D_{+1/2}\rangle$ ($D_{-1/2}\rangle$) and $Q_{+1/2}\rangle$ ($Q_{-1/2}\rangle$) are almost degenerate and the exchange energy J is the difference between the triplet-like state $D_{\pm 1/2}\rangle$ and the singlet-like state $D'_{\pm 1/2}\rangle$.</p>	47
-----	--	----

4.5	Exchange energy vs. frequency difference of the elliptical potential.	54
-----	---	----

5.1 Four different quantum dot configurations studied in this work. D1 and D2 are small dots about 12.5 nm in radius, which corresponds to a confinement energy of $\hbar\omega_0 = 7.28$ meV. The x -axis is defined to pass through the centers of both D1 and D2. D3 is the mediator quantum dot, which is taken to have a radius of about 17.5 nm, which corresponds to a confinement energy of $\hbar\omega_1 = \frac{1}{2}\hbar\omega_0 = 3.64$ meV. The y -axis passes through the center of D3. Here, we fix $2l_0 = 56$ nm for cases 1, 2 and 3. We distinguish different triangular geometries in cases 2 and 3 by angle α ; the distance between the mediator and small dots, l_1 , is a function of α . The blue dashed lines in every case are the potential separation lines described in the main text. (a) The two-dot system. J_{12} is the exchange coupling between two dots, which are separated by $2l_0$. (b) The triangular system with two electrons. We adjust the detuning Δ to keep D3 empty. (c) The triangular system with four electrons. We confine two electrons in the big dot by adjusting the detuning parameter Δ . (d) Linear three-dot with four electrons. This can be thought of as a limit of case 3 in which we fix l_1 and rotate the two small dots D1 and D2 with respect to D3 until they are on a line. l_1 in this case is still a function of α as in case 3, and we also use α to adjust the inter-dot separation in this case. 59

(a)	Case 1	59
(b)	Case 2	59
(c)	Case 3	59
(d)	Case 4	59

5.2	(a) Exchange energy for two quantum dots with one electron each (see Fig. 5.1(a)) computed from CI as a function of the number L of single-particle orbitals ($L/2$ orbitals for each dot). Full orbital shells on each dot are retained when $L = 6, 12, 20$. (b) Exchange energy for two dots versus inter-dot half-distance l_0 from a CI calculation with $L = 12$ single-particle basis states.	63
-----	--	----

(a)	Exchange energy versus number L of single-particle orbitals used in CI calculation for two electrons in a double quantum dot.	63
-----	---	----

(b)	Exchange energy versus inter-dot half-distance l_0	63
-----	--	----

5.3	Single-particle density for two electrons in a triangular triple dot (case 2) for $\alpha = 30^\circ$. The upper (lower) panel shows the single-particle density for the lowest-energy singlet $ S\rangle$ (triplet $ T_0\rangle$). The yellow dashed line is the potential cut at $y = y_0$. The dashed circles mark the positions of the three parabolic dot potentials for this value of α . It is apparent that the centers of the electron density in the small dots are displaced downward. This is due to the large value of detuning Δ chosen to deplete the big dot. The distance between the two small dots remains the same, as does the normal exchange coupling between them.	66
-----	---	----

5.4	Effective exchange interaction between electrons on dots D1 and D2 as a function of angle α (see Fig. 5.1(b)) in the case of two electrons in a triangular triple dot (case 2). In the CI calculation used to obtain this result, we retain 6, 6 and 3 orthonormalized Fock-Darwin orbitals for D1, D2 and D3, respectively, corresponding to a total of $L = 15$ single-particle basis states. The red dashed line is the result for J_{12} from case 1 (two electrons in a double dot) using 12 single-particle orbitals. We see only modest contributions from superexchange processes in this case.	67
5.5	Single-particle density for four electrons in a triangular triple dot (case 3) with $\alpha = 30^\circ$. The upper (lower) panel shows the single-particle density for the lowest-energy singlet-like $ S\rangle$ (triplet-like $ T_0\rangle$) four-electron state. The yellow dashed line marks the potential cut at $y = y_0$. The blue dashed circles indicate the original positions of the three dots for this value of α . The electrons in the small dots are displaced slightly downward and outward, while the electrons in the big dot move upward due to Coulomb repulsion.	70
5.6	(a) Effective exchange energy J_{12} versus angle α for four electrons in a triple quantum dot as in Fig. 5.1(c) (case 3). Results are obtained from a CI calculation in which 6, 6 and 3 orbitals are retained for D1, D2 and D3, respectively, for a total of $L = 15$ single-particle basis states. Superexchange processes strongly enhance J_{12} for $\alpha < 65^\circ$. (b) A zoom-in of (a), along with the CI result for two electrons in a double dot (case 1) when $L = 12$ single-particle states are kept (red dashed line). The dip in J_{12} near $\alpha = 70^\circ$ is likely caused by Coulomb repulsion as explained in the text.	73
(a)	Effective exchange energy for triangular triple dot with four electrons.	73

(b)	Zoom-in of panel (a)	73
5.7	Single-particle density for four electrons in a linear triple dot (case 4) with $\alpha = 30^\circ$. The upper (lower) panel shows the single-particle density for the lowest-energy singlet-like $ S\rangle$ (triplet-like $ T_0\rangle$) four-electron state. The yellow dashed lines mark the potential cuts at $x = \pm x_0$. The blue dashed circles indicate the positions of the three dots for this value of α . The electrons in the small dots are displaced slightly outward due to Coulomb repulsion. . . .	76
5.8	(a) Effective exchange energy J_{12} versus inter-dot separation (given by $2l_1 = 2l_0 \sec \alpha$, with $l_0 = 28$ nm) for four electrons in a linear triple dot as in Fig. 5.1(d) (case 4). Results are obtained from a CI calculation in which 6, 6 and 3 orbitals are retained for dots D1, D2 and D3, respectively, for a total of $L = 15$ single-particle basis states. The presence of the two mediator electrons strongly enhances J_{12} for $\alpha < 65^\circ$. (b) A zoom-in of (a). In the large-distance regime (large α and l_1), J_{12} monotonically approaches zero. . .	77
(a)	Effective exchange energy for linear triple dot with four electrons. . .	77
(b)	Zoom-in of panel (a)	77

5.9	Calculation of the vertical shift in electron positions due to Coulomb repulsion in case 3 (triangular triple dot) using the exchange energy from case 4 (linear triple dot). We assume the electrons in D1 and D2 remain fixed and only consider the movement of electrons in D3. (a) Effective exchange energy versus α and l_1 for case 4. Green diamonds are the original data from Fig. 5.8. The blue line is an interpolating function for lower angles to intermediate angles. One can map the data of case 3 to this function to get information about the shifts in electron positions as explained in the main text. (b) The resulting angular shifts due to Coulomb repulsion for different angles α . (c) The relative change in vertical position of the electrons in D3 for different angles.	78
(a)	Interpolating function for effective exchange in case 4.	78
(b)	Effective angular shifts for case 3.	78
(c)	Relative electron position shifts for case 3.	78
A.1	Single-particle density plots for the triangular triple dot with two electrons (case 2) for $\alpha = 30^\circ, 40^\circ, 45^\circ, 50^\circ, 60^\circ, 70^\circ$ and for the lowest-energy singlet-like (S) and triplet-like (T) states. The white and blue dashed circles indicate the dot potentials, and the yellow dashed line is the potential cut (here we do not show the $x = 0$ cut in the plots). The big dot contains approximately zero electrons. At low angles, the two small dots move a little bit downward due to the large detuning of the big dot. At high angles, this effect is small because the dots are sufficiently far apart.	108

A.2	Single-particle density plots for the triangular triple dot with four electrons (case 3) for $\alpha = 30^\circ, 40^\circ, 45^\circ, 50^\circ, 60^\circ, 70^\circ$ and for the lowest-energy singlet-like (S) and triplet-like (T) states. The white and blue dashed circles indicate the dot potentials, and the yellow dashed line is the potential cut (here we do not show the $x = 0$ cut in the plots). In each case, the big dot contains two electrons as can be confirmed by integrating the density over the upper region. The position shifts of the electrons in the big dot are significantly larger for smaller angles compared to larger angles, which confirms the results obtained in Sec. 5.5 and Fig. 5.9.	109
A.3	Single-particle density plots for the linear triple dot with four electrons (case 4) for $\alpha = 30^\circ, 40^\circ, 45^\circ, 50^\circ, 60^\circ, 70^\circ$ and for the lowest-energy singlet-like (S) and triplet-like (T) states. The blue dashed circles indicate the dot potentials, and the yellow dashed lines are the potential cuts. The big dot contains two electrons as can be confirmed by integrating the density over the middle region.	110

List of Tables

4.1	Ground states (S=Singlet and T=Triplet) for different dot sizes and number of electrons. Here, $\hbar\omega_0 = 1.0\text{meV}$ for both GaAs and Si quantum dots. . . .	52
(a)	Ground states table for GaAs.	52
(b)	Ground states table for Si.	52

List of Abbreviations

CI Configuration Interaction

FCA “Frozen Core” Approximation

FD Fock-Darwin

HL Heitler-London

HM Hund-Mulliken

OB Orthonormal Basis

Chapter 1

Introduction

1.1 Motivation

Here we briefly talk about the motivation of exploring exchange energy in quantum dot spin systems. We will leave the detailed introduction of semiconductor quantum dot spin systems to the next chapter.

Recently, quantum computation has become a blooming field due to its potential to solve some specific problems classical computers cannot solve. In quantum computation, information is in the form of qubits. Unlike bits in a classical computer, qubits can be implemented as superposition of many quantum states and the new states should be treated completely new. In these decades, people have found many systems as candidates for quantum computation. A quantum dot system is one of them [1, 3] and this is also the main focus of this thesis.

In a quantum dot system, one may use spins of electrons to encode qubits. One can encode several kinds of spin states as qubits as we will mention in the next chapter. Here we focus on two-electron qubits: singlet-triplet qubits. Considering a qubit formed by a singlet and triplet spin states, one can define exchange energy as the difference of these two states

$$J_{ex} = E_T - E_S, \tag{1.1}$$

where T and S represent triplet and singlet states, respectively. This exchange energy can be used to manipulate the states on the Bloch sphere [1]. For two electrons in a confining potential, the exchange energy can be positive or negative if there is a sufficiently strong magnetic field [4, 5, 6, 7, 8]. For example, it has been shown that the ground state oscillates between a singlet and a $S_z = 0$ triplet as the magnetic field strength is tuned, even in the absence of spin-orbit coupling [4, 7]. On the other hand, negative exchange is harder to achieve in weak magnetic fields due to the well-known two-electron ground state theorem [9, 10], although it has been shown to be possible in double quantum dot systems if there is a strong bias between the dots [8]. The difficulty in realizing negative exchange in the low-field, low-bias regime in turn limits the types of control schemes that can be employed to perform logic gates or dynamical decoupling [11, 12, 13].

However, it has been shown in recent experiments that the behavior of the exchange energy can be very different if there is a big multielectron quantum dot in the system [2, 14, 15]. These experiments reported negative exchange energies due to contributions from electrons in the higher orbitals of the big quantum dot. The existence of negative exchange energy in quantum dot systems not only opens a possibility to control the system more efficiently but also is interesting to understand in its own rights. Therefore, in this thesis we will review the theory of quantum dots and explain the underlying physical mechanisms behind the experiments. Moreover, we will use a method called configuration interaction (CI) to understand in which cases negative exchange could arise in quantum dot systems.

After understanding the physics of systems comprised of several dots, one may imagine building a two dimensional array of quantum dots by coupling single or double quantum dot systems. To reach this goal, one needs to understand how exchange interactions depend on the geometry of a quantum dot system distributed in two dimensions. Thus, in the last part of this thesis, we talk about the interplay of exchange and superexchange in triple quantum

dot systems.

1.2 Outline

In this thesis, we begin by presenting the basics of quantum dot spin systems in Chapter 2. This includes talking about quantum computing and quantum dot systems, introducing different kinds of spin qubits and zooming in on singlet-triplet qubits and exchange energy.

In Chapter 3, we review the theoretical description and some experimental controls of quantum dot systems. We start this chapter by considering a single electron in one quantum dot and introducing Fock-Darwin states as a basis of the system. After that, we build many particle states from Fock-Darwin states by utilizing Slater-Condon rules. Furthermore, we build a generic Hamiltonian and show how one can get a Heisenberg model from this Hamiltonian. Lastly, we talk about some experimental controls of exchange energy in several-quantum-dot systems using the Heisenberg model and my work in building the models.

In Chapter 4, we first introduce the recent experiments on triple quantum dot systems with many electrons showing that negative exchange energy arises. Secondly, we will describe my theoretical efforts to explain these experiments. Thirdly, we explore the system with only one large quantum dot and show that only several electrons are needed to have negative exchange energy.

In Chapter 5, we use a large quantum dot as a mediator and examine different dot geometries. In these systems we study the effective exchange and superexchange energy between small dots and mediated by the large quantum dot.

In Chapter 6, we summarize this whole thesis and discuss the potential impact of this work on future theoretical and experimental research on quantum dot spin systems.

1.3 Publication List

1. **Kuangyin Deng**, F. A. Calderon-Vargas, Nicholas J. Mayhall, and Edwin Barnes. “Negative exchange interactions in coupled few-electron quantum dots.” *Phys. Rev. B* **97**, 245301 (2018).
2. Haifeng Qiao, Yadav P. Kandel, **Kuangyin Deng**, Saeed Fallahi, Geoffrey C. Gardner, Michael J. Manfra, Edwin Barnes, and John M. Nichol. “Coherent Multispin Exchange Coupling in a Quantum-Dot Spin Chain.” *Phys. Rev. X* **10**, 031006 (2020).
3. **Kuangyin Deng** and Edwin Barnes. “Interplay of exchange and superexchange in triple quantum dots.” *Phys. Rev. B* **102**, 035427 (2020).

Chapter 2

Quantum dot systems

In this chapter, we introduce quantum dot spin systems as a way of realizing quantum computation. We briefly talk about quantum simulations in them and we review several ways of encoding qubits in one or more electron spins.

2.1 Quantum computing and quantum dot systems

Progress in developing and improving classical computers has been ongoing for many decades. Engineers try to make the chips smaller and more condensed. However, current chips are approaching the scale where quantum effects begin to affect their behavior, limiting the ability to increase the density of transistors on a chip further. Therefore, a new understanding of computation at the quantum level is needed. On the other hand, there are well known problems that classical computers cannot solve because of exponential scaling of the problems. Although we cannot guarantee that at the quantum level, a given computation must be more efficient and powerful than classical computation, there are now many examples of quantum algorithms that are capable of solving problems much faster than any known classical algorithm. One famous example is prime factorization, which plays a key role in information security. However, this problem was proved solvable in polynomial time on quantum computers as shown by Peter W. Shor [16] in 1994. In thinking about the applications of quantum computers, it is useful to keep in mind the development of classical computers.

At the time classical computers were just created, people only expected computers to do calculations faster than humans. Over the last several decades, as the internet was developed, people discovered the power of classical computers is not only to calculate academic problems, but also to facilitate communication, searching and entertainment. For quantum computers, we know they can solve some problems that are beyond the reach of classical computers, and as time goes on more and more quantum algorithms are being discovered. This does not mean quantum computers are better than classical computers in doing all jobs. One should really view them as a different class of machines altogether. In the future, there may or may not be an innovation of quantum computers that makes them useful for aspects of everyday life that classical computers have already reached. However, what we are sure about is that once a universal quantum computer is built, there must be some areas of technological development that will be significantly impacted.

In classical computation, information is stored in bits, and one bit can be written as two states 0 or 1. This form of information is discrete, and more digits can make the stored information more accurate. On the other hand, in quantum computation, information is stored in qubits, and one qubit can be written as not only $|0\rangle$ or $|1\rangle$ but also any superposition of these two as a new state: $|\alpha\rangle = a|0\rangle + b|1\rangle$, where $|a|^2 + |b|^2 = 1$. Here $|0\rangle$ and $|1\rangle$ are two different quantum states serving as the computational basis. Thus, a quantum state can continuously span any direction between the two basis states.

There are a lot of schemes that can potentially be used as qubits [17, 18]. Specifically, quantum dot spin systems are one of them. Since the very first proposal by Loss and Divincenzo [3], quantum computation based on spin qubits has enjoyed rapid development in both experimental techniques and theory.

A quantum dot is an artificial structure which can be treated as an atom in the sense that it confines electrons. It will be normally connected to a source and drain. Thus, electrons

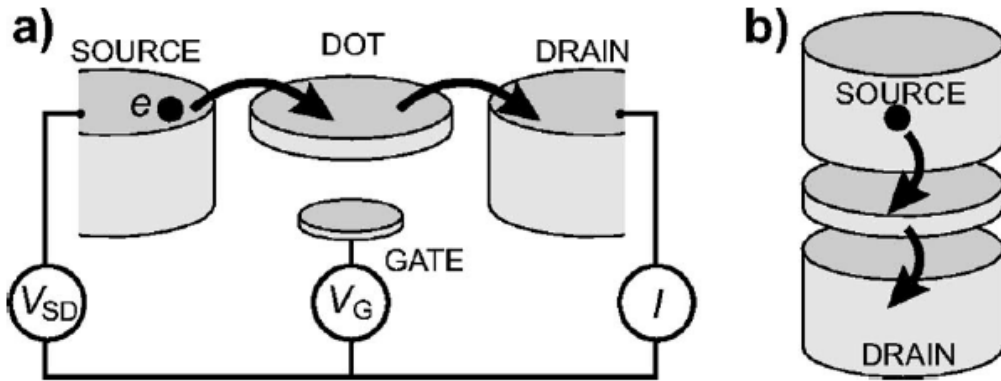


Figure 2.1: A quantum dot connecting source and drain for (a) a lateral system and (b) a vertical system. The current I could be measured depending on the gate voltage V_G and bias voltage V_{SD} . Adapted from Ref. [1].

or holes can be loaded into the dot by controlling the voltage. On the other hand, electron number can also be controlled by changing the chemical potential. As shown in Fig. 2.1, a quantum dot is connected to the source and drain from reservoirs. A current and bias voltage probe is attached to measure the electric properties. The dot is coupled by a gate with voltage V_G for chemical potential control.

A quantum dot can be fabricated in many different sizes and materials due to the fact that this is a very general structure [1]. In this thesis, we focus on semiconductor quantum dot systems such as GaAs and Si. The typical size of these kinds of dots normally ranges from 10 to 200 nm in diameter. Quantum dots provide a confinement potential to trap electrons. To realize quantum phenomena in GaAs quantum dots, they have to be cooled to temperatures well below 1 K.

The source and drain voltage bias V_{SD} and the gate voltage of the dot V_G can control the number of electrons. Here we show how this works in a single quantum dot. For multiple quantum dot systems, the control is similar. Now we consider a low bias window as shown in Fig. 2.2. In Fig. 2.2(a), the chemical potentials (also indicating the gate voltage V_G) $\mu(N)$ and $\mu(N-1)$ are both out of the range of the bias window $\mu_S \sim \mu_D$. Here Coulomb

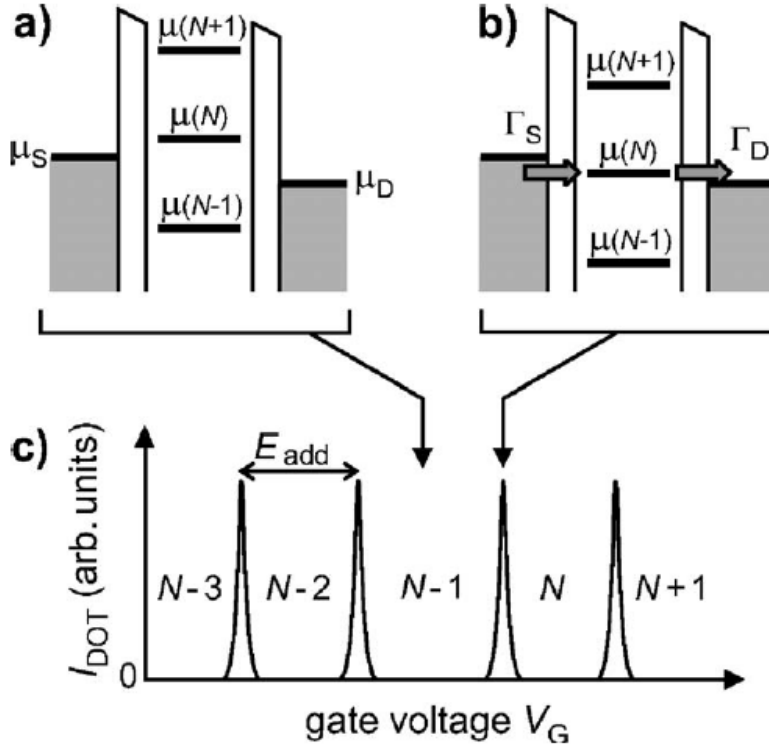


Figure 2.2: Quantum dot with low bias. (a) When the chemical potential of N electrons is not in the range of the bias window $\mu_S \sim \mu_D$, the system can only contain $N-1$ electrons due to Coulomb blockade. (b) When the chemical potential of N electrons is in the bias window, the dot can be filled with $N-1$ or N electrons, which leads to current flow. (c) The current versus gate voltage change. Whenever the chemical potential of the dot μ (controlled by gate voltage V_G) lies in the range of the bias window, there is a current flowing from source to drain. Adapted from Ref. [1].

blockade appears, forbidding the dot from having N electrons inside and locking the number of electrons to $N - 1$. Therefore, there is no current flowing from the source to the drain. In Fig. 2.2(b), the chemical potential obeys $\mu_S \geq \mu(N) \geq \mu_D$, which makes tunneling possible. When the dot is filled with $N - 1$ electrons, one more electron would hop into the dot to form a state with N electrons and soon this electron would tunnel into the drain to leave a state with $N - 1$ electrons again. This process results in a current flowing from source to drain. In Fig. 2.2(c), we show the current flow I_{DOT} as a function of gate voltage V_G . Currents only exist when the chemical potential is in the bias window.

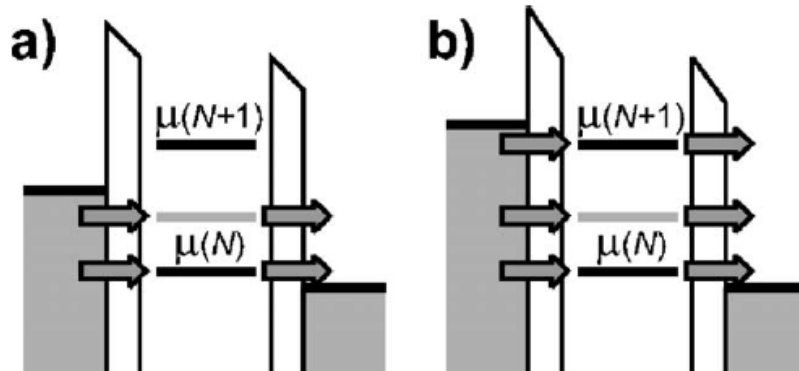


Figure 2.3: Quantum dot with high bias. (a) In the bias window, there are not just ground state for N electrons, but also one excited state. Electrons can tunnel through two paths, the ground state and the excited state. (b) The ground state of N and $N + 1$ electrons are both in the bias window. Two electrons can tunnel through at the same time to form double-electron tunnelling current. Adapted from Ref. [1].

On the other hand, when the quantum dot has a high bias V_{SD} , as shown in Fig. 2.3, things are different. In Fig. 2.3(a), the bias window contains the ground and the first excited state of N electrons, so that an electron has two paths to tunnel through the dot. This would change the current allowing us to perform energy spectroscopy of the excited states. When the bias is even higher, as Fig. 2.3(b) shows, the bias window could even cover the ground state with $N + 1$ electrons. This would lead to a double-electron tunnelling current. Experimentally, one can use this technique to identify the energy levels around the ground state for a given number of electrons, if one patiently finds the function mapping from the gate voltage V_G to the current I_{DOT} for any source-drain bias.

2.2 Quantum dot spin systems for quantum simulation

Quantum dot spin systems are not only just candidates for quantum computation, but also for the more specific task of quantum simulation. In condensed matter, understanding strongly correlated systems is still a major goal for both theorists and experimentalists.

Recently, a lot of experiments implementing quantum simulation on semiconductor quantum dots have been reported [19, 20, 21, 22, 23]. Thus quantum dot spin systems offer a new platform to realize strongly correlated systems based on controllable parameters. Here we only briefly talk about two examples of realizing some strongly correlated systems.

In Ref. [22], the authors used three lateral quantum dots to build up a simulator for the Coulomb blockade transition and the Mott metal-to-insulator transition. First, they proposed a single band Fermi-Hubbard model:

$$H = - \sum_i \epsilon_i n_i - \sum_{\langle i,j \rangle, \sigma} t_{ij} (c_{i\sigma}^\dagger c_{j\sigma} + h.c.) + \sum_i \frac{U_i}{2} n_i (n_i - 1) + \sum_{i,j} V_{ij} n_i n_j, \quad (2.1)$$

where ϵ_i is the chemical potential for site i , σ the spin of electrons, t_{ij} the nearest hopping term, U_i the onsite Coulomb energy and V_{ij} the Coulomb term for nearest-neighbour sites. Amazingly, they showed they can control all the parameters in this model by adjusting the voltages that define the dots. Utilizing this model, they realized a Mott transition in this three-dot system.

Another example is the realization of Nagaoka ferromagnetism in quantum dots systems. In the 1960s, Nagaoka proposed a theorem about ferromagnetism [24] based on a simple Hubbard model for a single band:

$$H = - \sum_i \epsilon_i n_i - \sum_{\langle i,j \rangle, \sigma} t_{ij} (c_{i\sigma}^\dagger c_{j\sigma} + h.c.) + \sum_i U_i n_{i\uparrow} n_{i,\downarrow}, \quad (2.2)$$

where again ϵ_i is the chemical potential for site i , σ the spin of electrons, t_{ij} the nearest hopping term and U_i the onsite Coulomb energy. Nagaoka showed analytically that for some lattice configurations, when $U \gg t$ and there is only a single hole in the half filling state for all sites (Mott-insulating state), the ground state is ferromagnetic (with the largest total spin). A good example of this is a 1D loop lattice with N sites. To obtain Nagaoka

ferromagnetism, one should put $N - 1$ electrons at almost half-filling. Assuming N is even, the single hole in the system can tunnel to the opposite position through two paths, and this interference leads to a ferromagnetic ground state. Using the same technique proposed by Ref. [22], another experimental work implemented these conditions in a four-dot-ring system [23]. They realized Nagaoka ferromagnetism in this system, showing that Nagaoka ferromagnetism can appear even in such a small system.

Although there are substantial challenges with scaling up to larger quantum dot systems, as the experimental techniques in semiconductor quantum dot systems continue to become more advanced, one can expect to simulate more complicated strongly correlated systems. This could potentially open a new door to understanding emerging phenomena such as high temperature superconductivity and magnetism.

2.3 Spin qubits in quantum dot systems

Spins in GaAs and Si lateral quantum dots are promising candidates for implementing a quantum computer due to their scalability [1, 3, 25], long coherence times [26, 27, 28, 29], and rapid gate operations [30, 31, 32]. Qubits based on electron spins in quantum dots come in several varieties, including ones based on individual electron spins [3, 33, 34], two-electron singlet-triplet qubits [27, 30], and three-electron resonant exchange qubits [32, 35, 36, 37] and hybrid qubits [38, 39, 40]. Different qubits systems faces different advantages and challenges. Thus, it is hard to say which one is generically better [1, 41]. Now we will introduce each kind of spin qubit to bring a flavor of the diversity of this field to the reader.

Single-spin qubits: A single-spin-qubit quantum dot system was first proposed by Loss and DiVincenzo [3] as the first example of quantum computing in a quantum dot system.

An electron has total spin $S = \frac{1}{2}$, which leads to two possible states in the z basis $|\uparrow\rangle$ and $|\downarrow\rangle$ corresponding to $S_z = +\frac{1}{2}$ and $S_z = -\frac{1}{2}$, respectively. Thus the qubit can be easily encoded as $|0\rangle = |\uparrow\rangle$ and $|1\rangle = |\downarrow\rangle$.

Singlet-triplet qubits: Singlet-triplet qubits involve two-electron states. This kind of qubits are easily controlled by exchange energy as we will mention later. The spins of two electrons have four possible states: $|\uparrow\uparrow\rangle$, $|\uparrow\downarrow\rangle$, $|\downarrow\uparrow\rangle$, $|\downarrow\downarrow\rangle$. These state can be combined to form one singlet state and three triplet states based on the spin state being anti-symmetric or symmetric, which corresponds to the $S = 0$ and $S = 1$ representations of the group, respectively. For the $S_z = 0$ subspace we define singlet and triplet respectively as $|S\rangle = \frac{1}{\sqrt{2}}(|\uparrow\downarrow\rangle - |\downarrow\uparrow\rangle)$ and $|T_0\rangle = \frac{1}{\sqrt{2}}(|\uparrow\downarrow\rangle + |\downarrow\uparrow\rangle)$. Therefore, in this system one can encode $|0\rangle = |S\rangle$ and $|1\rangle = |T\rangle$.

Three-electron resonant exchange qubits: For three-electron states, we have three irreducible representations: a quadruplet representation for the total spin $S = \frac{3}{2}$, $|Q_{S_z}\rangle$, where $S_z = \pm\frac{3}{2}, \pm\frac{1}{2}$ and two pairs of doublets $|D_{S_z}\rangle$ and $|D'_{S_z}\rangle$, where $S_z = \pm\frac{1}{2}$. These

states are defined as

$$|Q_{+3/2}\rangle = |\uparrow\uparrow\uparrow\rangle, \quad (2.3)$$

$$|Q_{+1/2}\rangle = \frac{1}{\sqrt{3}}(|\uparrow\uparrow\downarrow\rangle + |\uparrow\downarrow\uparrow\rangle + |\downarrow\uparrow\uparrow\rangle), \quad (2.4)$$

$$|Q_{-1/2}\rangle = \frac{1}{\sqrt{3}}(|\downarrow\downarrow\uparrow\rangle + |\downarrow\uparrow\downarrow\rangle + |\uparrow\downarrow\downarrow\rangle), \quad (2.5)$$

$$|Q_{-3/2}\rangle = |\downarrow\downarrow\downarrow\rangle, \quad (2.6)$$

$$|D_{+1/2}\rangle = \frac{1}{\sqrt{6}}(|\uparrow\uparrow\downarrow\rangle + |\uparrow\downarrow\uparrow\rangle - 2|\downarrow\uparrow\uparrow\rangle), \quad (2.7)$$

$$|D_{-1/2}\rangle = \frac{1}{\sqrt{6}}(|\downarrow\downarrow\uparrow\rangle + |\downarrow\uparrow\downarrow\rangle - 2|\uparrow\downarrow\downarrow\rangle), \quad (2.8)$$

$$|D'_{+1/2}\rangle = \frac{1}{\sqrt{2}}(|\uparrow\uparrow\downarrow\rangle - |\uparrow\downarrow\uparrow\rangle), \quad (2.9)$$

$$|D'_{-1/2}\rangle = \frac{1}{\sqrt{2}}(|\downarrow\downarrow\uparrow\rangle - |\downarrow\uparrow\downarrow\rangle). \quad (2.10)$$

The logical qubit states can be defined for the same S_z from two different representations of the doublets: $|0\rangle = |D_{\pm 1/2}\rangle$ and $|1\rangle = |D'_{\pm 1/2}\rangle$.

Hybrid qubits: Hybrid qubits are also defined in three-electron systems. However, the basis for defining the qubits here is not the natural states defined by group representations we just mentioned. One can instead combine states with $S = \frac{1}{2}$ and $S_z = -\frac{1}{2}$ to define the logical qubit states as $|0\rangle = |S\rangle |\downarrow\rangle$ and $|1\rangle = \frac{1}{\sqrt{3}} |T_0\rangle |\downarrow\rangle - \frac{\sqrt{2}}{\sqrt{3}} |T_-\rangle |\uparrow\rangle$, where the singlet and triplets are the two-electron states we mentioned before. Therefore the word “hybrid” means the mixture of triplets. This choice is not unique, and one can also use other combinations to define hybrid qubits.

As we have seen, there are many ways to define the logical qubit states. A specific system works better under a specific definition of qubits. Qubits with fewer spins are more efficient to fabricate but qubits with more spins are more robust and provide all-electrical control.

The interplay of all factors would decide what the best qubit definition is for a system. However, no matter how we define a spin qubit, we would need the logical states $|0\rangle$ and $|1\rangle$ to have different energy for manipulating states on the Bloch sphere. Moreover, in all kinds of qubit systems, exchange energy plays an important role.

2.4 Singlet-triplet exchange energy

In this section, we review the definition for the exchange energy between singlet and triplet states from the quantum computation point of view. We also explain how the exchange energy can be measured experimentally.

First of all, as we mentioned earlier, based on symmetry, we define the two electron spin states as

$$|S\rangle = \frac{1}{\sqrt{2}}(|\uparrow\downarrow\rangle - |\downarrow\uparrow\rangle) \quad (2.11)$$

$$|T_0\rangle = \frac{1}{\sqrt{2}}(|\uparrow\downarrow\rangle + |\downarrow\uparrow\rangle) \quad (2.12)$$

$$|T_+\rangle = |\uparrow\uparrow\rangle \quad (2.13)$$

$$|T_-\rangle = |\downarrow\downarrow\rangle. \quad (2.14)$$

Let us consider a system with only two orbitals and two electrons. For the three triplets $|T_\pm\rangle$ and $|T_0\rangle$, it is forbidden for two electrons to occupy the same orbital due to the Pauli exclusion principle. However, for the singlet $|S\rangle$, the two electrons are allowed to occupy the same orbital. When the two orbitals are both at half-filling and the electron spins are in state $|S\rangle$, the Coulomb exchange corresponds to a virtual process in which the electrons both hop onto the same orbital. This lowers the energy of the singlet $|S\rangle$. If these two orbitals are occupying different dots with large separation, the singlet and triplet states should be

degenerate because the effect of Coulomb exchange interaction is infinitely small. When the hopping is possible, an energy gap is created by this mechanism making $|S\rangle$ the ground state. This energy gap can be defined as the exchange energy

$$J_{ex} = E_{T_0} - E_S. \quad (2.15)$$

One can also write the Hamiltonian for this system, which is called a Heisenberg model:

$$H = \frac{1}{\hbar^2} J_{ex} \vec{S}_1 \cdot \vec{S}_2, \quad (2.16)$$

where \vec{S}_1 and \vec{S}_2 are the spin operators for the two electrons. This can be solved exactly, leading to the eigenvectors just as we had before $|S\rangle$, $|T_0\rangle$, $|T_+\rangle$ and $|T_-\rangle$. The corresponding eigenvalues are $-\frac{3}{4}J_{ex}$, $\frac{1}{4}J_{ex}$, $\frac{1}{4}J_{ex}$ and $\frac{1}{4}J_{ex}$, respectively. Thus, the energy gap between the triplets and singlet is just J_{ex} , the exchange energy. When a magnetic field is applied to the system, the triplets will split into three levels leading to the Zeeman effect. However the definition of exchange energy J_{ex} is robust to magnetic fields, since $|T_0\rangle$ and $|S\rangle$ are all $S_z = 0$ states.

This exchange energy can be measured experimentally [30]. Now let us consider a two-dot system with two electrons. The whole process is shown in Fig. 2.4. We start the experiment by preparing two electrons in the right dot. The chemical potential difference of these two dots is defined as the detuning ε . We set $\varepsilon > 0$ to make this happen, which gives us the singlet initial state in the right dot. At $t = 0$, for ε , we choose a target detuning at which we wish to obtain the exchange energy and change the system to that detuning adiabatically. For every detuning point we choose, scan over the magnitude of the magnetic field and let the system evolve for time $t = \tau_s$ for each magnetic field value. The magnetic field splits the triplets due to the Zeeman effect. If the intersection of the states $|T_+\rangle$ and $|S\rangle$ is right at the

target detuning, there will be leakage from $|S\rangle$ to $|T_+\rangle$ due to the hyperfine interaction [30] in these quantum dots, which flips the spins. After $t = \tau_s$, we implement the measurement. This is done by detuning back adiabatically into the $\varepsilon > 0$ region to make the electron hop back to the right dot, thus measuring the return probability of the singlet $|S\rangle$. If the leakage does happen, the measured return probability should be significantly less than 1 and part of the state remains in $|T_+\rangle$. Thus we obtain a return probability for each magnetic field and detuning as Fig. 2.4(C) shows. And the magnitude of the exchange energy J_{ex} corresponds to the magnetic field strength along the yellow dashed line for each detuning $\varepsilon < 0$. One might think that in Fig. 2.4(B), if we keep changing the detuning to large values of ε , the exchange energy becomes very large since there is a huge gap between $|T_0\rangle$ and $|S\rangle$ states. This is not right because when the two electrons are both in the right dot, both electrons can only occupy the lowest orbital in the dot if they are in state $|S\rangle$ whereas one electron needs to hop onto the first-excited orbital in the dot if the spin state is $|T_0\rangle$. Therefore the gap here should not be understood as the exchange energy, but instead the energy gap between the orbitals in the dot. On the other hand, one can also consider the inter-orbital exchange energy in one dot but this demands almost same orbital occupation for $|T_0\rangle$ and $|S\rangle$, and this singlet exists at higher energy.

This approach of extracting the exchange energy in two-dot systems is generic and can be extended to multi-dot systems. Theoretically, the singlet-triplet exchange interaction is an effective interaction, and we will talk about the origin of this interaction in the next chapter.

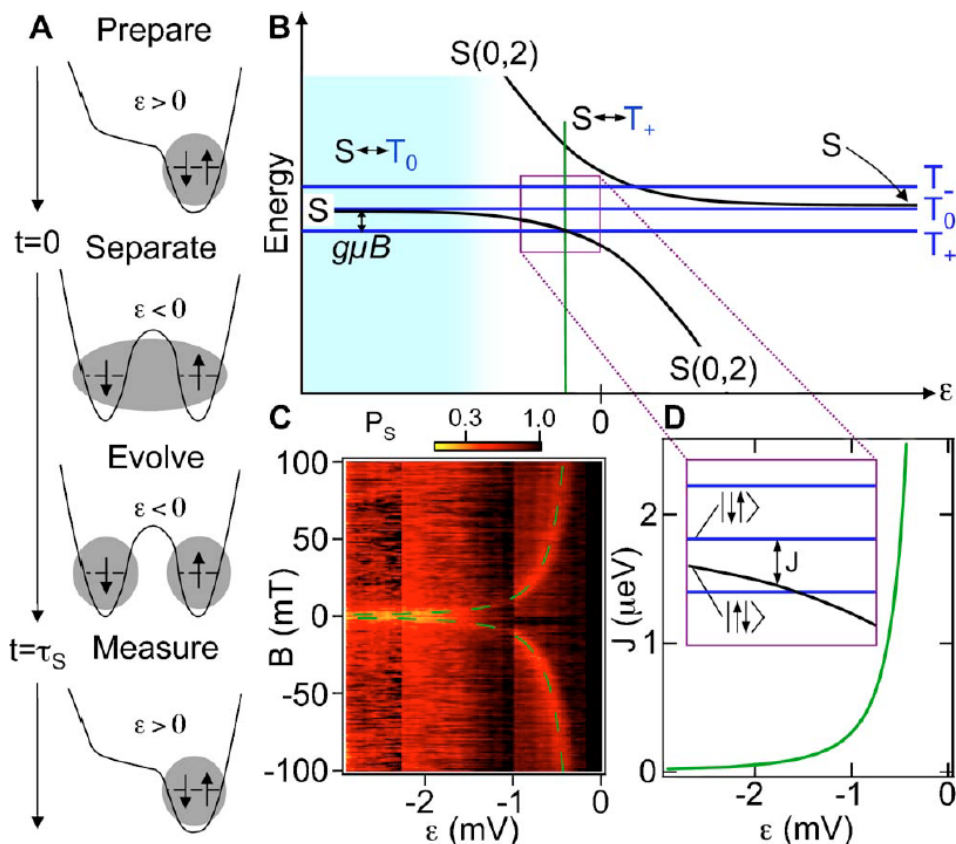


Figure 2.4: Measurement of exchange energy in a two-dot system. Detuning ε is defined as the chemical potential difference of the two dots. (A) The process of the experiment. (B) The spectrum as a function of the detuning ε . (C) Reading exchange energy from the strength of the out-of-plane magnetic field B . (D) The zooming up of (B) for negative detunings and a very small magnetic field difference is applied to two dots causing the eigenstates to be $|\uparrow\downarrow\rangle$ and $|\downarrow\uparrow\rangle$ for very negative ε . At $t < 0$ we prepare a singlet in the right dot. At $t = 0$, we adjust the detuning ε adiabatically to any point less than 0, which is the point we want to get the exchange energy for. Do this sweep each time with different magnetic field to scan. Then we wait for the system to evolve for time $t = \tau_S$. In this time interval, a leakage would happen only when the testing point is around the crossing of the $|S\rangle$ and $|T_+\rangle$ states due to the fact that the hyperfine interaction can flip the spins in the dots. After $t = \tau_S$ we change the detuning adiabatically back to the $\varepsilon > 0$ region to get the $(0, 2)$ configuration again. And we test the return probability of the singlet part of $(0, 2)$. If the evolution happens at the crossing point, the leakage will cause the return probability to be significantly less than 1, which can be read from the low probability curve in (C). Therefore, the magnetic field strength of the yellow curve in (C) can be mapped into the magnitude of the exchange energy J_{ex} for any detuning we choose in the ε region. Adapted from Ref. [1]

Chapter 3

Many-particle theory and experimental controls in quantum dots

In this chapter, we introduce the theory to describe quantum dot systems. First we build single particle states in a single quantum dot. Based on the single particle orbitals, we construct many-particle states by utilizing Slater-Condon rules. After that, starting from a generic Hamiltonian, we derive a series of effective models of increasing simplicity by putting assumptions one by one until finally arriving at the Heisenberg model. At the end of this chapter, we briefly discuss an experiment and its model for controlling Heisenberg couplings.

3.1 Single particle in one quantum dot

In a quantum dot, the real potential for an electron is complicated. However, one can use simple models to describe it such as a Gaussian potential or a quadratic potential [42]. Here we use a quadratic potential to model the dot. Without considering the spin part, and in the presence of an applied magnetic field, the single particle Hamiltonian reads

$$H = \frac{1}{2m^*}(-i\hbar\nabla + \frac{e}{c}\mathbf{A})^2 + \frac{1}{2}m^*\omega_0^2r^2, \quad (3.1)$$

where m^* is the effective mass of the electron in quantum dots, \mathbf{A} is the vector potential, $\hbar\omega_0$ is the quantum dot confinement energy, and $r = \sqrt{x^2 + y^2}$ is the radius. This harmonic Hamiltonian is called the Fock-Darwin Hamiltonian [43] and it can be solved analytically. First we choose the vector potential which induces a magnetic field in z direction (orthogonal to the plane of the dot):

$$\mathbf{A} = -\frac{B}{2}y\hat{x} + \frac{B}{2}x\hat{y}. \quad (3.2)$$

And we define the cyclotron frequency:

$$\omega_c \equiv \frac{eB}{m^*c}. \quad (3.3)$$

Following Ref. [43], here we derive the solutions. The Hamiltonian can be rewritten as

$$H = -\frac{\hbar^2}{2m^*}\nabla^2 + \frac{1}{2}m^*(\omega_0^2 + \frac{1}{4}\omega_c^2)r^2 + \frac{1}{2}\omega_c\ell_z, \quad (3.4)$$

where ℓ_z is the angular momentum in the z direction:

$$\ell_z = -i\hbar(x\partial_y - y\partial_x). \quad (3.5)$$

Now let us define complex coordinates:

$$z = \frac{x + iy}{\sqrt{2}\ell_0}, \quad \bar{z} = \frac{x - iy}{\sqrt{2}\ell_0}, \quad (3.6)$$

$$\partial = \frac{l_0}{\sqrt{2}}(\partial_x - i\partial_y), \quad \bar{\partial} = \frac{l_0}{\sqrt{2}}(\partial_x + i\partial_y), \quad (3.7)$$

where we have defined respectively the length scale ℓ_0 and the magnetic length as

$$\ell_0 \equiv \ell_B \left(\frac{1}{4} + \frac{\omega_0^2}{\omega_c^2} \right)^{-\frac{1}{4}}, \quad (3.8)$$

$$\ell_B \equiv \sqrt{\frac{\hbar c}{eB}}. \quad (3.9)$$

When the magnetic field $B \rightarrow 0$, the magnetic length goes to infinity but ℓ_0 remains finite in this limit because B cancels in the denominator. Now we define some creation and annihilation operators:

$$a = \frac{1}{\sqrt{2}}(\bar{z} + \partial), \quad a^\dagger = \frac{1}{\sqrt{2}}(z - \bar{\partial}), \quad (3.10)$$

$$b = \frac{1}{\sqrt{2}}(z + \bar{\partial}), \quad b^\dagger = \frac{1}{\sqrt{2}}(\bar{z} - \partial). \quad (3.11)$$

One can find the commutation relation as:

$$[a, a^\dagger] = 1, \quad [b, b^\dagger] = 1. \quad (3.12)$$

And all the other commutators are equal to 0. Thus the Hamiltonian can be written in a new harmonic form:

$$H = \hbar\omega_+(a^\dagger a + \frac{1}{2}) + \hbar\omega_-(b^\dagger b + \frac{1}{2}), \quad (3.13)$$

where we have defined

$$\omega_\pm \equiv \sqrt{\omega_0^2 + \frac{1}{4}\omega_c^2} \pm \frac{1}{2}\omega_c. \quad (3.14)$$

For this Hamiltonian, one can obtain the normalized ground state wave function:

$$\psi_0 = \sqrt{\frac{2}{\pi}} e^{-z\bar{z}}. \quad (3.15)$$

Noticing from the commutation relation that we have:

$$a^\dagger a (a^\dagger)^n = n (a^\dagger)^n + (a^\dagger)^{n+1} a, \quad (3.16)$$

$$b^\dagger b (b^\dagger)^n = n (b^\dagger)^n + (b^\dagger)^{n+1} b. \quad (3.17)$$

We see that the other excited states can be generated from the ground state:

$$\psi_{n_+, n_-} = \frac{1}{n_+! n_-!} (a^\dagger)^{n_+} (b^\dagger)^{n_-} \psi_0. \quad (3.18)$$

And the eigenenergies can be easily written as two harmonic oscillators

$$E_{n_+, n_-} = \hbar\omega_+ \left(n_+ + \frac{1}{2}\right) + \hbar\omega_- \left(n_- + \frac{1}{2}\right). \quad (3.19)$$

where n_+ and n_- are both natural numbers. We define the quantum numbers

$$n \equiv n_+ + n_-, \quad m \equiv n_+ - n_-, \quad (3.20)$$

and the energies can be rewritten as

$$E_{n,m} = (n+1)\hbar\sqrt{\omega_0^2 + \frac{1}{4}\omega_c^2} + \frac{1}{2}m\hbar\omega_c, \quad (3.21)$$

where the principal quantum number $n \geq 0$ is an integer, and the magnetic quantum number m runs from $-n$ to n in steps of 2. The corresponding eigenstates are called Fock-Darwin states. Borrowing from atomic physics, we can call n the shell number. Here each shell n

contains n states labeled by m . As one can see, when the magnetic field is turned off, i.e., when $\omega_c = 0$, we have all degenerate states in each shell. This is easy to understand if one treats the system as two harmonic oscillators in the x and y directions respectively.

3.2 Building many particle states

The Fock-Darwin states we have just constructed are a complete and orthonormal basis. They can serve as building blocks for us to construct many particle states. Now we define the many particle states in the second-quantized form as

$$|\psi\rangle = \left| \{ \alpha_{\uparrow}^{(1)}, \alpha_{\uparrow}^{(2)}, \dots \}, \{ \alpha_{\downarrow}^{(1)}, \alpha_{\downarrow}^{(2)}, \dots \} \right\rangle, \quad (3.22)$$

where for instance $\alpha_{\downarrow}^{(2)}$ represents a spin-down electron in the Fock-Darwin state with quantum numbers $\alpha^{(i)} = \{ \eta_i, n_i, m_i \}$. And η_i is the dot label. Notice that in each dot, the Fock-Darwin states are orthonormal, however, the two sets of Fock-Darwin states from each dot are not orthonormal. When two dots are far away, it is a good approximation to assume they are orthonormal since their overlaps are small, but when two dots are close enough, this argument is no longer true. In this case, one needs to find the new orthonormal single particle basis to build the many particle states above.

3.2.1 Cholesky decomposition

There is an efficient, systematic way to construct an orthonormal basis from non-orthogonal states. Imagine we have the original non-orthonormal basis $|NO\rangle$ and we are looking for the unknown orthonormal basis $|O\rangle$. In the non-orthonormal basis, the matrix of the overlap

operator is:

$$\langle \eta_i, n_i, m_i | \mathcal{O} | \eta_j, n_j, m_j \rangle = \langle \eta_i, n_i, m_i | \eta_j, n_j, m_j \rangle. \quad (3.23)$$

For any single particle operator \mathcal{A}' in the new orthonormal basis, we have the transformation from the operator \mathcal{A} in the non-orthonormal basis:

$$\mathcal{A}' = L\mathcal{A}L^\dagger. \quad (3.24)$$

Therefore the overlap operator in the new orthonormal basis should have the same form:

$$\mathcal{O}' = L\mathcal{O}L^\dagger = \mathcal{I}, \quad (3.25)$$

which leads to

$$\mathcal{O} = L^{-1}(L^{-1})^\dagger, \quad (3.26)$$

where the last equality in Eq. (3.25) is due to the fact that the new basis is orthonormal. This L^{-1} is a solvable triangular matrix, and this approach is the well known Cholesky decomposition. After obtaining the matrix A of an operator \mathcal{A} in the non-orthonormal basis, one can easily transform it to the new matrix A' under the new orthonormal basis.

The operator matrix transformation is obvious; however, the explicit wave function transformation is not so trivial and is different than its transformation of the representations. Denoting the Fock-Darwin wave functions as:

$$FD = \{FD_1, FD_2, \dots\}^\top, \quad (3.27)$$

after some algebra, one can show that the wave function transformation should be

$$FD_{OB} = (L^\dagger)^\top FD. \quad (3.28)$$

For a multi-dot platform such as a two-dot system, the new orthonormal basis constructed by Cholesky decomposition is actually very close to the original basis if the two dots are not too close, which is the usual case in spin qubit quantum computation and simulation. Generally speaking, the new state labels such as the labels in $\alpha^{(i)'} = \{\eta'_i, n'_i, m'_i\}$ are still indicating the positions and quantum numbers for quantum dots approximately.

3.2.2 Slater-Condon rules for many particle states

After the Cholesky decomposition, now we can safely assume that in Eq. (3.22), all the single particle states are orthonormal. A generic many particle Hamiltonian for N electrons in an external potential $V(\mathbf{r}_k)$ is:

$$H = \sum_{k=1}^N \left[\frac{1}{2m^*} (-i\hbar\nabla_k + \frac{e}{c}\mathbf{A})^2 + V(\mathbf{r}_k) + g^* \mu_B \mathbf{B} \cdot \mathbf{S}_k \right] + \sum_{j < k} \frac{e^2}{\kappa |\mathbf{r}_j - \mathbf{r}_k|}, \quad (3.29)$$

where m^* is the effective electron mass, $g^* = -0.44$ is the effective Landé factor, μ_B is the Bohr magneton, and the dielectric constant for this material is κ . We set the magnetic field to be out of plane $\mathbf{B} = B_0 \hat{z}$. Here, we are neglecting hyperfine interactions between the electrons and the surrounding nuclei in the semiconductor lattice. This Hamiltonian can be awkward to work with when N is large, and it is preferable to switch to its second-quantized

form:

$$H = \sum_{i,i'} t_{ii'} a_{i\sigma}^\dagger a_{i'\sigma} + \sum_{i,i',j,j'} U_{ii'jj'} a_{i\sigma}^\dagger a_{i'\sigma}^\dagger a_{j'\sigma'} a_{j\sigma}, \quad (3.30)$$

where i, i', j, j' are the orbital numbers (orthonormal single particle state numbers), $t_{ii'}$ is the single particle hopping and onsite energy produced by the integration of the single particle terms, and $U_{ii'jj'}$ is the two particle interaction obtained from the Coulomb integrals. This new Hamiltonian can be separated into two parts:

$$H = \mathcal{A} + \mathcal{C}, \quad (3.31)$$

where \mathcal{A} is the combination of all the single particle terms, and \mathcal{C} is all the two-particle Coulomb interactions. For the states in Eq. (3.22), our goal is to get all the matrix elements for this many particle Hamiltonian:

$$\langle \psi' | H | \psi \rangle. \quad (3.32)$$

This goal can be achieved efficiently using the Slater-Condon rules, which relate the many particle matrix elements to the single particle and double particle matrix elements. First we consider the first part of the Hamiltonian \mathcal{A} . For diagonal terms, one has

$$\begin{aligned} \langle \psi | \mathcal{A} | \psi \rangle &= \left\langle \{ \alpha_\uparrow^{(1)}, \alpha_\uparrow^{(2)}, \dots \}, \{ \alpha_\downarrow^{(1)}, \alpha_\downarrow^{(2)}, \dots \} \middle| \mathcal{A} \middle| \{ \alpha_\uparrow^{(1)}, \alpha_\uparrow^{(2)}, \dots \}, \{ \alpha_\downarrow^{(1)}, \alpha_\downarrow^{(2)}, \dots \} \right\rangle \\ &= \sum_{\beta \in \{ \alpha_\uparrow^{(1)}, \dots \}} \langle \beta | \mathcal{A} | \beta \rangle + \sum_{\beta \in \{ \alpha_\downarrow^{(1)}, \dots \}} \langle \beta | \mathcal{A} | \beta \rangle. \end{aligned} \quad (3.33)$$

For non-diagonal terms, the terms will be non-zero only if $|\psi\rangle$ and $|\psi'\rangle$ differ by one single particle orbital either with spin up or down, but it has to be the same spin. An example for

one orbital difference with spin up can be constructed as

$$\begin{aligned}\langle \psi' | \mathcal{A} | \psi \rangle &= \left\langle \{ \alpha_{\uparrow}^{(1)}, \dots, \alpha_{\uparrow}^{(k')}, \dots \}, \{ \alpha_{\downarrow}^{(1)}, \dots \} \middle| \mathcal{A} \middle| \{ \alpha_{\uparrow}^{(1)}, \dots, \alpha_{\uparrow}^{(k)}, \dots \}, \{ \alpha_{\downarrow}^{(1)}, \dots \} \right\rangle \\ &= (-1)^{k+k'} \left\langle \alpha_{\uparrow}^{(k')} \middle| \mathcal{A} \middle| \alpha_{\uparrow}^{(k)} \right\rangle.\end{aligned}\quad (3.34)$$

where $\alpha_{\uparrow}^{(k')}$ is different from $\alpha_{\uparrow}^{(k)}$, and other corresponding quantum numbers are the same in both states. The spin down ones are similar. The minus sign is from the fermionic commutation relation.

For Coulomb terms, it involves two-particle states and will be more complicated. The diagonal terms read:

$$\begin{aligned}\langle \psi | \mathcal{C} | \psi \rangle &= \left\langle \{ \alpha_{\uparrow}^{(1)}, \dots \}, \{ \alpha_{\downarrow}^{(1)}, \dots \} \middle| \mathcal{C} \middle| \{ \alpha_{\uparrow}^{(1)}, \dots \}, \{ \alpha_{\downarrow}^{(1)}, \dots \} \right\rangle \\ &= \sum_{\beta_1, \beta_2 \in \{ \alpha_{\uparrow}^{(1)}, \dots \} \cup \{ \alpha_{\downarrow}^{(1)}, \dots \}} \langle \beta_1, \beta_2 | \mathcal{C} | \beta_1, \beta_2 \rangle - \sum_{\beta_1, \beta_2 \in \{ \alpha_{\uparrow}^{(1)}, \dots \}} \langle \beta_1, \beta_2 | \mathcal{C} | \beta_2, \beta_1 \rangle \\ &\quad - \sum_{\beta_1, \beta_2 \in \{ \alpha_{\downarrow}^{(1)}, \dots \}} \langle \beta_1, \beta_2 | \mathcal{C} | \beta_2, \beta_1 \rangle,\end{aligned}\quad (3.35)$$

where the matrix elements in the first sum are called direct terms, and those in the second and third sums are called exchange terms. For the diagonal terms, the states can be different in either one or two single particle states and these cases are different here. Assuming we have only one orbital difference with spin up, we get

$$\begin{aligned}\langle \psi' | \mathcal{C} | \psi \rangle &= \left\langle \{ \alpha_{\uparrow}^{(1)}, \dots, \alpha_{\uparrow}^{(k')}, \dots \}, \{ \alpha_{\downarrow}^{(1)}, \dots \} \middle| \mathcal{C} \middle| \{ \alpha_{\uparrow}^{(1)}, \dots, \alpha_{\uparrow}^{(k)}, \dots \}, \{ \alpha_{\downarrow}^{(1)}, \dots \} \right\rangle \\ &= (-1)^{k+k'} \sum_{\beta \in (\{ \alpha_{\uparrow}^{(1)}, \dots \} \cap \{ \alpha_{\uparrow}^{(1)}, \dots \}) \cup \{ \alpha_{\downarrow}^{(1)}, \dots \}} \left\langle \beta, \alpha_{\uparrow}^{(k')} \middle| \mathcal{C} \middle| \beta, \alpha_{\uparrow}^{(k)} \right\rangle \\ &\quad - (-1)^{k+k'} \sum_{\beta \in \{ \alpha_{\uparrow}^{(1)}, \dots \} \cap \{ \alpha_{\uparrow}^{(1)}, \dots \}} \left\langle \beta, \alpha_{\uparrow}^{(k')} \middle| \mathcal{C} \middle| \alpha_{\uparrow}^{(k)}, \beta \right\rangle.\end{aligned}\quad (3.36)$$

If we have two orbitals that differ with both spin up, we have

$$\begin{aligned} \langle \psi' | \mathcal{C} | \psi \rangle &= \left\langle \{ \alpha_{\uparrow}^{\prime(1)}, \dots, \alpha_{\uparrow}^{\prime(k'_1)}, \dots, \alpha_{\uparrow}^{\prime(k'_2)}, \dots \}, \{ \alpha_{\downarrow}^{(1)}, \dots \} \middle| \mathcal{C} \middle| \{ \alpha_{\uparrow}^{(1)}, \dots, \alpha_{\uparrow}^{(k_1)}, \dots, \alpha_{\uparrow}^{(k_2)}, \dots \}, \{ \alpha_{\downarrow}^{(1)}, \dots \} \right\rangle \\ &= (-1)^{k_1+k_2+k'_1+k'_2} \left[\left\langle \alpha_{\uparrow}^{\prime(k'_1)}, \alpha_{\uparrow}^{\prime(k'_2)} \middle| \mathcal{C} \middle| \alpha_{\uparrow}^{(k_1)}, \alpha_{\uparrow}^{(k_2)} \right\rangle - \left\langle \alpha_{\uparrow}^{\prime(k'_1)}, \alpha_{\uparrow}^{\prime(k'_2)} \middle| \mathcal{C} \middle| \alpha_{\uparrow}^{(k_2)}, \alpha_{\uparrow}^{(k_1)} \right\rangle \right], \end{aligned} \quad (3.37)$$

where direct terms and exchange terms both survive. However, if the spin differences are one up and one down, we can only have the direct term because the spin flipping is not allowed here:

$$\begin{aligned} \langle \psi' | \mathcal{C} | \psi \rangle &= \left\langle \{ \alpha_{\uparrow}^{\prime(1)}, \dots, \alpha_{\uparrow}^{\prime(k'_1)}, \dots \}, \{ \alpha_{\downarrow}^{\prime(1)}, \dots, \alpha_{\downarrow}^{\prime(k'_2)}, \dots \} \middle| \mathcal{C} \middle| \{ \alpha_{\uparrow}^{(1)}, \dots, \alpha_{\uparrow}^{(k_1)}, \dots \}, \{ \alpha_{\downarrow}^{(1)}, \dots, \alpha_{\downarrow}^{(k_2)}, \dots \} \right\rangle \\ &= (-1)^{k_1+k_2+k'_1+k'_2} \left\langle \alpha_{\uparrow}^{\prime(k'_1)}, \alpha_{\downarrow}^{\prime(k'_2)} \middle| \mathcal{C} \middle| \alpha_{\uparrow}^{(k_1)}, \alpha_{\downarrow}^{(k_2)} \right\rangle. \end{aligned} \quad (3.38)$$

Together, this accounts for all the terms in the many particle Hamiltonian. Once we obtain all the matrix elements from single and double particle terms, we can build the full matrix for the total Hamiltonian based on these rules.

3.3 From a generic Hamiltonian to the Heisenberg model

In this section, we derive the possible ferromagnetic and anti-ferromagnetic mechanisms in quantum dot systems. Again, we consider the generic second-quantized Hamiltonian Eq. (3.30), and pick out specific terms from it.

3.3.1 Ferromagnetic couplings

First of all, we define the spin operators in the second-quantized form,

$$\vec{S}_i = \frac{1}{2} a_{i\alpha}^\dagger \vec{\sigma}_{\alpha\beta} a_{i\beta}, \quad (3.39)$$

where $\vec{\sigma}$ is the three Pauli matrices and i is the i th orbital in all the orbital pools. We pick out the Coulomb terms where $i' = j$ and $j' = i$, and $i \neq j$. After some algebra, one can show that these terms can be written as the spin-spin interactions for different orbitals:

$$\sum_{i \neq j} U_{ijji} a_{i\sigma}^\dagger a_{j\sigma'}^\dagger a_{i\sigma'} a_{j\sigma} = -2 \sum_{i \neq j} J_{ij}^F (\vec{S}_i \cdot \vec{S}_j + \frac{1}{4} n_i n_j), \quad (3.40)$$

where $n_i = a_{i\uparrow}^\dagger a_{i\uparrow} + a_{i\downarrow}^\dagger a_{i\downarrow}$ is the occupation number and $J_{ij}^F = U_{ijji}$. Inside of one dot, between many orbitals this term is normally positive, which leads to ferromagnetism. For atomic physics, Hund's rule arises in this way. For quantum dot systems, if the electrons do not occupy the same dot on higher orbitals instead of just the lowest one, this term does not contribute significantly to the energy. However, as we will see later in the next chapter, this mechanism will be the main factor leading to negative exchange.

3.3.2 From the tight-binding model to the Heisenberg model

Now we explore the other terms in Eq. (3.30). Before doing so, we confine ourselves to considering only short distance interactions, i.e., we make this generic Hamiltonian tight-binding with nearest neighbors. When the electrons are widely distributed across several quantum dots and do not congregate in a in specific dot, the interdot Coulomb interactions should be sufficiently small. Only the lowest orbitals will be occupied in the quantum dots. Furthermore, we assume the hopping term is identical for each dot and only onsite Coulomb

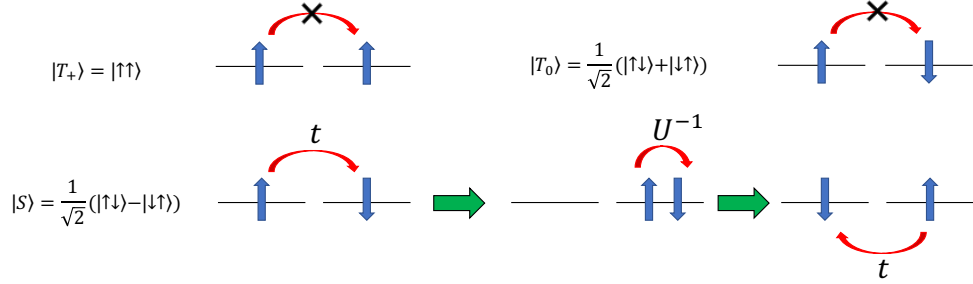


Figure 3.1: The exchange procedure. For triplet states including $|T_{\pm}\rangle$ and $|T_0\rangle$, the Pauli exclusion principle prevents hopping. However, for a singlet state, it is allowed for an electron to hop into the neighboring site. The left electron can hop virtually into the right dot and give rise to Coulomb interaction. And the original right electron can hop into the left site. These three processes combine to generate the exchange coupling $J = \frac{t^2}{U}$.

energy contributes substantially. Thus we obtain

$$H = t \sum_{i \neq j} a_{i\sigma}^\dagger a_{j\sigma} + U \sum_i n_{i\uparrow} n_{i\downarrow}, \quad (3.41)$$

where i, j are nearest neighbors and $U = 2U_{iiii}$ is the onsite Coulomb coupling. This form of the Hamiltonian is the well-known Hubbard model. In this model, we have only two parameters t and U , but this is really powerful because it turns out to be able to describe a lot of systems in condensed matter. Again if we introduce the spin operator as in Eq. (3.39), we can change the form of the coupling into the effective spin-spin interaction at leading order:

$$H = J \sum_{i \neq j} \vec{S}_i \cdot \vec{S}_j, \quad (3.42)$$

where $J = \frac{t^2}{U}$ is the effective spin-spin coupling, which is also called exchange energy. In this form we have neglected the $\mathcal{O}(t^2)$ terms. This Hamiltonian is called the Heisenberg model. As one would notice, here the coupling satisfies $J > 0$, as follows from the fact that $U > 0$. This model leads to anti-ferromagnetism.

This exchange process can be understood in another way as shown in Fig. 3.1. For the case with two electrons occupying two sites, we consider only the lowest orbital in each site. For triplet states ($|T_{\pm}\rangle$ and $|T_0\rangle$), due to the Pauli exclusion principle, the electron on the left site is not allowed to hop into the right site. However, for the singlet state, the left electron can hop virtually into the right site to produce a Coulomb interaction, and the right electron can hop to the left site afterward. These virtual processes together have amplitude $\frac{t^2}{U}$, which is exactly the exchange coupling strength. If we only consider a double-dot system with two electrons, we can solve this Hamiltonian analytically as we mentioned in Sec. 2.4 of Chapter 2, and the exchange J would be the energy difference between the triplet $|T_0\rangle$ and singlet $|S\rangle$.

3.4 An experiment: Controlling the exchange coupling in a Heisenberg chain

The work discussed in this section was published as:

Haifeng Qiao, Yadav P. Kandel, **Kuangyin Deng**, Saeed Fallahi, Geoffrey C. Gardner, Michael J. Manfra, Edwin Barnes, and John M. Nichol. “Coherent Multispin Exchange Coupling in a Quantum-Dot Spin Chain.” *Phys. Rev. X* **10**, 031006 (2020) [44].

Reuse with permission from the American Physical Society. Copyright (2020) by the American Physical Society.

In this section, we describe an experiment implemented by our collaborators in Prof. John Nichol’s group. I contributed in calculations for the Heitler-London model and conceived the idea and theory of shifting dots. I have also participated in writing the manuscript.

In multi-quantum-dot spin systems, exchange couplings between dots play important roles

for quantum computation or simulation. Thus, it is important to be able to control multiple exchange couplings simultaneously in multispin arrays. This is nontrivial because the dependence on the multidot confinement potential can depend quite nontrivially on the various gate voltages used to define it. In general, switching on an exchange coupling in part of the array can modify the dot potentials further away.

In this work, we demonstrate coherent multispin exchange coupling in a GaAs quadruple quantum dot. We show that the nonlinear and nonlocal dependence of exchange couplings on confinement gate voltages results, in large part, from electronic wave-function shifts during exchange pulses. We model our data using the Heitler-London (HL) expression for exchange coupling between two spins [45], assuming that the barrier-gate pulses used to induce exchange coupling primarily shift the locations of the electrons. The model parameters we use change slightly depending on the number of spins involved, suggesting that additional effects beyond wave-function shifts, including perhaps the quantum-dot potential depths and widths, are also important.

The parameters we extract by fitting our data to the Heitler-London model agree well with electrostatic simulations of the confinement potential of our device. We also show that a simpler, exponential model also fits our data well and can be used to predict gate voltages for independent control of exchange couplings. We demonstrate two-, three-, and four-spin exchange coupling in our four-dot device. These results are applicable to Si qubits, which feature reduced hyperfine coupling and longer electron spin coherence compared to GaAs spin qubits. Our results are also applicable to longer arrays of spin qubits, an encouraging prospect for quantum information processing and the exploration of Heisenberg spin chain physics.

The quantum dot device is shown in Fig. 3.2(a). We define virtual plunger gate voltages P_1 , P_2 , P_3 , and P_4 as linear combinations of the physical plunger gate voltages (p_1, p_2, p_3, p_4)

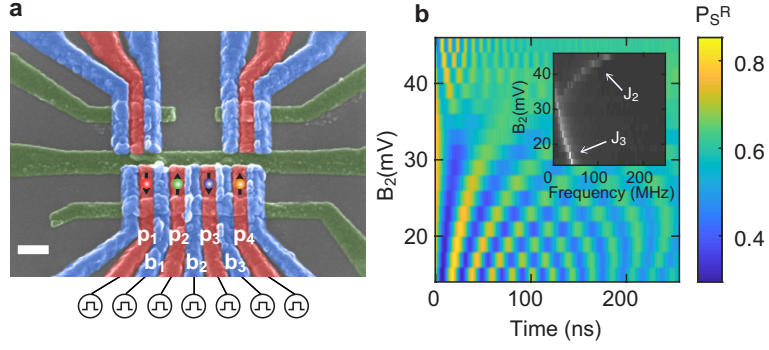


Figure 3.2: (a) Scanning electron micrograph of the quadruple quantum dot device. The upper two plunger gates are sensor quantum dots not shown explicitly. The scale bar is 200 nm. (b) Measured exchange oscillations with virtual barrier gate $B_3 = 30$ mV. Inset: Absolute value of the fast Fourier transform of data shown in (b). As B_2 increases, J_3 decreases.

such that changes to P_i are proportional to changes in the electrochemical potential of dot i . We also define virtual barrier-gate voltages B_1 , B_2 , and B_3 as the voltage applied to the corresponding physical barrier (b_1 , b_2 , and b_3) together with a linear combination of physical plunger voltages chosen such that the chemical potentials of the dots are unchanged by the barrier pulse. The spin-state Hamiltonian of the quadruple dot can be written as

$$H = \frac{\hbar}{4} \sum_{i=1}^3 J_i (\boldsymbol{\sigma}_i \cdot \boldsymbol{\sigma}_{i+1}) + \frac{\hbar}{2} \sum_{i=1}^4 B_i^z \sigma_i^z. \quad (3.43)$$

Here J_i is the exchange coupling strength (with units of frequency) between dots i and $i + 1$, $\boldsymbol{\sigma}_i = [\sigma_i^x, \sigma_i^y, \sigma_i^z]$ is the Pauli vector describing the components of spin i , and \hbar is Planck's constant. B_i^z is the z -component magnetic field experienced by each spin, and it includes both a large 0.5 T external magnetic field and the smaller hyperfine field. The quantization axis (z -direction) is defined by the external magnetic field direction. The x - and y -components of the hyperfine field are neglected in this Hamiltonian since their sizes are negligible compared to the external magnetic field. B_i^z also has units of frequency. As shown in Fig. 3.2(b), we find that when we increase the gate voltage B_2 , which means lower

the barrier block, before the coupling J_2 gets high, J_3 would decrease rapidly to 0. This makes it challenging to tune all exchange couplings together.

To explain this, we have developed two models: the Heitler-London (HL) model and the exponential model. Here, we will focus primarily on the HL model, which we use to find how the dot locations shift when interdot barriers are raised or lowered. For double dots, we choose the Double Gaussians potential [45]:

$$V(x, y) = -V_0 \left[\exp\left(\frac{-(x-a)^2}{l_x^2}\right) + \exp\left(\frac{-(x+a)^2}{l_x^2}\right) \right] \exp\left(\frac{y^2}{l_y^2}\right), \quad (3.44)$$

where x and y are coordinates in the plane of the two-dimensional electron gas, and V_0 , a , l_x , l_y characterize the potential wells of the dots. Double Gaussians of this type are commonly used to model double dots, but usually a separate barrier term is included, as in Ref. [45]. Our simulated potential is shallow enough that a separate barrier term is not required to reproduce the potential we simulate.

Based on Ref. [45], the exchange coupling between two quantum dots in a potential of the form Eq. 3.44 in the Heitler-London (HL) framework at zero magnetic field is

$$J_{HL}(V_0, a) = \frac{2S^2}{1-S^4} \left\{ \frac{\hbar^2 a^2}{ml_0^4} - \frac{2V_0 l_x l_y}{\sqrt{(l_x^2 + l_0^2)(l_y^2 + l_0^2)}} \left[\exp\left(\frac{-(2a)^2}{l_x^2 + l_0^2}\right) - 2 \exp\left(\frac{-a^2}{l_x^2 + l_0^2}\right) \right] - \sqrt{\frac{\pi}{2}} \frac{e^2}{4\pi\epsilon\epsilon_0 l_0} \left[1 - SI_0\left(\frac{a^2}{l_0^2}\right) \right] \right\}, \quad (3.45)$$

where $S = \exp(-a^2/l_0^2)$, $l_0 = \sqrt{\hbar/m\omega_0}$, with $\omega_0 = \sqrt{V_0/ml_x^2}$. m is the electron effective mass, ϵ_0 is the permittivity of free space, ϵ is the dielectric constant of the material, and I_0 is the zeroth order modified Bessel function. In writing this equation, we have assumed that the minima of the double-dot potential occur at $x = \pm a$. We have also ignored the magnetic-field-dependent terms, because for the magnetic field used here (0.5T), the effective

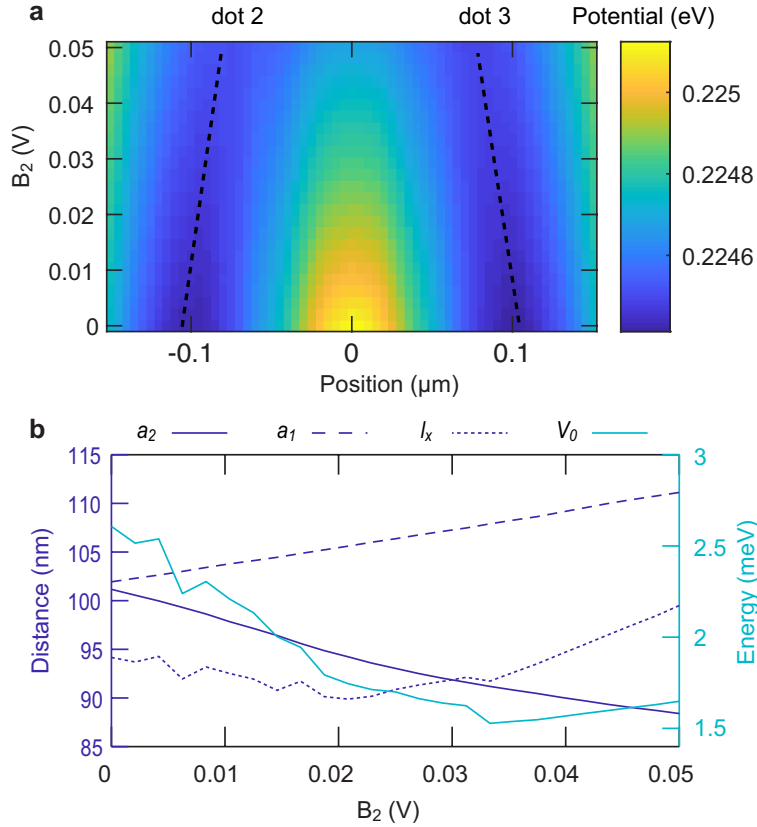


Figure 3.3: Electrostatic simulations. (a) Linecuts of the simulated potential associated with dots 2 and 3 vs. the barrier voltage pulse B_2 . The left dip is the potential of dot 2, and the right dip is the potential of dot 3. The dots move closer together as B_2 increases. The dashed lines are guides to the eye. (b) Fitted parameters of the simulated double-dot potential vs. B_2 . Based on the simulated potential of dot 1 (not shown), we also find that dots 1 and 2 move farther apart during the sample pulse.

magnetic confinement is still weaker than the electrostatic confinement. Utilizing this model we can do simulations to find the right parameters for the experiments. And we find the dots are shifted when one changes the barrier voltage. This result is shown in Fig. 3.3.

The result of the simulation agrees with the experiment as shown in Fig. 3.4. From Fig. 3.4(a) to (c) the order of the experiments should not be changed. At the beginning, all the barriers B_i are fully blocking J_i (corresponding to all 0 values), which does not allow the electrons to interact with each other. And the first step is to lower B_1 and find every value of J_1 while

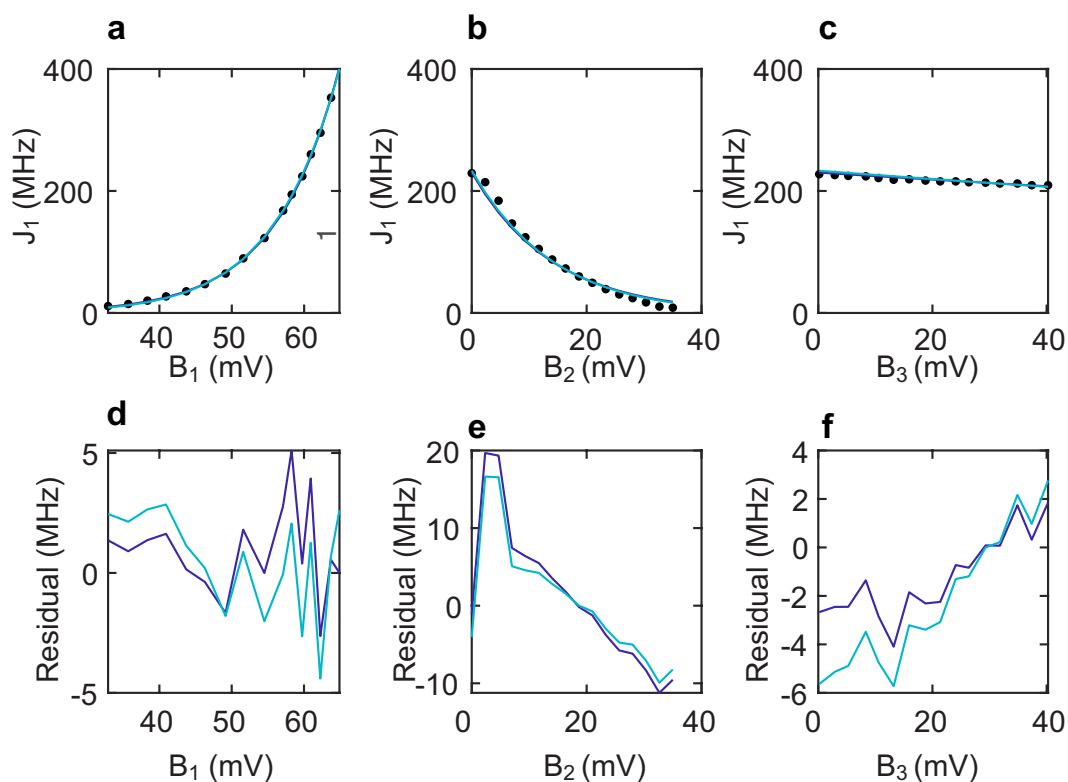


Figure 3.4: J_1 vs. B_j . (a) J_1 vs. B_1 . (b) J_1 vs B_2 , for $B_1 = 60$ mV. (c) J_1 vs. B_3 , for $B_1 = 60$ mV. The black data points in each panel are obtained from the fast Fourier transform of a dataset similar to Fig. 3.2(b). In (a)-(c), the dark blue line is the fit to the exponential model, and the light blue line is the fit to the HL model. Panels (d)-(f) show the difference between the fits and the data for the two models.

changing B_1 as shown in Fig. 3.4(a). We find J_1 grows with B_1 in this process. In the second step, we fix the value of $B_1 = 60\text{mV}$, and lower B_2 to scan J_1 as shown in Fig. 3.4(b). We find J_1 decays as B_2 increases. The last step is to tune B_2 back to 0 at the end of the first step and start to increase B_3 . We find J_1 does not depend much on B_3 . Both of the models (HL and exponential model) agree with the experiments. The difference of these two models as shown in Fig. 3.4(d)-(f).

In this work, we showed how to control Heisenberg exchange energy in a quantum dot spin chain. This method is scalable and also has the potential to be used in other quantum dot systems. Using these techniques, recently, Prof. John Nichol's group have implemented further experiments [46] to realize time crystals, which can improve the swap gates in the case of pulse imperfections [47, 48]. Time crystals are just one example of many interesting spin chain phenomena that can be realized in these systems provided there is sufficient control over the exchange couplings. Our work can be used to help realize this potential in future experiments.

Chapter 4

Negative exchange energy in quantum dots

The work discussed in this chapter, excepting Sec. 4.2, was published as:

Kuangyin Deng, F. A. Calderon-Vargas, Nicholas J. Mayhall, and Edwin Barnes. “Negative exchange interactions in coupled few-electron quantum dots.” *Phys. Rev. B* **97**, 245301 (2018) [49].

Reuse with permission from the American Physical Society. Copyright (2018) by the American Physical Society.

I contributed in calculating all the analytical and numerical results under the supervision of Prof. Edwin Barnes. All authors have participated in discussing and analyzing the results and contributed in writing the manuscript.

4.1 Introduction

As we have discussed in Chapter 2, semiconductor quantum dot spin systems are promising candidates for implementing a quantum computer due to their scalability [1, 3, 25], long coherence times [27, 28, 50, 51], and rapid gate operations [30, 31, 32]. We also discussed qubits encoded in different ways using the spin states of one or more electrons trapped in

one or more quantum dots, among these the single-spin [28, 52, 53, 54, 55, 56], singlet-triplet [27, 30, 31, 57, 58, 59, 60], resonant exchange [32, 35, 36, 37], and hybrid spin [38, 39, 40, 61, 62] qubits have been successfully implemented in the laboratory. In many of these systems qubits are coupled to each other by means of the tunneling-based effective exchange interaction, which has the advantage of producing fast gates controlled electrically with gate voltages. [27, 30, 63]. Furthermore, it has been recently demonstrated that symmetric exchange pulses substantially reduce the sensitivity of qubit gates to charge noise [64, 65, 66, 67, 68, 69, 70, 71].

Notwithstanding these advantages, the short-ranged nature of the exchange coupling [72, 73] is a potential hindrance towards scalability. However, this limitation can be circumvented by using an intermediate quantum system as a mediator [74, 75, 76], for example a multi-electron quantum dot [77, 78, 79]. In this line, Refs. [2, 80] study the spin properties of a multielectron GaAs quantum dot (with an estimated number of electrons between 50 and 100) exchange coupled to a single-electron quantum dot, which in turn is coupled to another single-electron quantum dot. This linear three-dot system is studied under magnetic fields both parallel and perpendicular to the two-dimensional electron gas (2DEG). In particular, the aforementioned works show that, at the transition between odd and even occupation number, the multielectron ground state is singlet-like for small hybridization and becomes triplet-like once the central electron has totally moved to the multielectron dot. As a result, the usually positive exchange energy becomes negative, even at zero magnetic field. This finding is not only important for understanding the properties of multielectron quantum dots, but also for performing dynamical decoupling on exchange-coupled spins. If the exchange coupling is restricted to be nonnegative, then special techniques are needed to dynamically correct for noise errors during gate operations [11, 12, 13], which generally leads to longer gate times. Instead, if the exchange coupling can be tuned to both positive and negative

values, then standard decoupling techniques can be used [81], and this issue is avoided.

It has been demonstrated that negative exchange energy in a quantum dot with just two-electrons can be induced by a non-zero out-of plane magnetic field [4, 5, 6, 7]. Here, the out-of-plane magnetic field leads to a compression of the orbital wave functions and a larger electron-electron repulsion, which makes triplets energetically favorable. However, an in-plane or zero magnetic field does not create a wave-function compression, and thus it does not induce a negative exchange energy in a doubly occupied quantum dot, i.e. the ground state is always the singlet. In fact, there is a two-electron ground state theorem [9, 10], which states that in the absence of spin or velocity-dependent forces (the force exerted by the in-plane magnetic field is negligible since it is along the strong confinement perpendicular to the 2DEG) the state of lowest energy must be non-degenerate. An extension of the two-particle theorem to an arbitrary number of particles is given in Ref. [9]. This theorem correctly predicts the ground state of many electrons in a linear array, as shown in Ref. [82]. Nonetheless, the multielectron ground state theorem does not apply to electrons interacting with central forces [9] and, for the multielectron quantum dot, the lower full orbitals do exert an effective central force onto higher orbitals. Therefore, there is no fundamental theorem or principle that prevents a triplet-like eigenstate from being the ground state of a multielectron quantum dot, regardless of the magnitude and direction of the magnetic field, as demonstrated in recent [2, 80] and earlier [83, 84] experiments with multielectron quantum dots.

In this chapter we demonstrate that a quantum dot does not require tens of electrons to exhibit negative exchange energy; instead, as few as four electrons are enough to have a triplet-like ground state in a quantum dot with zero magnetic field. We do this by performing a detailed numerical analysis employing the CI method with up to 14 electrons in both GaAs and Si quantum dots. Moreover, we use the full CI to determine the ground state of an

elliptically shaped four-electron quantum dot with different eccentricities and, in doing so, we identify a threshold, in both GaAs and Si quantum dots, at which the exchange energy flips sign.

This chapter is divided in four sections. In Sec. 4.3, we use a simple Hubbard model to study and give a general picture of the system presented in Ref. [2]. Then, in Sec. 4.4, we use a CI method to determine the ground state of a multielectron quantum dot with parabolic potential, where we consider different number of electrons and dot sizes. Moreover, a full CI calculation shows that for four electrons the ground state is triplet-like for all the dot sizes we considered. Finally, in Sec. 4.5, we use the full CI method to calculate the exact eigenenergies of four electrons confined in an elliptically shaped quantum dot, showing the effect of the dot asymmetry in the occurrence of triplet-like ground states.

4.2 The negative exchange energy experiment

In this section, we review the experiment implemented by the Copenhagen group showing negative exchange energy [2]. The device is shown in Fig. 4.1(a). Three gates V_L , V_M and V_R control the chemical potential of the quantum dots respectively. The cartoon also shows the electron numbers in the quantum dots approximately. The left and middle dots are small and contain only one or two electrons. Thus the electrons will only occupy the lowest orbitals in these dots. The right dot is very large, and it contains about 100 electrons. To provide one electron to pair up with the electron in the middle dot, we need the exact number of electrons in the large dot to be odd, which can be written as $2N + 1$, where N is an integer. Fig. 4.1(b) shows the charge configuration as a function of the gates. The two arrows ζ and ε show the trajectories in configuration space (dot occupancy) as the voltages are tuned in the experiment. The voltage control sequence that implements these trajectories

and the corresponding occupations are shown schematically in Figs. 4.1(c) and 4.1(d). One begins by initializing the state with two electrons in the left dot forming a singlet. After this preparation, one changes the detuning to let one electron hop into the middle dot (following the arrow labeled ζ) and then subsequently into the large dot (following the arrow labeled ε). After some time of interaction, one tunes the detuning back to its original value to let the the electron come back to the left dot. Then one can implement readout.

The results of this experiment are shown in Fig. 4.2. Fig. 4.2(a) shows the return probability for each of the detunings (ζ and ε). The black lines indicate the leakage of the original state, which can be translated into the energy energy spectrum shown in Fig. 4.2(b). This technique is very similar to the two-dot one described in Fig. 2.4(C). In Fig. 4.2(b), when $\varepsilon < 0$, the effective exchange J is positive. However, when $\varepsilon > 0$, the effective exchange between the middle and right dots becomes negative, which means that the triplet state $|\uparrow\rangle |T_0\rangle$ has lower energy than the singlet $|\uparrow\rangle |S\rangle$.

This result is unusual in quantum dot systems, as we explain further in the next section. To explain this experiment, we have to include orbital effects in the large quantum dot, which would cause the famous Hund's rule. In the next section, we present a theory based on a Hubbard model that reproduces the main features of the experimental data.

4.3 Hubbard model and Hund's rule

We start our analysis with a simple Hubbard model that describes the system studied in Ref. [2], i.e. a multielectron quantum dot (rightmost) with $2N + 1$ electrons ($N = 50$) tunnel-coupled to a double quantum dot containing two electrons, see Fig. 4.3. We keep as many orbitals (single-particle energy levels) as necessary in the right dot and only one orbital in each of the other two quantum dots (see Fig. 4.4(a)). The system's Hamiltonian

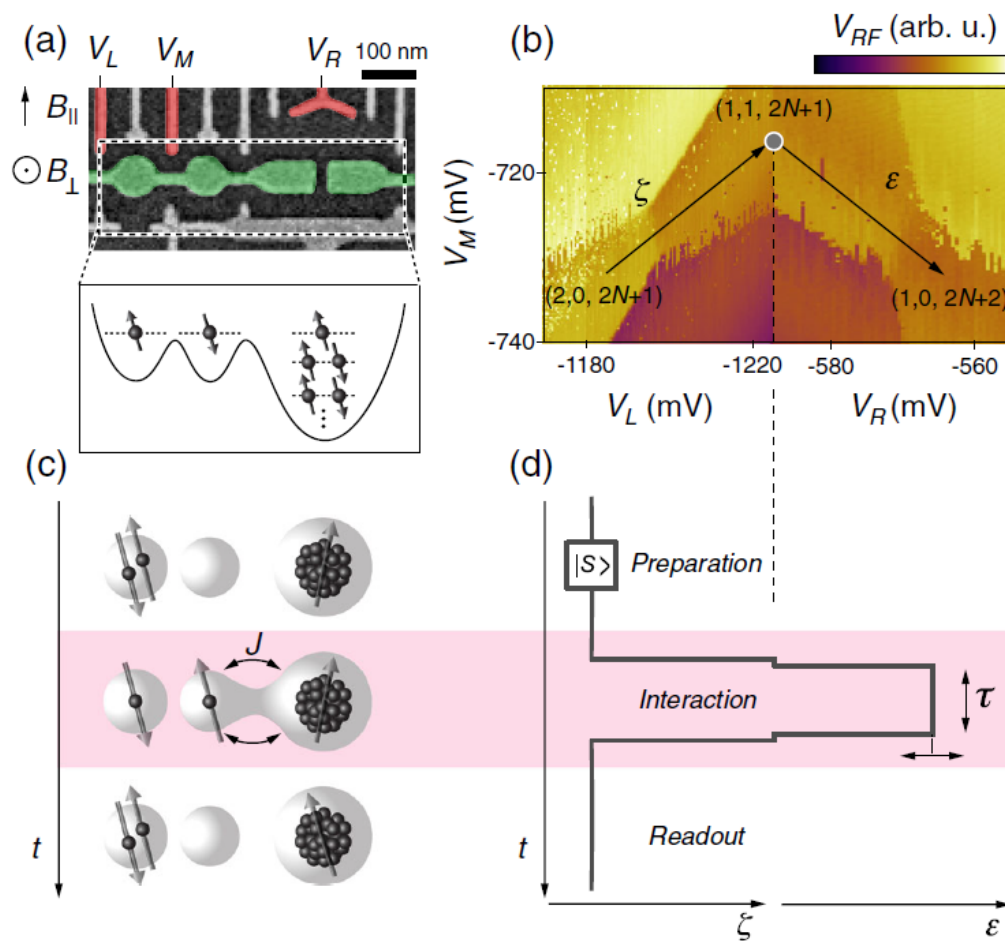


Figure 4.1: (a) Device and cartoon illustration. Two small and one large quantum dot with about 100 electrons. In the large dot the electron number is odd. (b) Charge diagram of the system. The experiment was implemented by tuning of the detunings ζ and ϵ , which alter the dot occupancies as shown. Every point on this path will be tested. (c) and (d) the experiment procedure illustration. We start from the state, in which we have two electrons in the left dot forming a singlet. We then change the detuning to let one electron jump into the middle dot (following the arrow labeled ζ) or the large dot (following the arrow labeled ϵ) and interact for time τ with the large quantum dot on the right. After the interaction, we change the detuning back to the preparation stage and measure the return probability. Adapted from Ref. [2].

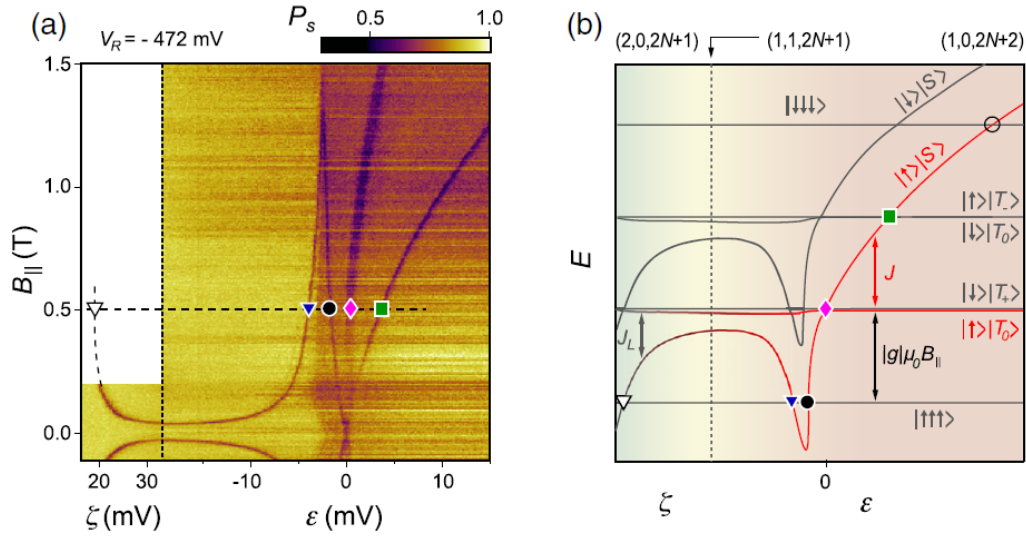


Figure 4.2: (a) The measured singlet return probability for different detunings and in-plane magnetic field. The black curve indicates the leakage, which is very similar to the process in Fig. 2.4(C). (b) The mapping to the energy from (a). For $\varepsilon < 0$, the effective exchange energy J between the middle and right dots is positive. But for $\varepsilon > 0$, this J becomes negative, which indicates that singlet $|\uparrow\rangle|S\rangle$ has higher energy than the triplet $|\uparrow\rangle|T_0\rangle$ for the middle and right dot. Adapted from Ref. [2].

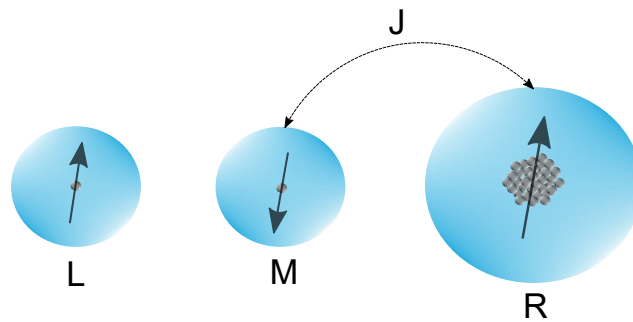


Figure 4.3: Illustration of the three dot system, where the L and M dots form a two-electron double quantum dot and R is the multielectron quantum dot. In the main text, we analyze the effective exchange interaction, J , between the middle (M) and right (R) quantum dots.

is

$$H = H_0 + H_z + H_A + H_U, \quad (4.1)$$

where

$$H_0 = \sum_{\sigma} \left[\sum_l \epsilon_{R,l} n_{R,l\sigma} + \epsilon_M n_{M,\sigma} + \epsilon_L n_{L,\sigma} - \sum_l t_{MR,l} (c_{R,l\sigma}^{\dagger} c_{M,\sigma} + c_{M,\sigma}^{\dagger} c_{R,l\sigma}) - t_{LM} (c_{M,\sigma}^{\dagger} c_{L,\sigma} + c_{L,\sigma}^{\dagger} c_{M,\sigma}) \right], \quad (4.2)$$

$$H_Z = \frac{E_B}{2} \left[\sum_l (n_{R,l\uparrow} - n_{R,l\downarrow}) + n_{M,\uparrow} - n_{M,\downarrow} + n_{L,\uparrow} - n_{L,\downarrow} \right], \quad (4.3)$$

$$H_A = A_R \sum_l (c_{R,l\uparrow}^{\dagger} c_{R,l\downarrow} + c_{R,l\downarrow}^{\dagger} c_{R,l\uparrow}) + A_{L,M} (c_{M,\uparrow}^{\dagger} c_{M,\downarrow} + c_{M,\downarrow}^{\dagger} c_{M,\uparrow} + c_{L,\uparrow}^{\dagger} c_{L,\downarrow} + c_{L,\downarrow}^{\dagger} c_{L,\uparrow}), \quad (4.4)$$

$$H_U = \sum_l U_{R,l} n_{R,l\uparrow} n_{R,l\downarrow} + \sum_{l_1 \neq l_2, \sigma, \sigma'} U_{R,l_1 l_2} n_{R,l_1 \sigma} n_{R,l_2 \sigma'} + U_M n_{M,\uparrow} n_{M,\downarrow} + U_L n_{L,\uparrow} n_{L,\downarrow} + \sum_{l_1 \neq l_2, \sigma, \sigma'} U_{R,l_1 l_2 l_2 l_1} c_{R,l_1 \sigma}^{\dagger} c_{R,l_2 \sigma'}^{\dagger} c_{R,l_1 \sigma'} c_{R,l_2 \sigma}. \quad (4.5)$$

Here, $n_{\alpha,l\sigma} = c_{\alpha,l\sigma}^{\dagger} c_{\alpha,l\sigma}$ is the number operator for the single-particle states in the left (L), middle (M), and right (R) quantum dot ($\alpha = L, M, R$; $\sigma = \uparrow, \downarrow$; and l is the right dot's l -th single-particle state), $\epsilon_{\alpha,l}$ denotes the single-particle energies, $t_{\alpha\beta}$ is the tunneling amplitude between dots ($\alpha, \beta = L, M, R$), E_B is the Zeeman energy, A_{α} is the hyperfine interaction (proportional to the dot size) between electrons and the nuclear spin bath, U_{α} is the ‘‘on-site’’ Coulomb interaction, and finally, $U_{R,l_1 l_2}$ and $U_{R,l_1 l_2 l_2 l_1}$ are the Coulomb interaction and exchange term between orbitals l_1 and l_2 in the right dot, respectively. The large number of electrons in the right dot makes the numerical calculation of the eigenenergies too difficult to carry out without any sort of approximation. Accordingly, we make use of the so-called ‘‘frozen-core’’ approximation (FCA), where we keep the right dot's $2N$ core electrons in the lowest non-interacting states and only allow a valence electron to occupy higher energy levels. It is worth mentioning that, due to the large number of core electrons, we are only considering

the direct Coulomb interaction between the core and the valence electrons, which causes a general energy shift. In the following sections we will consider cores with fewer electrons, and thus the FCA will also take into account the Coulomb exchange interaction between core and valence electrons.

In atomic physics, it is well known that in certain configurations a combination of electron-electron repulsion and electron-nucleus attraction makes high-spin states energetically more favorable than any other lower-spin state arising from the same configuration [85]; this is commonly known as Hund's multiplicity rule. Similarly, for the multielectron quantum dot the exchange term, $U_{R,l_1l_2l_2l_1}$, in Eq. (4.5) induces magnetic correlations among the electron spins and, as a result, it lowers the energy of the eigenstates with spin 1. This is more evident if we set $J_{R,l_1l_2}^F \equiv U_{R,l_1l_2l_2l_1}$ and, using Pauli matrix identities, we rewrite the exchange energy in Eq. (4.5) as we have derived in Chapter 3

$$\begin{aligned} & \sum_{l_1 \neq l_2, \sigma, \sigma'} U_{R,l_1l_2l_2l_1} c_{R,l_1\sigma}^\dagger c_{R,l_2\sigma'}^\dagger c_{R,l_1\sigma'} c_{R,l_2\sigma} \\ &= -2 \sum_{l_1 \neq l_2} J_{R,l_1l_2}^F (\mathbf{S}_{R,l_1} \cdot \mathbf{S}_{R,l_2} + \frac{1}{4} n_{Rl_1} n_{Rl_2}), \end{aligned} \quad (4.6)$$

where \mathbf{S}_{R,l_i} is the spin operator acting on the l_i -th single-particle state.

Since we assume that the $2N$ core electrons in the right dot are "frozen" (FCA), we are effectively dealing with a three-electron system. The spin Hamiltonian for three electrons coupled by nearest-neighbor exchange interactions and subject to a magnetic field is $H' = J_{LM} (\mathbf{S}_L \cdot \mathbf{S}_M - 1/4) + J_{MR} (\mathbf{S}_M \cdot \mathbf{S}_R - 1/4) - E_B (S_{z,L} + S_{z,M} + S_{z,R})$, where $J_{\alpha\beta}$ acts as an effective exchange interaction and E_B is the Zeeman energy. The eight spin eigenstates of

this Hamiltonian form a quadruplet Q ,

$$|Q_{+3/2}\rangle = |\uparrow\uparrow\uparrow\rangle, \quad (4.7)$$

$$|Q_{+1/2}\rangle = \frac{1}{\sqrt{3}}(|\downarrow\uparrow\uparrow\rangle + |\uparrow\downarrow\uparrow\rangle + |\uparrow\uparrow\downarrow\rangle), \quad (4.8)$$

$$|Q_{-1/2}\rangle = \frac{1}{\sqrt{3}}(|\uparrow\downarrow\downarrow\rangle + |\downarrow\uparrow\downarrow\rangle + |\downarrow\downarrow\uparrow\rangle), \quad (4.9)$$

$$|Q_{-3/2}\rangle = |\downarrow\downarrow\downarrow\rangle, \quad (4.10)$$

and high- and low-energy doublets, which, in the absence of tunneling between left and middle dots, have the following simple form

$$|D_{+1/2}\rangle = \frac{1}{\sqrt{6}}(-2|\downarrow\uparrow\uparrow\rangle + |\uparrow\downarrow\uparrow\rangle + |\uparrow\uparrow\downarrow\rangle), \quad (4.11)$$

$$|D_{-1/2}\rangle = \frac{1}{\sqrt{6}}(-2|\uparrow\downarrow\downarrow\rangle + |\downarrow\uparrow\downarrow\rangle + |\downarrow\downarrow\uparrow\rangle), \quad (4.12)$$

$$|D'_{+1/2}\rangle = \frac{1}{\sqrt{2}}(|\uparrow\uparrow\downarrow\rangle - |\uparrow\downarrow\uparrow\rangle), \quad (4.13)$$

$$|D'_{-1/2}\rangle = \frac{1}{\sqrt{2}}(|\downarrow\downarrow\uparrow\rangle - |\downarrow\uparrow\downarrow\rangle). \quad (4.14)$$

Here, the spin eigenstates $|D_{+1/2}\rangle$ ($|D_{-1/2}\rangle$) and $|Q_{+1/2}\rangle$ ($|Q_{-1/2}\rangle$) are almost degenerate, with an energy $E_{D_{\pm 1/2}} = \mp E_B/2$, whereas the low-energy doublets have an energy $E_{D'_{\pm 1/2}} = -J_{MR} \mp E_B/2$. Therefore, the effective exchange energy between the middle and right dots is given by

$$J_{MR} = E_{D_{+1/2}} - E_{D'_{+1/2}}, \quad (4.15)$$

where $|D_{+1/2}\rangle$ and $|D'_{+1/2}\rangle$ are the lowest spin triplet-like and singlet-like eigenstates, respectively.

We use the Hubbard model, Eq. (4.1), to calculate the energies of the aforementioned spin eigenstates. To that end, we choose a set of parameters such that the resulting energy

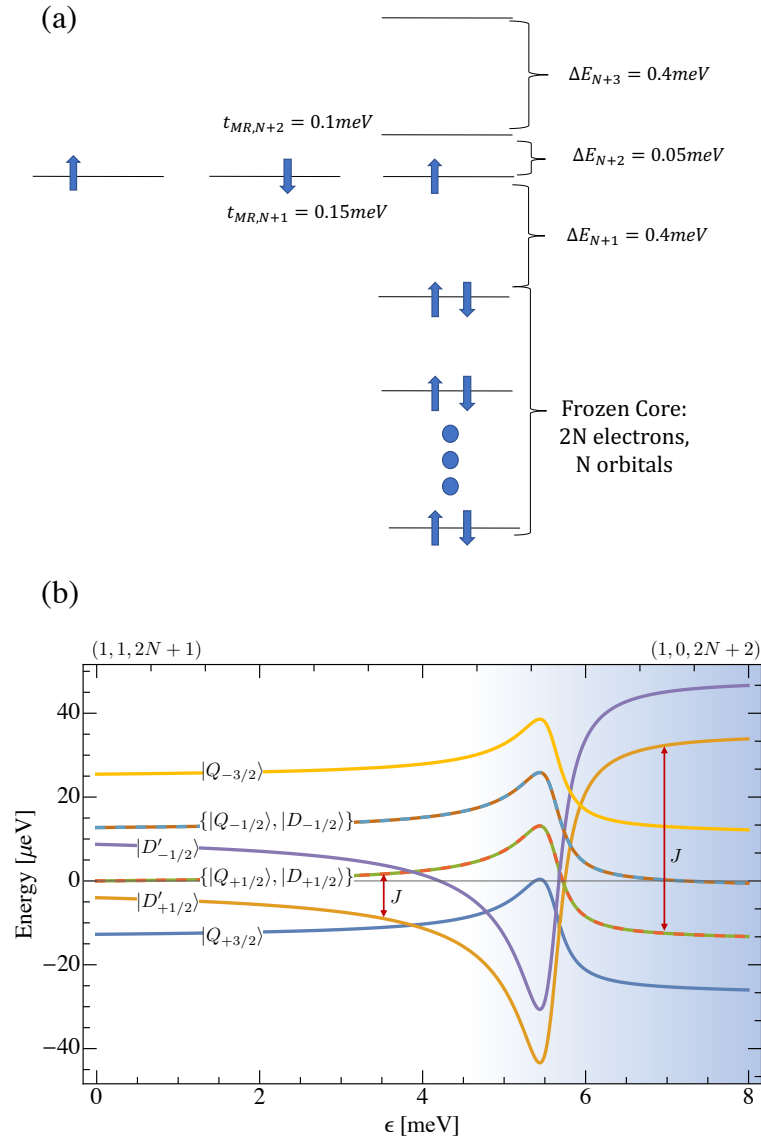


Figure 4.4: (a) Schematic of the energy levels and charge configuration for the three-dot system. Here, ΔE_i is the difference between two orbitals on the multielectron quantum dot. The schematic only shows the tunnel coupling between the middle and right dot, where $t_{MR,N+1}$ and $t_{MR,N+2}$ are the tunneling amplitudes between the middle dot's single-orbital and the lowest two orbitals above the frozen core in the multielectron quantum dot. (b) Eigenenergy spectrum, calculated as a function of the detuning ϵ , for the three-dot system at the transition between $(1, 1, 2N+1)$ and $(1, 0, 2N+2)$ charge configurations. The eigenstates $|D_{+1/2}\rangle$ ($|D_{-1/2}\rangle$) and $|Q_{+1/2}\rangle$ ($|Q_{-1/2}\rangle$) are almost degenerate and the exchange energy J is the difference between the triplet-like state $|D_{\pm 1/2}\rangle$ and the singlet-like state $|D'_{\pm 1/2}\rangle$.

spectrum resembles the one reported in Ref. [2]. Accordingly, we set the magnitude of the energy level splittings as $\Delta E_{N+1} = 0.4\text{meV}$, $\Delta E_{N+2} = 0.05\text{meV}$, $\Delta E_{N+3} = 0.4\text{meV}$, where $\Delta E_l = \epsilon_{R,l} - \epsilon_{R,l-1}$ and $\epsilon_{R,l}$ is the right dot's l -th single-particle energy level (see Fig. 4.4(a)). The tunneling amplitudes are $t_{MR,N+1} = 0.15\text{meV}$, $t_{MR,N+2} = 0.1\text{meV}$, and $t_{LM} = 0.02\text{meV}$. The hyperfine interactions for the multielectron quantum dot and double quantum dot are $A_R = 0.4\text{neV}$ and $A_{LM} = 4\text{neV}$, respectively. Finally, the ferromagnetic exchange term in the right dot is set equal to $J_{R,l_1l_2}^F = 0.1\text{meV}$ and the in-plane magnetic field is $B = 500\text{mT}$. With these parameters we plot in Fig. 4.4(b) the eigenenergies as a function of the detuning between left and right dot, $\epsilon \equiv (\epsilon_M - \epsilon_{R,N+1})/2$. Notice that in the $(1, 1, 2N+1)$ configuration, where (n_L, n_M, n_R) represents the number of electrons in the left, middle, and right dots, the singlet-like eigenstate $|D'_{+1/2}\rangle$ has lower energy than $|D_{+1/2}\rangle$ ($J_{MR} > 0$), but as soon as the middle dot's electron tunnels into the right dot the exchange energy becomes negative, i.e. $E_{D_{+1/2}} < E_{D'_{+1/2}}$. The latter is caused by the right dot's ferromagnetic exchange term $J_{R,l_1l_2}^F$, which lowers the energies of all two-electron states in the right dot with total spin equal to 1. This is analogous to Hund's rule in atomic physics.

Thus far, we have shown that, by choosing the appropriate parameters, the simple Hubbard model qualitatively reproduces the experimental results presented in Ref. [2]. Moreover, the model shows that the negative exchange energy is caused by the multielectron quantum dot exhibiting a spin triplet-like rather than singlet-like ground state. In this line, Ref. [80] presents comparable results using a Hubbard model similar to ours, with the difference that ours takes into account the hyperfine interaction (between electrons and the nuclear spin bath) and the Coulomb interaction between orbitals in the right dot. Nonetheless, the Hubbard model does not provide enough insight into the characteristics (minimum number of electrons, dot shape, etc.) a system must have in order to display a negative exchange energy under zero magnetic field. This is addressed below using a microscopic description

of the multielectron quantum dot.

4.4 Configuration interaction for a multielectron quantum dot

4.4.1 Frozen-core approximation

Here we determine the ground state of a multielectron quantum dot using a CI approach. The large number of electrons forces us to use, once again, the FCA, which now also takes into account the Coulomb exchange interaction between core and valence electrons.

The system can be described by the valence effective Hamiltonian [86, 87]:

$$\begin{aligned}
 H_v = & [E_v + \sum_i^{core} h_{ii} + \sum_{i<j}^{core} (ii|jj) - (ij|ji)] \\
 & + \sum_{r,s}^{val} \tilde{h}_{rs} c_r^\dagger c_s + \frac{1}{2} \sum_{p,q,r,s}^{val} (pq|rs) c_p^\dagger c_r^\dagger c_s c_q,
 \end{aligned} \tag{4.16}$$

with

$$(kl|mn) = \int \phi_k^*(r_1) \phi_l(r_1) \frac{1}{r_{12}} \phi_m^*(r_2) \phi_n(r_2) dr_1 dr_2, \tag{4.17}$$

where the single-particle orbitals are denoted by ϕ_α , and the summations marked “core” and “val” are over orbitals occupied by core or valence electrons, respectively. The terms inside the bracket in Eq. (4.16), which comprises the total single-particle energy of the valence electrons (E_v) and the core’s energy, add up to a constant, and thus they only shift the

energy scale. The energy term \tilde{h}_{rs} is defined as

$$\tilde{h}_{rs} = t_{rs} + \sum_i^{core} [(rs|ii) - (ri|is)], \quad (4.18)$$

where t_{rs} is the electron hopping between valence orbitals, and $(rs|ii)$ and $(ri|is)$ are the Coulomb interaction and exchange coupling between the valence and core electrons, respectively.

In our numerical analysis we consider $2N + 2$ electrons ($2N$ core electrons and 2 valence electrons, $0 \leq N \leq 6$) living in 12 orbitals. We model the lateral gate confinement of the multielectron quantum dot with a symmetric parabolic potential. Thus, the appropriate single-particle orbitals are the eigenstates of the Fock-Darwin Hamiltonian

$$H = \frac{1}{2m^*}(-i\hbar\nabla + \frac{e}{c}\mathbf{A})^2 + \frac{1}{2}m^*\omega^2r^2, \quad (4.19)$$

where m^* is the effective electron mass, $\hbar\omega$ is the quantum dot confinement energy, and $r = \sqrt{x^2 + y^2}$ is the radius. Following a numerical method developed in a previous work [43] and Chapter 3, and setting the external magnetic field to zero, we determine the eigenenergies and ground eigenstate of the valence effective Hamiltonian. We perform this calculation for both GaAs and Si quantum dots (see Table 4.1); using for GaAs (Si) the effective electron mass $m^* = 0.067m_e$ ($m^* = 0.19m_e$), where m_e is the electron mass, and the dielectric constant of the host material $\kappa = 13.1\epsilon_0$ ($\kappa = 11.68\epsilon_0$). In contrast to GaAs, Si quantum dots present a two-fold degenerate ground state. This valley degeneracy can be lifted and finely tuned by an out-of-plane electric field [28, 88]. Here, we assume that such techniques have been employed to achieve a sufficiently large valley splitting, and thus we do not include a valley coupling parameter in our calculations. A comprehensive analysis including valley effects would require a detailed microscopic understanding of the intervalley coupling, which

is likely device specific and is beyond the scope of this thesis.

Before discussing our results, it is important to note that the multielectron quantum dot has shells at $\eta = 2, 6, 12, 20, \dots, (n^2 + 3n + 2)$, where η is the total number of electrons in the dot and $n = 0, 1, 2, 3, \dots$ is the principal quantum number. This is a consequence of the $(n + 1)$ -fold degeneracy of the quantum dot's eigenenergies, which stems from the dot's effective confinement having a symmetry very close to circular [89]. We are primarily interested in situations where the multielectron quantum dot can be used as a spin qubit, i.e., it initially contains an odd number of electrons where all but one electron completely fill a number of shells and form a spin singlet-like state, leaving a net spin 1/2 from the remaining unpaired electron [43, 90, 91]. To examine the sign of the exchange interaction with a neighboring single-electron quantum dot we consider that the neighboring electron tunnels into the large quantum dot, giving now two valence electrons in that dot. We therefore consider first the simplest case involving just a pair of electrons, and then for larger number of electrons we focus on electron numbers $\eta = 4, 8, 14, \dots, (n_{max}^2 + 3n_{max} + 4)$, which correspond to two valence electrons and where n_{max} is the principal quantum number of the highest full shell in the core.

Our results, presented in Table 4.1, show that when the multielectron quantum dot contains only two electrons, only a singlet ground state can be realized; this is in accordance with the two-electron ground state theorem [9, 10]. Incidentally, in the case of valley degeneracy or near-degeneracy, a pair of electrons in a Si quantum dot would not necessarily follow the aforementioned theorem since electrons in different valleys could be treated as different species [92], which would violate the theorem's assumption that the potential is symmetric under permutations [9]. In Table 4.1 we also see that, for more than two electrons, triplet states are possible depending on the size of the dot. This indicates that having a core of electrons completely occupying lower energy orbitals is important for creating a triplet

Table 4.1: Ground states (S=Singlet and T=Triplet) for different dot sizes and number of electrons. Here, $\hbar\omega_0 = 1.0\text{meV}$ for both GaAs and Si quantum dots.

(a) Ground states table for GaAs.

ω/ω_0 # of electrons	0.25	0.5	1	2	4	8	16
2	S	S	S	S	S	S	S
4	T	T	T	T	T	T	T
8	S	T	T	T	T	T	T
14	S	S	S	S	T	T	T

(b) Ground states table for Si.

ω/ω_0 # of electrons	0.25	0.5	1	2	4	8	16
2	S	S	S	S	S	S	S
4	T	T	T	T	T	T	T
8	S	S	S	T	T	T	T
14	S	S	S	S	S	S	T

ground state. The fact that, at least for $\eta > 4$, whether the ground state is a singlet or a triplet depends on the size of the dot suggests that the orbital spacing plays an important role. We know that the energy difference between shells is inversely proportional to the square radius of the quantum dot, so that small dots present well defined energy gaps between shells. Consequently, for a pair of valence electrons above a full shell and for a sufficiently large energy gap between shells (small dot), Coulomb interactions between valence and core electrons are likely reduced since excitations from core to valence orbitals are suppressed. This picture is consistent with what we observe in Table 4.1, where for sufficiently small dots ($\omega/\omega_0 \geq 4$ for GaAs and $\omega/\omega_0 \geq 16$ for Si, where $\hbar\omega_0 = 1.0\text{meV}$) the ground state is always triplet-like, while for bigger dots ($\omega/\omega_0 \leq 2$ for GaAs and $\omega/\omega_0 \leq 8$ for Si) the comparatively larger Coulomb interactions between valence and core electrons increases the likelihood of singlet-like ground states.

4.4.2 Full configuration interaction for a four-electron dot

The FCA was instrumental in the calculation of the results presented in Table 4.1 and, therefore, it is important to probe the accuracy of this approximation. To that end, we use the full CI method to calculate the exact eigenenergies of a four-electron dot with variable size and zero magnetic field. In the numerical calculation we consider 4 electrons living in the 10 lowest orbitals of a parabolic potential. Our results show that the ground state of this system is triplet-like regardless of the dot size, in accordance with the results obtained through the FCA. We also notice that the higher-orbital-content of the ground state increases proportionally to the dot size. This is due to the reduction in the energy gap between orbitals when the size of the dot increases, which allows the mixing with higher orbitals. In this regard, the FCA only provides an estimation of the ground state's orbital content, and thus the FCA's accuracy is expected to diminish for large-size dots. Nonetheless, the FCA remains a good approximation within the dot size range considered in this work.

4.5 Full configuration interaction with elliptical potential

Apart from the dot size and number of electrons confined in a quantum dot, here we show that the shape of the dot also determines the occurrence of a triplet-like ground state. To that end we use, once again, the full CI method to calculate the exact eigenenergies of a four-electron quantum dot with elliptical potential and, in doing so, we show the effect of asymmetry on the exchange energy's magnitude and sign. In our calculation we consider 4

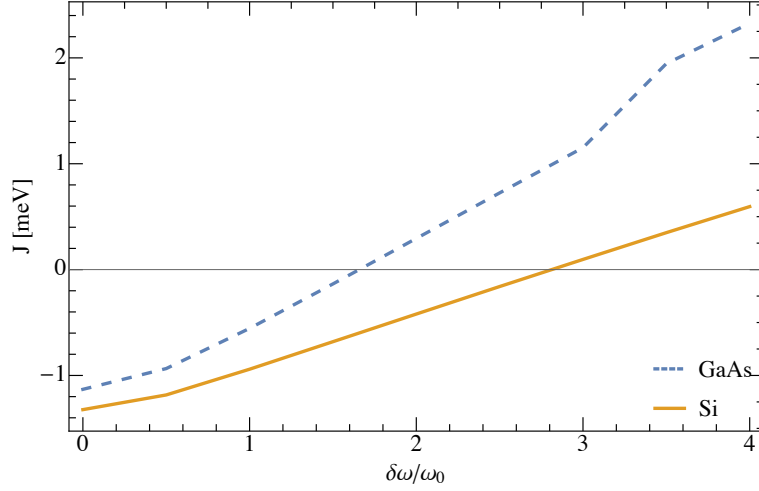


Figure 4.5: Exchange energy vs. frequency difference of the elliptical potential.

electrons residing in 10 orbitals, with a single-particle Hamiltonian given by

$$H = \frac{1}{2m^*}(-i\hbar\nabla + \frac{e}{c}\mathbf{A})^2 + \frac{1}{2}m^*(\omega_1^2x^2 + \omega_2^2y^2), \quad (4.20)$$

where ω_1 and ω_2 are the frequencies of the harmonic oscillators for the x and y directions, respectively. In the absence of an external magnetic field, $\mathbf{B} = 0$, the single-particle energies are the eigenvalues of the anisotropic two-dimensional harmonic oscillator:

$$\epsilon_{n_x, n_y} = \frac{1}{2}(\hbar\omega_1 + \hbar\omega_2) + n_x\hbar\omega_1 + n_y\hbar\omega_2, \quad (4.21)$$

where we define $\tilde{n} = n_x + n_y$. Here, it is evident that the splitting between single-particle energies can be tuned by the frequency difference

$$\delta\omega = \omega_2 - \omega_1, \quad (4.22)$$

which effectively changes the eccentricity of the dot's elliptical potential. Accordingly, we calculate the eigenenergies of the four electrons (in both GaAs and Si quantum dots with zero

magnetic field) using different magnitudes for $\delta\omega$, where, for convenience, we set $\frac{\hbar(\omega_2+\omega_1)}{2} = 8\hbar\omega_0 = 8meV$ and $\omega_2 \geq \omega_1$. Our results are summarized in Fig. 4.5, which shows the exchange energy J (given by the difference in energy between the lowest triplet-like and singlet-like eigenstates) as a function of the frequency difference $\delta\omega$. Notice that when $\delta\omega = 0$, i.e. the potential is parabolic, \tilde{n} becomes the principal quantum number and the principal energy levels (electron shells) corresponding to $\tilde{n} > 0$ are degenerate. Here, the electron distribution is such that the lowest shell is full and the next degenerate shell contains two electrons. In this configuration, as shown in the previous section, the ground state is triplet-like. However, for non-zero $\delta\omega$ the degeneracy is lifted and, in our particular case, when $\delta\omega$ is greater than a certain threshold $\delta\tilde{\omega}$ ($\delta\tilde{\omega} \approx 1.65\omega_0$ for GaAs and $\delta\tilde{\omega} \approx 2.8\omega_0$ for Si) the split between the formerly degenerate orbitals with $\tilde{n} = 1$ is large enough to favor a singlet-like ground state and, therefore, a positive exchange energy. This is because the triplet-like state would have to pay the gap energy. A similar effect is observed with larger numbers of electrons and/or larger dot sizes (see Table 4.1).

4.6 Conclusions

In this chapter we have studied the conditions under which negative exchange interactions can occur in coupled few-electron quantum dots. The negative exchange interaction between a multielectron quantum dot (with odd occupation number) and a single-electron quantum dot (which in turn is coupled to a second single-electron quantum dot) has its roots in the larger quantum dot exhibiting a spin triplet-like ground state, which occurs once the smaller dot's electron has tunneled into the larger dot. This was demonstrated using a Hubbard model for a linear three-dot system [93] that reproduces the experimental results presented in Ref. [2], where negative exchange was observed. The larger quantum dot with an even

number of electrons and zero magnetic field was further studied using a microscopic model based on the CI method with which we determined the ground state of the multielectron quantum dot. In this CI calculation we considered different combinations of total number of electrons and dot sizes (parabolic potential), showing that the occurrence of both triplet-like and singlet-like ground states depend on those parameters and that 4 electrons is the minimum needed to have a triplet-like ground state in both Si and GaAs quantum dots. Moreover, the effect of dot asymmetry on the exchange energy is also addressed via a full CI calculation of the energy spectrum for a four-electron quantum dot with elliptical potential. The full CI calculation is repeated for different eccentricities, revealing a threshold, in both GaAs and Si dots, at which the exchange energy flips signs. Future work will explore the equally interesting three-dot system where a multielectron quantum dot acts as a quantum mediator between two single-electron quantum dots. For now, the results presented in this work show that negative exchange interactions are robust in few-electron double quantum dots, and that all the potential advantages a tunable exchange interaction can provide are accessible with as few as 4 electrons in a double quantum dot. This is fundamental for scalability purposes since it avoids the need of large quantum dots, it prevents unwanted capacitive coupling between remote dots, and it enables simpler and faster dynamically corrected gate operations.

Chapter 5

Interplay of exchange and superexchange in triple quantum dots

The work discussed in this chapter was published as:

Kuangyin Deng and Edwin Barnes. “Interplay of exchange and superexchange in triple quantum dots.” *Phys. Rev. B* **102**, 035427 (2020) [94].

Reuse with permission from the American Physical Society. Copyright (2020) by the American Physical Society.

I contributed in calculating all the analytical and numerical results under the supervision of Prof. Edwin Barnes. I co-wrote the manuscript with Prof. Edwin Barnes.

5.1 Introduction

In the past few years, there has been rapid progress in improving gate fidelities and in scaling up to larger quantum dot spin arrays [28, 52, 55, 60, 61, 62, 95, 96, 97, 98, 99, 100, 101, 102, 103]. There have also been remarkable advances in creating long-distance spin-spin interactions using superconducting resonators [104, 105, 106, 107] or a large multi-electron quantum dot as a mediator of superexchange interactions [15, 74, 77, 108, 109]. As for most approaches to quantum computing, one of the current challenges in this field is to

determine suitable, scalable architectures that achieve high connectivity and controllability while maintaining long coherence times.

In all these types of quantum dot spin qubits, exchange interactions play a central role, either as a main driver of entanglement generation or as the primary single-qubit control mechanism in the case of qubits based on the spin states of two or three electrons. The difficulty in realizing negative exchange in the low-field, low-bias regime in turn limits the types of control schemes that can be employed to perform logic gates or dynamical decoupling [11, 12, 13].

However, it has been shown in recent experiments that the behavior of the exchange energy can be very different if there is a big multielectron quantum dot in the system [2, 14, 15]. These experiments reported negative exchange energies due to contributions from electrons in the higher orbitals of the big quantum dot. As described in the previous chapter, our subsequent theory work showed that it is possible to have a triplet ground state without a magnetic field by loading as few as four electrons into the big dot. It has also been experimentally demonstrated that multielectron quantum dots can be used to mediate strong superexchange interactions between spins that do not interact directly [15], a finding that was anticipated in earlier theory work based on a Hubbard model [74]. Together, these findings suggest that architectures based on arrays of smaller one-electron dots interspersed with larger multielectron dots may be a promising route to scaling up to larger quantum processors [79]. For instance, one could imagine a square 2d array of single-electron quantum dots with a large multielectron mediator at the center of each plaquette. A key outstanding question is whether one can selectively interact pairs of spins coupled to the same mediator by adjusting detunings and tunnel barriers.

In this chapter, we take a first step toward addressing this question by investigating the interplay of normal exchange and superexchange in triple quantum dot systems where one

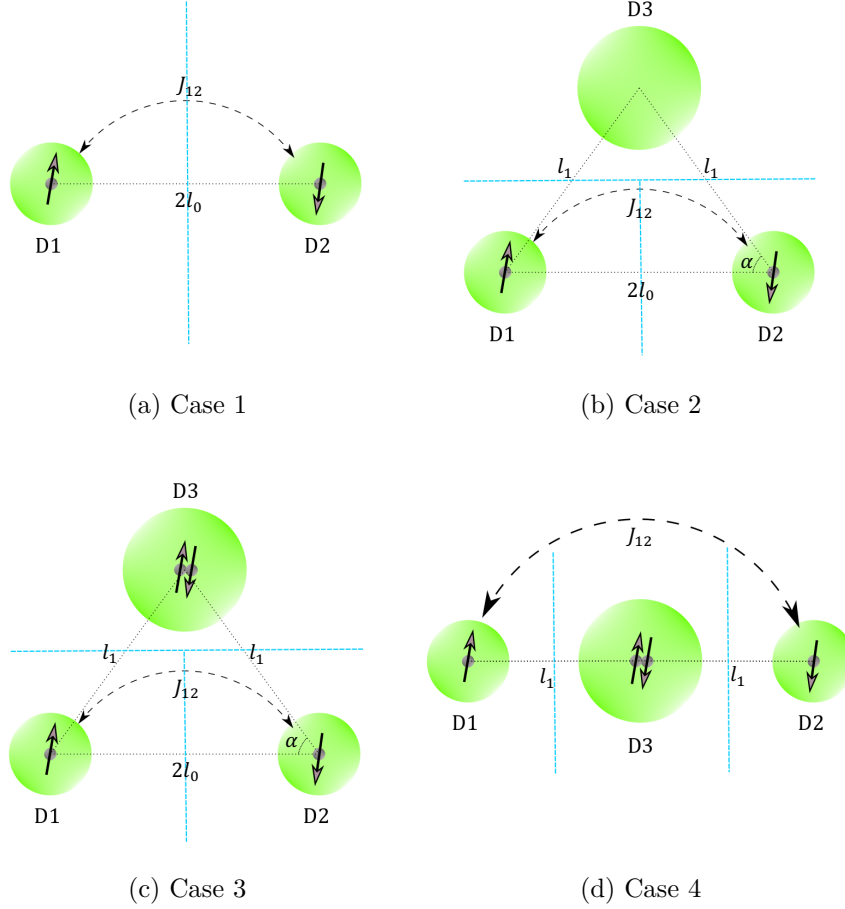


Figure 5.1: Four different quantum dot configurations studied in this work. D1 and D2 are small dots about 12.5 nm in radius, which corresponds to a confinement energy of $\hbar\omega_0 = 7.28$ meV. The x -axis is defined to pass through the centers of both D1 and D2. D3 is the mediator quantum dot, which is taken to have a radius of about 17.5 nm, which corresponds to a confinement energy of $\hbar\omega_1 = \frac{1}{2}\hbar\omega_0 = 3.64$ meV. The y -axis passes through the center of D3. Here, we fix $2l_0 = 56$ nm for cases 1, 2 and 3. We distinguish different triangular geometries in cases 2 and 3 by angle α ; the distance between the mediator and small dots, l_1 , is a function of α . The blue dashed lines in every case are the potential separation lines described in the main text. (a) The two-dot system. J_{12} is the exchange coupling between two dots, which are separated by $2l_0$. (b) The triangular system with two electrons. We adjust the detuning Δ to keep D3 empty. (c) The triangular system with four electrons. We confine two electrons in the big dot by adjusting the detuning parameter Δ . (d) Linear three-dot with four electrons. This can be thought of as a limit of case 3 in which we fix l_1 and rotate the two small dots D1 and D2 with respect to D3 until they are on a line. l_1 in this case is still a function of α as in case 3, and we also use α to adjust the inter-dot separation in this case.

of the dots is a large mediator. Using CI calculations, we explore how these two types of exchange evolve as the geometry and electron number in the dots are varied. Specifically, we compare four different cases: (i) a double quantum dot without the mediator, a triple quantum dot in a triangular configuration with (ii) two electrons or (iii) four electrons, and (iv) a triple quantum dot in a linear arrangement with the mediator in the middle. These cases are summarized in Fig. 5.1. Comparing these four cases allows us to distinguish effects due to electron number or dot detuning from those caused by the dot geometry. In the triangular configuration cases, we find that the mediator gives rise to a modest superexchange interaction when it is not occupied, but when two electrons are added to the mediator, this interaction becomes orders of magnitude stronger. We show that the same enhancement can also be obtained from the Hubbard model presented in Ref. [74], where we use CI calculations to compute the model parameters. We also find that the effective exchange exhibits non-monotonic behavior as the mediator moves away from the two smaller dots. In the linear configuration case, we find that including the mediator leads to a still stronger exchange coupling, along with a substantial extension of the interaction distance of the two remote spin qubits.

This chapter is organized as follows. In Sec. 5.2, we give details of the system Hamiltonian and the CI approach we use. We also compute the exchange energy for two electrons in two dots, which is used as a reference to compare against the triple-dot configurations. In Sec. 5.3, we investigate superexchange in the triangular dot configuration with two electrons. In Sec. 5.4, we study the effect of adding two electrons to the mediator, finding that superexchange is strongly enhanced as a consequence. In Sec. 5.5, we compare the triangular triple-dot case with four electrons to the linear triple-dot case. We present our conclusions in Sec. 5.6. An appendix contains additional details about our calculations and a detailed survey of the single-electron density for each of the triple-dot configurations considered.

5.2 Quantum dot model and exchange energy for double dot

We model each quantum dot by a 2d symmetric parabolic potential, and we include a uniform external magnetic field in the z direction, which is orthogonal to the plane of the dots. The Hamiltonian for N electrons is then

$$H_{i,N} = \sum_{k=1}^N \left[\frac{1}{2m^*} \left(-i\hbar\nabla_k + \frac{e}{c}\mathbf{A} \right)^2 + V_i(\mathbf{r}_k) + g^* \mu_B \mathbf{B} \cdot \mathbf{S}_k \right] + \sum_{j < k} \frac{e^2}{\kappa |\mathbf{r}_j - \mathbf{r}_k|}, \quad (5.1)$$

where $m^* = 0.067m_e$ is the effective electron mass for GaAs, m_e is the electron mass, $g^* = -0.44$ is the effective Landé factor, μ_B is the Bohr magneton, and the dielectric constant for this material is $\kappa = 13.1\epsilon_0$. Throughout this work, we set $\mathbf{B} = B_0\hat{z}$, where $B_0 = 0.845$ T. V_i is the total quantum dot potential for case i , where $i = 1, \dots, 4$ refers to one of the cases shown in Fig. 5.1.

Let us first consider a system of two small quantum dots without a mediator, as shown in Fig. 5.1(a) (case 1). In the following sections, we use this system as a reference against which we compare triple-dot configurations involving a mediator. The explicit form of the quantum dot potential in Eq. (5.1) for case $i = 1$ is

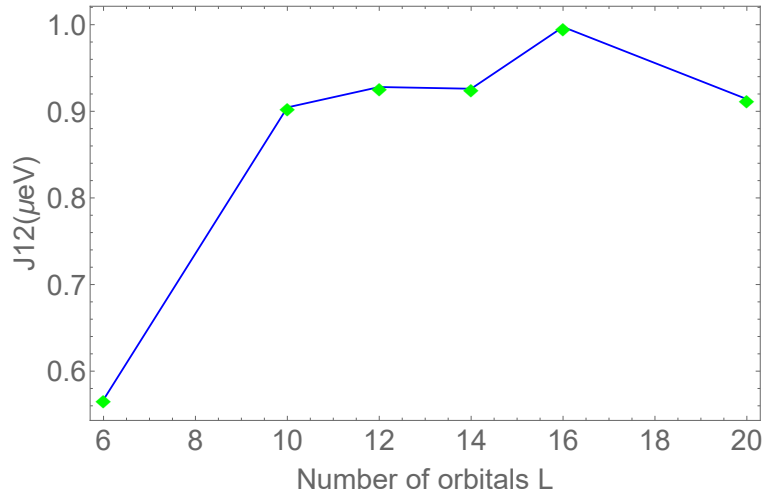
$$V_1(\mathbf{r}) = \frac{1}{2}\Theta(x)m^*\omega_0^2(\mathbf{r} - \mathbf{R}_{D2})^2 + \frac{1}{2}\Theta(-x)m^*\omega_0^2(\mathbf{r} - \mathbf{R}_{D1})^2. \quad (5.2)$$

Here, $\hbar\omega_0$ is the confinement energy for each dot, \mathbf{r} is the electron coordinate, and $r = \sqrt{x^2 + y^2}$ the corresponding radius. \mathbf{R}_{D1} and \mathbf{R}_{D2} are the coordinates of the dot centers for D1 and D2, respectively. The confinement energy of each dot is set to $\hbar\omega_0 = 7.28$ meV, which for $B_0 = 0.845$ T corresponds to a radius of about 12.5 nm, and the center-to-center separation between the two dots is 56 nm. $\Theta(x)$ is the unit step function, which is used to cut

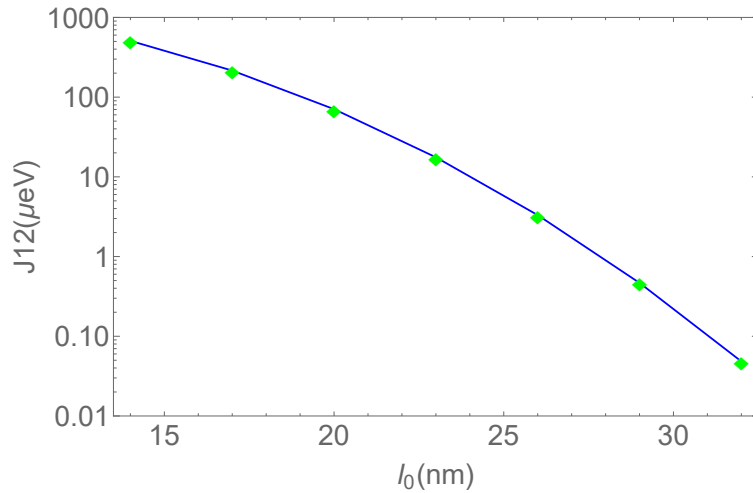
and glue the two harmonic oscillator potentials together along the $x = 0$ line, as indicated by the blue dashed line in Fig. 5.1(a) (case 1). Similar cuts are used in the triple-dot cases as well. This is explained further in the next sections.

To compute the eigenstates and energies of Eq. (5.1), we employ CI (e.g., exact diagonalization) following the approach used in the previous chapter. Our single-particle basis states are comprised of the Fock-Darwin states for each dot. Because the Fock-Darwin states from different dots are not orthonormal to each other, we use the Cholesky decomposition mentioned in Chapter 3 to obtain linear combinations of them that do form a fully orthonormal basis. One could also consider using a Gaussian grid basis instead; this has been shown to yield similar results to the present approach [90, 110]. After constructing our single-particle basis and truncating it to retain only the lowest L levels, we build our multi-particle states and compute matrix elements of the Hamiltonian with respect to these using the Slater-Condon rules in Chapter 3. We then extract the effective exchange energy J by computing the energy difference of the lowest-energy triplet $|T_0\rangle$ and singlet $|S\rangle$ states. We establish convergence by adjusting L until the results do not change significantly.

Fig. 5.2 shows our CI results for case 1, two electrons in two small dots. Here in Fig. 5.2(a), the orbital number is the total number of orthonormalized Fock-Darwin orbitals for the whole system. The energy levels of the Fock-Darwin states are $E_{n,m} = (n+1)\hbar\sqrt{\omega_0^2 + \omega_c^2/4} + m\hbar\omega_c/2$, where $\omega_c = eB_0/m^*c$ is the cyclotron frequency, n is a non-negative integer, and $m = -n, -n+2, \dots, n-2, n$ is the magnetic quantum number. In the limit of zero magnetic field, these levels form degenerate shells labeled by the quantum number n , where the degeneracy of the n th shell is $n+1$. For the relatively weak magnetic field considered here, for which $\omega_c = 2\omega_0/\sqrt{99}$, the levels in each shell are nearly degenerate. Because of this, one might expect that it is necessary to retain all the orbitals within a shell in order for results to converge [43]. Indeed, Fig. 5.2(a) shows that keeping other numbers of orbitals may lead to



(a) Exchange energy versus number L of single-particle orbitals used in CI calculation for two electrons in a double quantum dot.



(b) Exchange energy versus inter-dot half-distance l_0 .

Figure 5.2: (a) Exchange energy for two quantum dots with one electron each (see Fig. 5.1(a)) computed from CI as a function of the number L of single-particle orbitals ($L/2$ orbitals for each dot). Full orbital shells on each dot are retained when $L = 6, 12, 20$. (b) Exchange energy for two dots versus inter-dot half-distance l_0 from a CI calculation with $L = 12$ single-particle basis states.

slight inaccuracies in some cases (orbital numbers 6, 12 and 20 correspond to keeping full shells). Therefore, we choose to retain an integer number of shells in our CI calculations throughout this work to be safe. In Fig. 5.2(b), we show the exchange energy as a function of the inter-dot half-distance l_0 (measured from the center of D1 to the origin) on a logarithmic scale. As expected, the exchange energy falls off exponentially with the distance. We compare this result to what happens when the mediator dot D3 is placed at the origin in Sec. 5.5.

Before moving on to consider the effect of a mediator, it is worth pausing for a moment to discuss possible issues with using the infinitely confining biquadratic potential shown in Eq. (5.2). Potentials of this type are used throughout this thesis. Prior works showed that models based on infinite confinement potentials can produce erroneous exchange couplings at short inter-dot distances [111, 112]. These works found that the exchange energy exhibits a striking non-monotonic behavior below a critical distance that is on the order of the dot radius. However, in Fig. 5.2(b), the exchange coupling continues to rise smoothly at the shortest distances considered, as one would expect, while no indications of non-monotonic behavior are evident. It may be that the failure at short distances observed in Refs. [111, 112] is due more to the use of Heitler-London (HL) and Hund-Mulliken (HM) approximations rather than infinite confinement potentials. This interpretation is consistent with the fact that previous works employing CI to compute exchange energies of electrons confined to biquadratic potentials also obtained physically reasonable results [43, 90, 110]. We further support this conclusion by showing in Sec. 5.4 that our exchange coupling results are in agreement with those obtained from a Hubbard model; such models have been shown to work well even at distances where HL or HM models fail [112]. The model potentials we use will likely become unreliable at very short inter-dot separations, but this regime lies outside the scope of the present work, where our focus is on long-distance spin-spin interactions

between electrons in well separated dots. If one is interested in describing specific devices in which the dots are very close to each other, then a more reliable approach might be to use density functional theory calculations to construct the single-particle basis states rather than a model potential [113].

5.3 Triangular triple dot with two electrons

We now move on to case 2, which includes a third, larger dot as shown in Fig. 5.1(b). We expect that if the third dot is brought sufficiently close to the first two, then it can mediate superexchange interactions between the electrons on the two small dots. These superexchange interactions can potentially combine constructively or destructively with the normal exchange that still exists between the two small dots.

In order to compare directly with the results of case 1, we again fix the radius of the two small dots (D1 and D2) to about 12.5 nm and choose the center-to-center distance ($2l_0$) between them to be 56 nm. The larger mediator dot (D3) is chosen to have a confinement energy of $\hbar\omega_1 = \frac{1}{2}\hbar\omega_0 = 3.64$ meV, which corresponds to a radius of about 17.5 nm. The center of the dot is located on the positive y axis. The centers of these three dots form an isosceles triangle, and the angle between the base and one leg of the triangle is defined to be α . We match the three parabolic potentials of the three dots along a T cut that separates the plane into three regions as indicated with the blue dashed lines in Fig. 5.1(b). Each of these regions contains one of the dot potentials. The horizontal separation line is placed at $y = y_0$, where y_0 depends on the angle α in such a way that dot D3 remains almost entirely above this line in all cases. The precise manner in which y_0 is chosen for a given value of α is described in Appendix A. The remaining two regions are separated by the y -axis at $x = 0$.

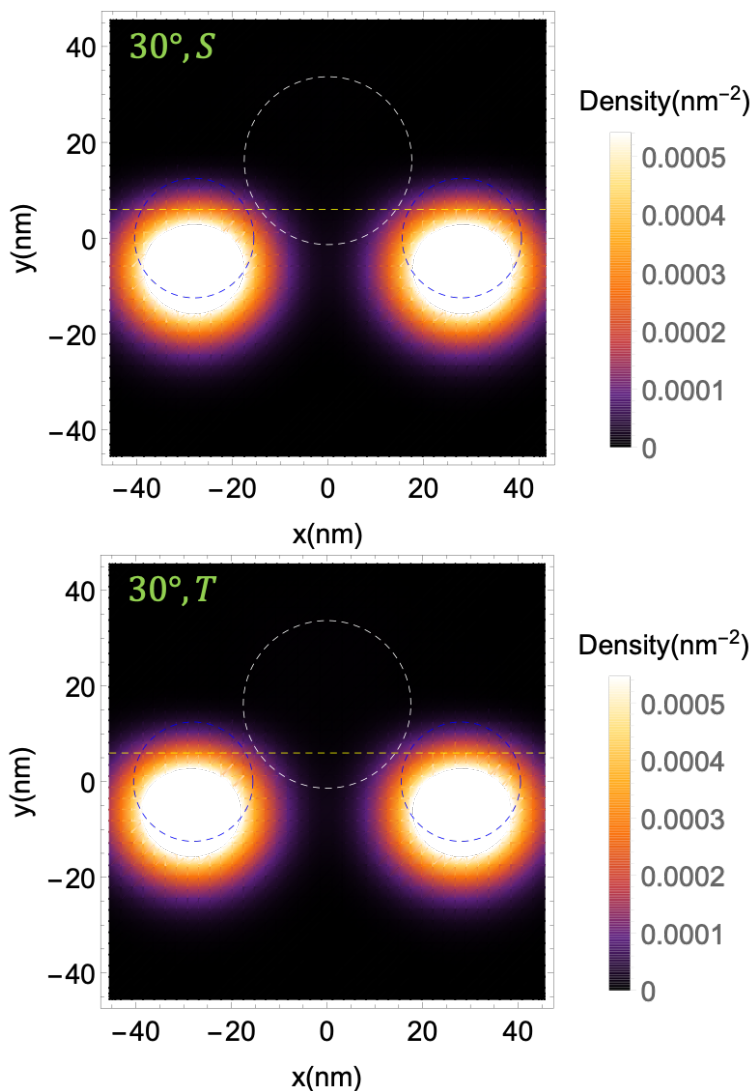


Figure 5.3: Single-particle density for two electrons in a triangular triple dot (case 2) for $\alpha = 30^\circ$. The upper (lower) panel shows the single-particle density for the lowest-energy singlet $|S\rangle$ (triplet $|T_0\rangle$). The yellow dashed line is the potential cut at $y = y_0$. The dashed circles mark the positions of the three parabolic dot potentials for this value of α . It is apparent that the centers of the electron density in the small dots are displaced downward. This is due to the large value of detuning Δ chosen to deplete the big dot. The distance between the two small dots remains the same, as does the normal exchange coupling between them.

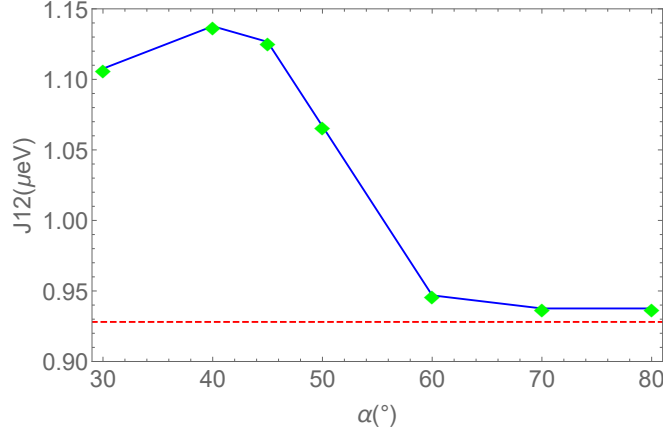


Figure 5.4: Effective exchange interaction between electrons on dots D1 and D2 as a function of angle α (see Fig. 5.1(b)) in the case of two electrons in a triangular triple dot (case 2). In the CI calculation used to obtain this result, we retain 6, 6 and 3 orthonormalized Fock-Darwin orbitals for D1, D2 and D3, respectively, corresponding to a total of $L = 15$ single-particle basis states. The red dashed line is the result for J_{12} from case 1 (two electrons in a double dot) using 12 single-particle orbitals. We see only modest contributions from superexchange processes in this case.

Thus, for case $i = 2$, the total quantum dot potential in Eq. (5.1) is

$$\begin{aligned}
 V_2(\mathbf{r}) = & \frac{1}{2}\Theta(y_0 - y)\Theta(x)m^*\omega_0^2(\mathbf{r} - \mathbf{R}_{D2})^2 \\
 & + \frac{1}{2}\Theta(y_0 - y)\Theta(-x)m^*\omega_0^2(\mathbf{r} - \mathbf{R}_{D1})^2 \\
 & + \Theta(y - y_0)\left[\frac{1}{2}m^*\omega_1^2(\mathbf{r} - \mathbf{R}_{D3})^2 + \Delta\right].
 \end{aligned} \tag{5.3}$$

In the last line of Eq. (5.3), we introduced the detuning parameter Δ for dot D3; this parameter applies a constant energy shift to all the levels in the mediator relative to the energy levels in the small dots, D1 and D2. For each angle α , we adjust Δ until dot D3 is empty of electrons, which we check by integrating the multi-particle density over the region above the horizontal blue dashed line in Fig. 5.1(b) to obtain the electron number in D3. Of course, one cannot make the electron number in D3 exactly zero, but it can be made very small, at least for $\alpha \geq 45^\circ$. For these angles, we can keep the electron number in D3 below

0.05e by choosing $\Delta = 20$ meV for all angles in this range. For smaller angles in the range $\alpha < 45^\circ$, reducing the electron number in D3 becomes more difficult, but we can still get it below 0.1e by setting $\Delta = 20$ meV.

The successful depletion of D3 is also visible in the single-particle density, which we calculate by integrating the multi-electron density over just one set of electronic coordinates. An example is shown in Fig. 5.3 for $\alpha = 30^\circ$. Increasing Δ until the big dot is almost vacant also causes the two small dots to move downward, as is evident in the figure. However, the separation between the electrons in the small dots remains unchanged for both the lowest-energy singlet and triplet state, hence the normal exchange interaction between them remains the same. Additional density plots for various angles can be found in Appendix A.

We now calculate the effective exchange interaction J_{12} between the electrons on dots D1 and D2. This interaction includes contributions from normal, nearest-neighbor exchange between D1 and D2 as well as a superexchange interaction mediated by dot D3. We compute J_{12} as a function of angle α ; this allows us to control the relative strength of the superexchange coupling compared to the normal exchange, because increasing α increases the distance between D3 and the other two dots. The result is shown in Fig. 5.4 (blue line with green points). We see that across a broad range of angles, the effective J_{12} exceeds the normal exchange interaction (dashed red line) that we obtain in the absence of the mediator. We attribute the difference between these two curves to superexchange processes. It is evident that, in this case, superexchange provides only a modest enhancement of the total effective exchange that is at most 20% of the normal exchange. This enhancement quickly fades as α increases beyond 50° (which corresponds to $l_1 = 43.56$ nm), although some evidence of superexchange remains visible in the large-angle regime. Interestingly, we also find non-monotonic behavior in J_{12} in the small angle regime, with a maximum near 40° . This may be because the downward shift of the electrons in D1 and D2 caused by Δ effectively increases

the distance to D3, leading to a small suppression of superexchange.

5.4 Triangular triple dot with four electrons

We now investigate the impact of increasing the number of electrons on the effective exchange coupling. In particular, we add two more electrons to the system, while keeping the form of the potential ($V_3 = V_2$) and almost all the parameters the same. The only parameter we change is Δ , which is now adjusted so that two electrons occupy D3 as in Fig. 5.1(c). The precise values used are given in Appendix A.

Before proceeding, we need to clarify the definition of J_{12} in the case where there are four electrons. For each possible occupancy of spatial orbitals, there are a total of 16 spin states, many of which are singlet-like and triplet-like. To compute the effective exchange energy, we identify the lowest-energy state with $S^{total} = 0$ and $S_z^{total} = 0$ as our singlet state $|S\rangle$ and the lowest-energy state with $S^{total} = 1$ and $S_z^{total} = 0$ as our triplet state $|T_0\rangle$. We then calculate J_{12} by taking the difference of the two corresponding eigenenergies. In all four-electron cases considered in this work, we confirm the suitability of this definition by verifying that the resulting $|S\rangle$ and $|T_0\rangle$ states have the property that the two electrons on D3 approximately form a singlet.

The one-electron density (obtained this time by integrating the full multielectron density over three sets of electronic coordinates) for $\alpha = 30^\circ$ is shown for both the lowest-energy singlet-like and triplet-like states in Fig. 5.5. It is evident in both cases that the electrons in D1 and D2 are displaced slightly downward as a consequence of D3, similarly to Fig. 5.3, while the two electrons on D3 undergo a more substantial upward shift. This is due to a combination of Coulomb repulsion and the fact that the confinement energy of D3 is much smaller than that of D1 and D2, which allows the electrons in D3 more freedom to move

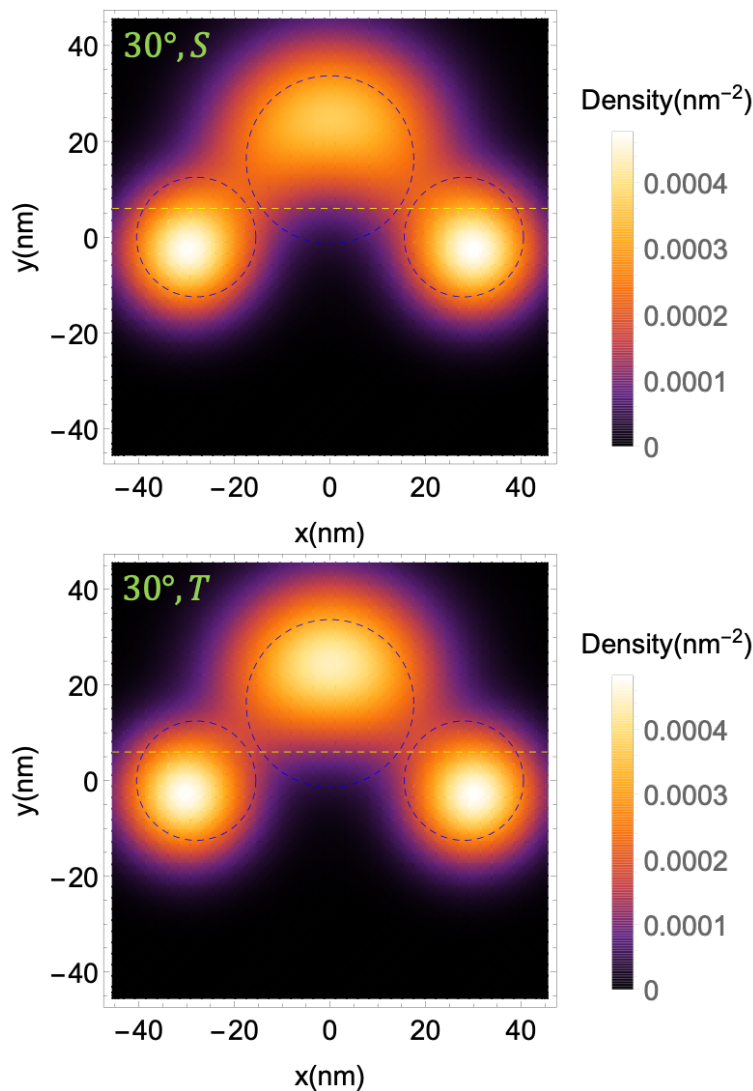


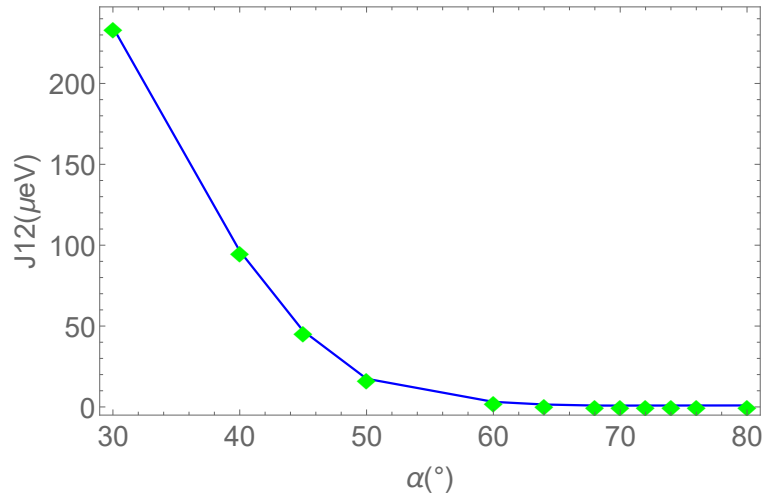
Figure 5.5: Single-particle density for four electrons in a triangular triple dot (case 3) with $\alpha = 30^\circ$. The upper (lower) panel shows the single-particle density for the lowest-energy singlet-like $|S\rangle$ (triplet-like $|T_0\rangle$) four-electron state. The yellow dashed line marks the potential cut at $y = y_0$. The blue dashed circles indicate the original positions of the three dots for this value of α . The electrons in the small dots are displaced slightly downward and outward, while the electrons in the big dot move upward due to Coulomb repulsion.

away from the other two electrons. Unlike the two-electron case, here the electrons in D1 and D2 are also pushed away from each other horizontally as a consequence of the Coulomb repulsion from the two electrons on D3, and this in turn can impact the normal exchange. As one would anticipate based on fermion statistics, it is also evident in Fig. 5.5 that the singlet density is more uniformly spread across the three dots compared to the triplet density. This is, of course, directly related to the nonzero superexchange energy. Additional plots of the single-particle density for other values of α can be found in Appendix A.

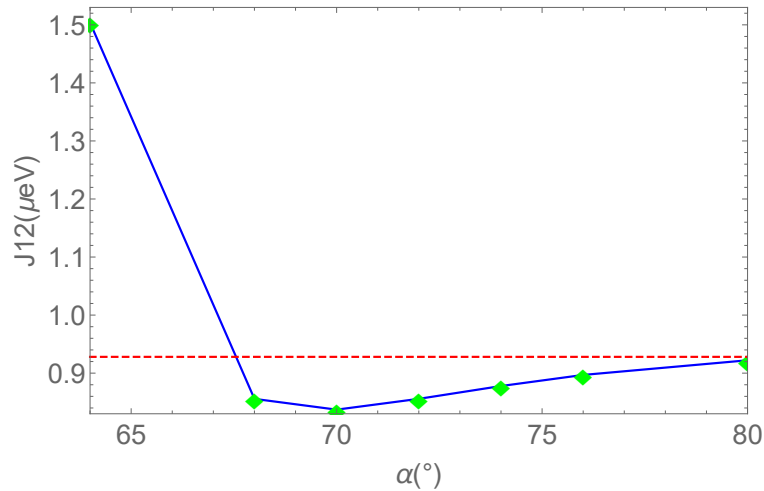
Next, we show that the inclusion of the two additional electrons compared to case 2 can either strongly enhance or weakly suppress the effective exchange interaction J_{12} depending on α . Our CI results for J_{12} as a function of α for case 3 are shown in Fig. 5.6. The most striking difference compared to the two-electron case considered in the previous section is that the effective exchange energy is more than two orders of magnitude larger in the low-angle regime (compare with Fig. 5.4). We can understand this as a consequence of Fermi statistics combined with the fact that the three quantum dot potentials are merging together in the low- α regime, which forces the four electrons to occupy the same space. This happens in the four-electron case because here we lower Δ substantially in order to keep two electrons trapped in the mediator. This is unlike the previous case where Δ was set to a large value to keep the mediator empty, which in turn keeps the potential similar to what it was in the case of two isolated dots (case 1). If we were to think of the triple-dot potential in case 3 (low Δ) as effectively one big dot D_{eff} , and if we neglect Coulomb interactions for the moment, then the ground state of the system would be a $S^{total} = 0$ state consisting of two pairs of two-electron singlets occupying the lowest two single-particle orbitals of D_{eff} . The lowest-energy state with $S^{total} = 1$ and $S_z^{total} = 0$ would be formed by moving one of the electrons to the second excited orbital, which produces an exchange splitting that is on the order of the level spacing of D_{eff} . In the present context, this is on the order of meV. (In case 2

where Δ is large, this splitting is very small because we have essentially two independent dots with nearly degenerate orbitals.) Restoring the Coulomb interactions reduces this splitting because the more symmetric spatial part of the $S^{total} = 0$ state incurs a larger Coulomb energy penalty, but the splitting can still remain large. Note that this mechanism is closely related to the notion of spin blockade in singlet-triplet qubits, where the singlet and triplet two-electron states are nearly degenerate when the electrons are separated into distinct dots, but when a large detuning is applied to one dot, the electrons are pushed into the same dot, opening a large energy gap between the singlet and triplet states [30]. In the next section, we show that the vertical shift of the mediator electrons due to Coulomb repulsion (Fig. 5.5) actually leads to a significant reduction in the superexchange in the small-angle regime compared to what would occur in the absence of this shift.

Fig. 5.6 shows that the effective exchange energy exhibits three different qualitative trends as a function of α . For $\alpha < 65^\circ$, J_{12} is dominated by a very strong superexchange interaction mediated by D3 as discussed above. For $\alpha > 72^\circ$, J_{12} quickly converges to the value obtained in the two-electron case without the mediator (which is indicated with a red dashed line in the figure). In between these regimes, $68^\circ < \alpha < 72^\circ$, J_{12} is close to but clearly below the two-dot value. One possible explanation for this behavior is that the superexchange contribution is becoming negative in this range and partially cancels the positive normal exchange energy. Negative superexchange couplings mediated by large quantum dots have recently been observed experimentally [15]. We have also shown in prior work that negative exchange can arise in quantum dots containing as few as four electrons in Chapter 4. However, we believe that it is more likely that the superexchange coupling quickly drops to zero before $\alpha = 68^\circ$, and that the suppression of J_{12} after this point is instead due to the horizontal displacement of the electrons in D1 and D2 caused by Coulomb repulsion as shown in Fig. 5.5. We have checked numerically that displacing dots D1 and D2 by a similar amount in the



(a) Effective exchange energy for triangular triple dot with four electrons.



(b) Zoom-in of panel (a).

Figure 5.6: (a) Effective exchange energy J_{12} versus angle α for four electrons in a triple quantum dot as in Fig. 5.1(c) (case 3). Results are obtained from a CI calculation in which 6, 6 and 3 orbitals are retained for D1, D2 and D3, respectively, for a total of $L = 15$ single-particle basis states. Superexchange processes strongly enhance J_{12} for $\alpha < 65^\circ$. (b) A zoom-in of (a), along with the CI result for two electrons in a double dot (case 1) when $L = 12$ single-particle states are kept (red dashed line). The dip in J_{12} near $\alpha = 70^\circ$ is likely caused by Coulomb repulsion as explained in the text.

two-dot geometry leads to a change in J_{12} that is of the same order of magnitude in that case, supporting this interpretation. This effect could have important consequences in general for architectures in which long-distance interactions are mediated by multielectron quantum dots because, in addition to mediating superexchange interactions, the extra electrons on the mediators can also have a negative impact on the resulting spin-spin coupling strength due to Coulomb interactions depending on the layout of the dots.

Next, we show that the strong enhancement in the superexchange coupling can also be obtained from the Hubbard model introduced in Ref. [74]. We would expect the Hubbard model to be reliable for the dot geometries considered here since we are focusing on long-distance spin-spin couplings between well separated dots. To show that this is true, we first use CI to compute the parameters of the Hubbard model. We focus on the dot configuration with $\alpha = 30^\circ$ since this corresponds to the shortest distances between the dots and thus the regime in which the Hubbard model is most in danger of failing. The Hubbard model parameters we need to compute are the onsite energy associated with filling a dot with one electron (\mathcal{P}) and the additional energy needed to add a second electron (\mathcal{Q}), along with the analogous energies for the mediator (U and Δ , respectively). See Fig. 1 of Ref. [74]. Here, we set $\mathcal{P} = 0$, $\mathcal{Q} = C_1$, $U = V_i$, $\Delta = C_2 + V_i$, where C_1 and C_2 are the sums of the orbital and Coulomb energies for a small dot and the mediator, respectively, V_i is the detuning on the mediator, and the index $i = 0, 2$ indicates the number of electrons on the mediator. From CI calculations, we find that these parameters are $V_0 \approx 20$ meV, $V_2 \approx 1$ meV, $C_1 \approx 11$ meV and $C_2 \approx 8$ meV. Plugging these values into the expressions for the effective exchange couplings from Ref. [74], we find that the ratio of the couplings for 2 or 0 electrons on the mediator is $J_{eff}^2/J_{eff}^0 \approx 200$, which agrees with what we obtain from a direct CI calculation (compare Figs. 5.4 and 5.6(a) at $\alpha = 30^\circ$).

The main difference between these two methods is that full CI includes all the contribu-

tions from the electronic interactions while Hubbard-type models normally neglect the exchange part of the Coulomb interaction and keep onsite direct terms and hopping terms only. Hubbard-type models become unreliable when the exchange terms become significant. For instance, if one wants to describe the ferromagnetic behavior of the intra-dot interactions, one needs to use CI rather than Hubbard-type models since the exchange part of the Coulomb terms is important. In our case, the three dots are not too close to each other, so the exchange terms in the Coulomb interaction are negligible, and the Hubbard model works well.

5.5 Linear triple dot with four electrons

We now move on to the final quantum dot configuration considered in this work: the linear triple dot with four electrons depicted in Fig. 5.1(d). The total quantum dot potential in this case is

$$V_4 = \frac{1}{2}\Theta(x - x_0)m^*\omega_0^2(\mathbf{r} - \mathbf{R}_{D2})^2 + \frac{1}{2}\Theta(-x_0 - x)m^*\omega_0^2(\mathbf{r} - \mathbf{R}_{D1})^2 + \Theta(x + x_0)\Theta(x_0 - x)\left[\frac{1}{2}m^*\omega_1^2(\mathbf{r} - \mathbf{R}_{D3})^2 + \Delta\right]. \quad (5.4)$$

This potential is formed by cutting and gluing together the individual dot potentials along vertical lines located at $x = \pm x_0$. We are interested in computing the effective exchange energy between dots D1 and D2 as a function of the inter-dot distance l_1 . For each l_1 , we set the detuning Δ such that the mediator is occupied by two electrons. The particular values used are given in Appendix A.

To make it easier to compare directly to the triangular triple dot studied in the previous section (case 3), we again compute J_{12} as a function of angle α , but where α now refers to

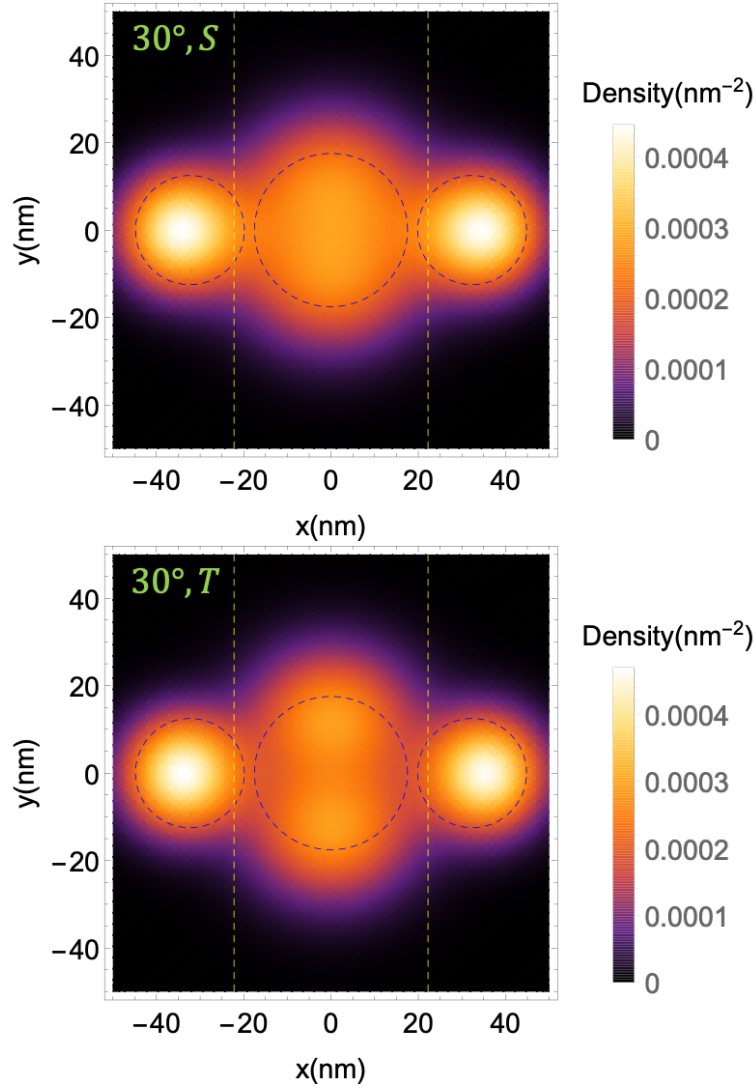
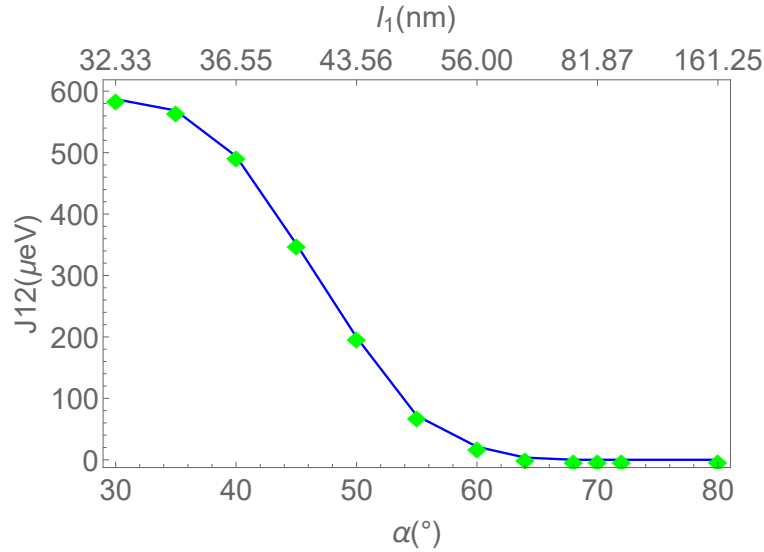
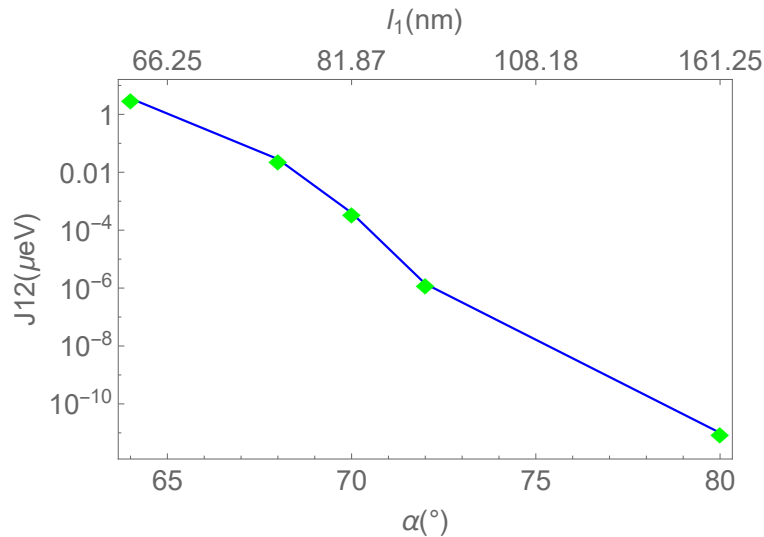


Figure 5.7: Single-particle density for four electrons in a linear triple dot (case 4) with $\alpha = 30^\circ$. The upper (lower) panel shows the single-particle density for the lowest-energy singlet-like $|S\rangle$ (triplet-like $|T_0\rangle$) four-electron state. The yellow dashed lines mark the potential cuts at $x = \pm x_0$. The blue dashed circles indicate the positions of the three dots for this value of α . The electrons in the small dots are displaced slightly outward due to Coulomb repulsion.

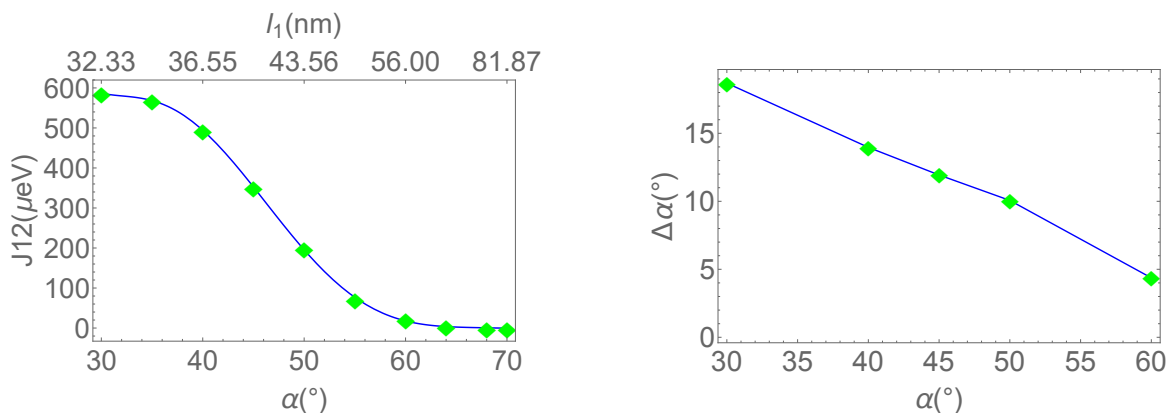


(a) Effective exchange energy for linear triple dot with four electrons.



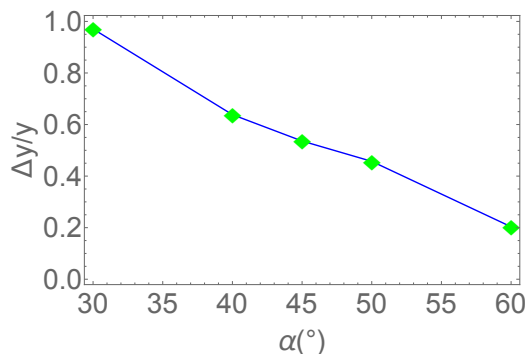
(b) Zoom-in of panel (a).

Figure 5.8: (a) Effective exchange energy J_{12} versus inter-dot separation (given by $2l_1 = 2l_0 \sec \alpha$, with $l_0 = 28$ nm) for four electrons in a linear triple dot as in Fig. 5.1(d) (case 4). Results are obtained from a CI calculation in which 6, 6 and 3 orbitals are retained for dots D1, D2 and D3, respectively, for a total of $L = 15$ single-particle basis states. The presence of the two mediator electrons strongly enhances J_{12} for $\alpha < 65^\circ$. (b) A zoom-in of (a). In the large-distance regime (large α and l_1), J_{12} monotonically approaches zero.



(a) Interpolating function for effective exchange in case 4.

(b) Effective angular shifts for case 3.



(c) Relative electron position shifts for case 3.

Figure 5.9: Calculation of the vertical shift in electron positions due to Coulomb repulsion in case 3 (triangular triple dot) using the exchange energy from case 4 (linear triple dot). We assume the electrons in D1 and D2 remain fixed and only consider the movement of electrons in D3. (a) Effective exchange energy versus α and l_1 for case 4. Green diamonds are the original data from Fig. 5.8. The blue line is an interpolating function for lower angles to intermediate angles. One can map the data of case 3 to this function to get information about the shifts in electron positions as explained in the main text. (b) The resulting angular shifts due to Coulomb repulsion for different angles α . (c) The relative change in vertical position of the electrons in D3 for different angles.

the corresponding angle in the triangular triple dot geometry that has the same distance l_1 between the mediator D3 and the smaller dots D1 and D2. Imagine that each linear geometry we consider in this section is obtained by starting from a triangular configuration with angle α , freezing l_1 , and then rotating D1 and D2 around D3 until all three dot centers lie on a line. In this way, each value of α that we start with corresponds to a different inter-dot distance in the linear geometry according to the formula $l_1 = l_0 \sec \alpha$, where $l_0 = 28$ nm. We are thus computing $J_{12}(l_1) = J_{12}(l_0 \sec \alpha)$ as a function of α .

An example of the one-electron density for $\alpha = 30^\circ$ is shown in Fig. 5.7. Although the inter-dot distance is rather short at this value of α ($l_1 = 32.33$ nm), the electrons in D1 and D2 shift only slightly away from D3. This is because of a trade-off between the Coulomb repulsion and the large confinement energy of the small dots. The electrons in the small dots need to move only a little bit to cancel the Coulomb repulsion from the mediator electrons. The horizontal shift of the D1, D2 electrons is smaller than in case 3 (see Fig. 5.5) because D1 and D2 are a bit further apart here. It is also evident in Fig. 5.7 that the density for the triplet state is more disjointed (exhibiting four distinct maxima) compared to the singlet density as one would expect based on fermion statistics. Additional single-electron density plots for other values of α can be found in Appendix A.

Our CI results for J_{12} as a function of α in the linear geometry are shown in Fig. 5.8. The first thing to notice is that the superexchange again dominates in the small α regime, even more so here than in the triangular triple dot (case 3), as is evident in Fig. 5.8(a). We also see from Fig. 5.8(b) that the interaction strength remains above $1 \mu\text{eV}$ for inter-dot distances of up to ~ 130 nm. This should be compared to the case without the mediator (Fig. 5.2(b)), where the corresponding distance is only 56 nm. Thus, the mediator extends the interaction range by more than a factor of 2. Fig. 5.8(b) further reveals that the effective exchange decays to zero monotonically with inter-dot distance. Because the horizontal displacement

caused by Coulomb repulsion is smaller in this case, a dip in J_{12} does not arise as in case 3. The large enhancement in J_{12} at smaller α relative to that seen in case 3 is likely due to the fact that the vertical Coulomb repulsion in case 3 effectively increases the distance to the mediator electrons (see Fig. 5.5), which in turn reduces the benefit to the superexchange that comes from the presence of these extra electrons. The vertical shift is significant because of the weak confinement energy of the mediator. On the other hand, the additional symmetry in the linear geometry prevents a similar phenomenon from happening in this case, yielding a stronger superexchange enhancement. If this interpretation is correct, then we should adjust the α values in case 3 to account for the upward shift of the mediator electrons in order to do a proper comparison to the linear configuration. To check whether this makes sense, we will in fact do the opposite: We first determine the shift in α^{case3} needed to make J_{12}^{case3} equal to J_{12}^{case4} (setting the inter-dot distances equal in both cases), and we will then check whether this shift corresponds to a vertical displacement Δy of the mediator electrons that is comparable to that seen in Fig. 5.5. The first step then is to solve the equation

$$J_{12}^{case3}(\alpha^{case3}) = J_{12}^{case4}(\alpha^{case4}), \quad (5.5)$$

for α^{case4} , which we then interpret as the effective angle for case 3: $\alpha_{eff}^{case3} = \alpha^{case4}$. The shift in α caused by Coulomb repulsion is then $\Delta\alpha = \alpha_{eff}^{case3} - \alpha^{case3}$. In order to solve Eq. (5.5), we must first interpolate our data for J_{12} versus α to obtain a smooth function $J_{12}^{case4}(\alpha^{case4})$. This interpolation is shown in Fig. 5.9(a), and the $\Delta\alpha$ that results from solving Eq. (5.5) is shown in Fig. 5.9(b). The corresponding vertical displacement is then given by

$$\frac{\Delta y}{y} = \frac{y_{eff} - y}{y} = \frac{l_0 \tan(\alpha_{eff}^{case3}) - l_0 \tan(\alpha^{case3})}{l_0 \tan(\alpha^{case3})} = \frac{\tan(\alpha_{eff}^{case3}) - \tan(\alpha^{case3})}{\tan(\alpha^{case3})}. \quad (5.6)$$

These results are shown in Fig. 5.9(c), where it is clear that substantial vertical shifts are

needed to account for the suppression of J_{12} in the triangular triple dot case. For example, when $\alpha = 30^\circ$, $\Delta y/y \approx 0.95$, corresponding to a $\sim 95\%$ vertical shift. From Fig. 5.5, where $y = l_0 \tan \alpha = 16.17$ nm, we see that $y_{eff} \approx 25$ nm, yielding $\Delta y/y \approx 0.55$. Although this is less than 0.95, it is still large enough that we believe this is the primary mechanism responsible for the suppression of J_{12} in the triangular case. The discrepancy is likely due to the downward shift of the electrons in D1 and D2, which we have neglected in this analysis. From Fig. 5.5, we see that this shift is on the order of 5 nm; this would bring the net vertical shift up to $y_{eff} \approx 30$ nm, which is consistent with the 95% value obtained from our analysis. As the angle or l_1 gets larger, the Coulomb repulsion becomes weaker, and the vertical displacement becomes negligible, which is also clear from Fig. 5.9(c). One can also see this from the shifts in the single-particle densities at larger α shown in Appendix A.

Before we conclude, it is worth commenting on why we have not seen any evidence of negative exchange interactions, even though our previous work in Chapter 4 showed that these can arise in quantum dot systems containing as few as four electrons. There, we showed that if four electrons are confined in a symmetric parabolic potential, the ground state is a triplet provided the splitting between the second and third single-particle levels is sufficiently small. This splitting vanishes in the limit of zero magnetic field due to rotational symmetry, and it remains small in the low magnetic field regime. These findings suggest that, in the present case of the linear triple dot, if one were to gradually tune l_1 down to zero, one would see the exchange energy reach a maximum positive value and then decrease all the way down to negative values as the three dots merge into one big dot. Before l_1 reaches zero, the triple dot potential looks like one large elliptical dot. In Chapter 4, we calculated how the exchange energy depends on dot ellipticity, and we showed that a transition from negative to positive exchange occurs as the ellipticity increases past a certain threshold value that depends on the confinement energy. This transition happens because increasing the ellipticity breaks the

rotational symmetry of the dot and opens a gap between the second and third single-particle levels. Fig. 4.3 of Chapter 4 shows that the exchange energy vanishes when the ellipticity $\hbar\delta\omega$ is about 1-2 meV (when the confinement energy is 7-8 meV), which corresponds to a difference of 2-4 nm between the vertical and horizontal extent of the dot potential. For the linear triple-dot geometry, this implies that the small dots would need to overlap almost completely with the mediator, which happens for $l_1 \lesssim 5$ nm, which is well below the l_1 values we have considered. Thus, it is not surprising that we have not encountered negative exchange energies in this work. Unfortunately, probing this crossover behavior from three separate dots to one large dot is computationally challenging because a very large number of single-particle basis states would be needed to obtain accurate results, which translates to a very large computational cost. It would also be interesting to explore the possibility of negative superexchange interactions when four electrons are confined to the mediator instead of two. We leave these investigations to future work.

5.6 Conclusions

In this chapter, we explored the interplay of normal exchange and superexchange processes in triple quantum dot systems where a large dot is used to mediate long-range spin-spin interactions between a pair of smaller dots. We consider triangular geometries in which both normal exchange and superexchange can be present simultaneously. Using configuration interaction simulations, we showed that the effective exchange energy receives a modest enhancement due to superexchange when the mediating dot is brought sufficiently close to the small dots. We further showed that this enhancement can be increased by two orders of magnitude if the mediating dot is loaded with two electrons, a phenomenon we attribute to a combination of Fermi statistics and quantum confinement. We also found that the effective

exchange energy exhibits non-monotonic behavior as the distance between the small dots and the mediator is varied. This can be understood as a consequence of the rapid decay of superexchange with distance and a more slowly changing lateral shift of the electron positions in the small dots due to Coulomb repulsion from the mediator electrons. Our calculations also reveal that the effective exchange interaction can be made still larger by placing the mediating dot exactly between the two smaller dots, and we provided evidence that the somewhat smaller interaction in the triangular case is likely due to an additional Coulomb repulsion that is not present in the linear case. Moreover, we found that in addition to sharply increasing the effective exchange coupling, the electron-filled mediator also more than doubles the range of the interaction.

Overall, we found that the strength of the superexchange interaction depends on both the detuning of the mediator and on the geometry of the three dots. Low detunings on the mediator can lead to very high superexchange couplings. This is the main reason the superexchange is much larger when two electrons are confined on the mediator compared to no electrons. We also saw that geometry plays an important role as well, albeit to a lesser extent. In the triangular dot configurations, the superexchange coupling is lower than in the linear case because of a shift in the electron density on the mediator, which in turn changes the effective distance between the small dots and the mediator. Both factors should be taken into consideration when designing multi-dot devices that utilize superexchange interactions.

Our results show that including electrons in a quantum dot mediator can substantially enhance the strength and range of spin-spin interactions between remote quantum dots. They also suggest that the precise geometry of the dots can have important ramifications and provide additional flexibility in the design of larger-scale architectures based on quantum dot-mediated exchange couplings.

Chapter 6

Summary and outlook

The goal of this thesis is to improve our understanding of the exchange and superexchange processes that take place in semiconductor quantum dot spin systems.

In the opening chapters, we described the basic concepts and key features of quantum dot systems. Quantum dots can be treated as artificial two-dimensional atoms. The number of electrons can be controlled by the gates connected to the quantum dots. We also described important applications of quantum dot systems. On the one hand, they can be used as quantum computation devices to realize different kinds of spin qubit systems. On the other hand, they can also be used for quantum simulation. In this thesis, we paid particular attention to the role of exchange interactions in spin qubits. We discussed the measurement of exchange energy in experiments in a two-dot system.

After introducing the basics of quantum dots, one should consider how to describe them in theory. We built the single particle states referred as Fock-Darwin states. For systems with more than one quantum dot, we implemented the Cholesky decomposition to obtain the truly orthonormal basis. Using this basis, we built the many particle states. To calculate the total many particle Hamiltonian, we then applied the Slater-Condon rules to relate the many particle matrix elements to single and double particle ones, which simplified the problem a lot. After introducing the computational approaches we use, including configuration interaction and Hubbard models, we derived different physical phenomena that can arise in quantum dot systems. From a generic Hamiltonian, we found the exchange terms of the

Coulomb coupling can lead to the effective spin-spin interaction referred to ferromagnetism, which is shown in Eq. (3.39). This mechanism is called Hund’s rule in atomic physics. Thus it can arise in quantum dot systems if there are enough electrons occupying in one dot. On the other hand, if the exchange terms of the Coulomb coupling are small enough, which is the case for interdot interactions, we can simplify our model to the Hubbard model shown as in Eq. (3.41). Thus in this model, only two parameters are needed, which are the hopping terms and the on-site Coulomb energy. Taking the leading order, one can arrive at the Heisenberg model, which is a commonly used model for quantum dot systems. The Heisenberg model leads to anti-ferromagnetism, and the exchange coupling indicates the energy difference between triplet $|T_0\rangle$ and $|S_0\rangle$, which is the energy we focus on. From this mechanism, this energy $J = \frac{t^2}{U}$ is always positive. Furthermore, we have reviewed an experiment implemented by our collaborators in Prof. John Nichol’s group, where we contributed to the theoretical modeling and pointed out that the positions of quantum dots were actually shifting in response to changes in barrier heights. In this work, we showed how to simultaneously control multiple exchange couplings in a Heisenberg chain of four quantum dots. We showed that our two theoretical models (Heitler-London model and exponential model) can both describe the inter-dependence of the barrier heights and dot positions faithfully. The techniques and models in this work can be further used to realize the advanced control necessary to produce interesting phenomena such as a time crystal phase.

In Chapter 4, we have mainly focused on negative exchange interactions observed in an experiment implemented by the Copenhagen group led by Prof. Ferdinand Kuemmeth. For the system with two small and one large quantum dot, they found that negative exchange can arise between the large quantum dot and the small one in the middle. To describe this system, we constructed a Hubbard model including the Hund’s rule terms. By using the “frozen-core” approximation, we recovered the negative exchange interaction, shown in

Fig. 4.4(b), found by their experiment. This indicates that the negative exchange is caused by the inter-orbital exchange in the large quantum dot rather than anything related to the small dot. Thus, we explored one single large quantum dot filled with several electrons using a configuration interaction approach. The question is how many electrons one needs to generate negative exchange in the large dot. We then found the answer that four electrons are enough. Lastly, we broke the degeneracy of the shells in the dot by making the dot potential asymmetric. We found that for a four-electron system a transition from a triplet to a singlet ground state happens as the energy gap grows. This is true for both GaAs and Si quantum dots.

In the last part of this thesis, we considered more complicated quantum dot systems, such as a 2d quantum dot array. This requires one to first understand the simple blocks of these 2d systems. In this work, we considered three quantum dot systems with different geometries. Firstly, we considered two dots with two electrons (case 1) to find the minimum number of single-particle orbitals needed to accurately describe one dot and to find the basic exchange energy for this system. Then we introduced a third dot which is significantly larger (case 2). These three dots forms a triangle, and we explored the effective exchange energy for these two electrons under the influence of the large dot. We found that the effective exchange energy J does not change much in this case. Then we put another two electrons in the large quantum dot (case 3) to have the exact geometry as case 2. In this case, we see three distinct regions of behavior: For the low angle region, superexchange is enhanced substantially up to about 250 times compared to case 2. For a range of intermediate angles, the superexchange energy is on the order of the normal exchange, and there is a small region where the contribution of superexchange is negative, which leads the total effective exchange energy to be lower than the original one. In the last case, we put three dots on a line and varied their separation. We found that the superexchange is enhanced even further (about 600 times the normal

exchange) than case 3. The reason behind this is that for a triangular geometry, electrons in the large dot will be pushed from the center to the side due to Coulomb interaction and this leads the effective distance to be larger than before whereas the linear system does not have this effect. These high superexchange cases open the possibility of using large quantum dots to mediate long distance interactions between remote spin qubits. These results are useful for constructing quantum dot arrays and enabling more versatile architectures for quantum dot systems.

In the future, one could consider a quantum computation or simulation device based on 2d quantum dot arrays. According to the understanding provided by our work, one could implement both positive or negative exchange energy to control the spin qubits, which would reduce the control time and add greater flexibility in canceling noise dynamically. One could also imagine including large quantum dots in the array to enhance or suppress long-distance interactions between distant spins by adjusting the detuning or electron number in the large dots. This provides more flexibility for controlling these types systems.

Bibliography

- [1] Ronald Hanson, Leo P Kouwenhoven, Jason R Petta, Seigo Tarucha, and Lieven MK Vandersypen. Spins in few-electron quantum dots. *Reviews of modern physics*, 79(4):1217, 2007.
- [2] Frederico Martins, Filip K Malinowski, Peter D Nissen, Saeed Fallahi, Geoffrey C Gardner, Michael J Manfra, Charles M Marcus, and Ferdinand Kuemmeth. Negative spin exchange in a multielectron quantum dot. *Physical review letters*, 119(22):227701, 2017.
- [3] Daniel Loss and David P DiVincenzo. Quantum computation with quantum dots. *Physical Review A*, 57(1):120, 1998.
- [4] M Wagner, U Merkt, and A. V. Chaplik. Spin-singlet–spin-triplet oscillations in quantum dots. *Physical Review B*, 45(4):1951–1954, jan 1992.
- [5] Fabio Baruffa, Peter Stano, and Jaroslav Fabian. Spin-orbit coupling and anisotropic exchange in two-electron double quantum dots. *Physical Review B*, 82(4):045311, jul 2010.
- [6] D. M. Zumbühl, C. M. Marcus, M. P. Hanson, and A. C. Gossard. Cotunneling Spectroscopy in Few-Electron Quantum Dots. *Physical Review Letters*, 93(25):256801, dec 2004.
- [7] Sebastian Mehl and David P. DiVincenzo. Inverted singlet-triplet qubit coded on a two-electron double quantum dot. *Physical Review B*, 90(19):195424, nov 2014.

- [8] Zack White and Guy Ramon. Extended orbital modeling of spin qubits in double quantum dots. *Physical Review B*, 97(4):045306, 2018.
- [9] Elliott Lieb and Daniel Mattis. Theory of Ferromagnetism and the Ordering of Electronic Energy Levels. *Physical Review*, 125(1):164–172, jan 1962.
- [10] Richard P. Feynman. *Statistical mechanics: A set of lectures*. Westview Press, 1998.
- [11] Xin Wang, Lev S. Bishop, J.P. Kestner, Edwin Barnes, Kai Sun, and S Das Sarma. Composite pulses for robust universal control of singlet–triplet qubits. *Nature Communications*, 3:997, aug 2012.
- [12] Jason P. Kestner, Xin Wang, Lev S. Bishop, Edwin Barnes, and S. Das Sarma. Noise-Resistant Control for a Spin Qubit Array. *Physical Review Letters*, 110(14):140502, apr 2013.
- [13] Xin Wang, Lev S. Bishop, Edwin Barnes, J. P. Kestner, and S. Das Sarma. Robust quantum gates for singlet-triplet spin qubits using composite pulses. *Physical Review A*, 89(2):022310, feb 2014.
- [14] Filip K Malinowski, Frederico Martins, Thomas B Smith, Stephen D Bartlett, Andrew C Doherty, Peter D Nissen, Saeed Fallahi, Geoffrey C Gardner, Michael J Manfra, Charles M Marcus, et al. Spin of a multielectron quantum dot and its interaction with a neighboring electron. *Physical Review X*, 8(1):011045, 2018.
- [15] Filip K Malinowski, Frederico Martins, Thomas B Smith, Stephen D Bartlett, Andrew C Doherty, Peter D Nissen, Saeed Fallahi, Geoffrey C Gardner, Michael J Manfra, Charles M Marcus, et al. Fast spin exchange across a multielectron mediator. *Nature communications*, 10(1):1–6, 2019.

- [16] Peter W Shor. Algorithms for quantum computation: discrete logarithms and factoring. In *Proceedings 35th annual symposium on foundations of computer science*, pages 124–134. Ieee, 1994.
- [17] David P DiVincenzo. The physical implementation of quantum computation. *Fortschritte der Physik: Progress of Physics*, 48(9-11):771–783, 2000.
- [18] Charles H Bennett and David P DiVincenzo. Quantum information and computation. *nature*, 404(6775):247–255, 2000.
- [19] Efstratios Manousakis. A quantum-dot array as model for copper-oxide superconductors: A dedicated quantum simulator for the many-fermion problem. *Journal of low temperature physics*, 126(5-6):1501–1513, 2002.
- [20] Tim Byrnes, Na Young Kim, Kenichiro Kusudo, and Yoshihisa Yamamoto. Quantum simulation of fermi-hubbard models in semiconductor quantum-dot arrays. *Physical Review B*, 78(7):075320, 2008.
- [21] Pierre Barthelemy and Lieven MK Vandersypen. Quantum dot systems: a versatile platform for quantum simulations. *Annalen der Physik*, 525(10-11):808–826, 2013.
- [22] Toivo Hensgens, Takafumi Fujita, Laurens Janssen, Xiao Li, CJ Van Diepen, Christian Reichl, Werner Wegscheider, S Das Sarma, and Lieven MK Vandersypen. Quantum simulation of a fermi–hubbard model using a semiconductor quantum dot array. *Nature*, 548(7665):70–73, 2017.
- [23] Juan P Dehollain, Uditendu Mukhopadhyay, Vincent P Michal, Yao Wang, Bernhard Wunsch, Christian Reichl, Werner Wegscheider, Mark S Rudner, Eugene Demler, and Lieven MK Vandersypen. Nagaoka ferromagnetism observed in a quantum dot plaquette. *Nature*, 579(7800):528–533, 2020.

- [24] Yosuke Nagaoka. Ferromagnetism in a narrow, almost half-filled s band. *Physical Review*, 147(1):392, 1966.
- [25] Floris A Zwanenburg, Andrew S Dzurak, Andrea Morello, Michelle Y Simmons, Lloyd CL Hollenberg, Gerhard Klimeck, Sven Rogge, Susan N Coppersmith, and Mark A Eriksson. Silicon quantum electronics. *Reviews of modern physics*, 85(3):961, 2013.
- [26] Hendrik Bluhm, Sandra Foletti, Izhar Neder, Mark Rudner, Diana Mahalu, Vladimir Umansky, and Amir Yacoby. Dephasing time of gaas electron-spin qubits coupled to a nuclear bath exceeding 200 μ s. *Nature Physics*, 7(2):109–113, 2011.
- [27] Brett M Maune, Matthew G Borselli, Biqin Huang, Thaddeus D Ladd, Peter W Deelman, Kevin S Holabird, Andrey A Kiselev, Ivan Alvarado-Rodriguez, Richard S Ross, Adele E Schmitz, et al. Coherent singlet-triplet oscillations in a silicon-based double quantum dot. *Nature*, 481(7381):344–347, 2012.
- [28] M Veldhorst, JCC Hwang, CH Yang, AW Leenstra, Bob de Ronde, JP Dehollain, JT Muhonen, FE Hudson, Kohei M Itoh, A Morello, et al. An addressable quantum dot qubit with fault-tolerant control-fidelity. *Nature nanotechnology*, 9(12):981–985, 2014.
- [29] Filip K Malinowski, Frederico Martins, Peter D Nissen, Edwin Barnes, Łukasz Cywiński, Mark S Rudner, Saeed Fallahi, Geoffrey C Gardner, Michael J Manfra, Charles M Marcus, et al. Notch filtering the nuclear environment of a spin qubit. *Nature nanotechnology*, 12(1):16, 2017.
- [30] Jason R Petta, Alexander Comstock Johnson, Jacob M Taylor, Edward A Laird, Amir Yacoby, Mikhail D Lukin, Charles M Marcus, Micah P Hanson, and Arthur C Gos-

- sard. Coherent manipulation of coupled electron spins in semiconductor quantum dots. *Science*, 309(5744):2180–2184, 2005.
- [31] Sandra Foletti, Hendrik Bluhm, Diana Mahalu, Vladimir Umansky, and Amir Yacoby. Universal quantum control of two-electron spin quantum bits using dynamic nuclear polarization. *Nature Physics*, 5(12):903–908, 2009.
- [32] J Medford, Johannes Beil, JM Taylor, SD Bartlett, AC Doherty, EI Rashba, DP DiVincenzo, H Lu, AC Gossard, and Charles M Marcus. Self-consistent measurement and state tomography of an exchange-only spin qubit. *Nature nanotechnology*, 8(9):654–659, 2013.
- [33] JM Elzerman, R Hanson, LH Willems Van Beveren, B Witkamp, LMK Vandersypen, and Leo P Kouwenhoven. Single-shot read-out of an individual electron spin in a quantum dot. *nature*, 430(6998):431–435, 2004.
- [34] Frank HL Koppens, Christo Buizert, Klaas-Jan Tielrooij, Ivo T Vink, Katja C Nowack, Tristan Meunier, LP Kouwenhoven, and LMK Vandersypen. Driven coherent oscillations of a single electron spin in a quantum dot. *Nature*, 442(7104):766–771, 2006.
- [35] Edward A Laird, Jacob Mason Taylor, David P DiVincenzo, Charles Masamed Marcus, Micah P Hanson, and Arthur C Gossard. Coherent spin manipulation in an exchange-only qubit. *Physical Review B*, 82(7):075403, 2010.
- [36] J Medford, Johannes Beil, JM Taylor, EI Rashba, H Lu, AC Gossard, and Charles M Marcus. Quantum-dot-based resonant exchange qubit. *Physical review letters*, 111(5):050501, 2013.
- [37] Kevin Eng, Thaddeus D Ladd, Aaron Smith, Matthew G Borselli, Andrey A Kisilev, Bryan H Fong, Kevin S Holabird, Thomas M Hazard, Biqin Huang, Peter W

- Deelman, et al. Isotopically enhanced triple-quantum-dot qubit. *Science Advances*, 1(4):e1500214, 2015.
- [38] Zhan Shi, CB Simmons, JR Prance, John King Gamble, Teck Seng Koh, Yun-Pil Shim, Xuedong Hu, DE Savage, MG Lagally, MA Eriksson, et al. Fast hybrid silicon double-quantum-dot qubit. *Physical review letters*, 108(14):140503, 2012.
- [39] Teck Seng Koh, John King Gamble, Mark Friesen, MA Eriksson, and SN Coppersmith. Pulse-gated quantum-dot hybrid qubit. *Physical review letters*, 109(25):250503, 2012.
- [40] Gang Cao, Hai-Ou Li, Guo-Dong Yu, Bao-Chuan Wang, Bao-Bao Chen, Xiang-Xiang Song, Ming Xiao, Guang-Can Guo, Hong-Wen Jiang, Xuedong Hu, et al. Tunable hybrid qubit in a gas double quantum dot. *Physical review letters*, 116(8):086801, 2016.
- [41] Maximilian Russ and Guido Burkard. Three-electron spin qubits. *Journal of Physics: Condensed Matter*, 29(39):393001, 2017.
- [42] Xin Wang, Shuo Yang, and S Das Sarma. Quantum theory of the charge-stability diagram of semiconductor double-quantum-dot systems. *Physical Review B*, 84(11):115301, 2011.
- [43] Edwin Barnes, JP Kestner, NTT Nguyen, and S Das Sarma. Screening of charged impurities with multielectron singlet-triplet spin qubits in quantum dots. *Physical Review B*, 84(23):235309, 2011.
- [44] Haifeng Qiao, Yadav P Kandel, Kuangyin Deng, Saeed Fallahi, Geoffrey C Gardner, Michael J Manfra, Edwin Barnes, and John M Nichol. Coherent multispin exchange coupling in a quantum-dot spin chain. *Physical Review X*, 10(3):031006, 2020.

- [45] Rogerio de Sousa, Xuedong Hu, and S Das Sarma. Effect of an inhomogeneous external magnetic field on a quantum-dot quantum computer. *Physical Review A*, 64(4):042307, 2001.
- [46] Haifeng Qiao, Yadav P Kandel, John S Van Dyke, Saeed Fallahi, Geoffrey C Gardner, Michael J Manfra, Edwin Barnes, and John M Nichol. Floquet-enhanced spin swaps. *arXiv preprint arXiv:2006.10913*, 2020.
- [47] John S Van Dyke, Yadav P Kandel, Haifeng Qiao, John M Nichol, Sophia E Economou, and Edwin Barnes. Protecting quantum information in quantum dot spin chains by driving exchange interactions periodically. *arXiv preprint arXiv:2009.08469*, 2020.
- [48] Bikun Li, John S Van Dyke, Ada Warren, Sophia E Economou, and Edwin Barnes. Discrete time crystal in the gradient-field heisenberg model. *Physical Review B*, 101(11):115303, 2020.
- [49] Kuangyin Deng, FA Calderon-Vargas, Nicholas J Mayhall, and Edwin Barnes. Negative exchange interactions in coupled few-electron quantum dots. *Physical Review B*, 97(24):245301, 2018.
- [50] Hendrik Bluhm, Sandra Foletti, Izhar Neder, Mark Rudner, Diana Mahalu, Vladimir Umansky, and Amir Yacoby. Dephasing time of GaAs electron-spin qubits coupled to a nuclear bath exceeding 200 μ s. *Nature Physics*, 7(2):109–113, feb 2011.
- [51] Filip K. Malinowski, Frederico Martins, Peter D. Nissen, Edwin Barnes, Łukasz Cywiński, Mark S. Rudner, Saeed Fallahi, Geoffrey C. Gardner, Michael J. Manfra, Charles M. Marcus, and Ferdinand Kuemmeth. Notch filtering the nuclear environment of a spin qubit. *Nature Nanotechnology*, 12(1):16–20, oct 2016.
- [52] K. Takeda, J. Kamioka, T. Otsuka, J. Yoneda, T. Nakajima, M. R. Delbecq, S. Amaha,

- G. Allison, T. Kodera, S. Oda, and S. Tarucha. A fault-tolerant addressable spin qubit in a natural silicon quantum dot. *Science Advances*, 2(8):e1600694–e1600694, aug 2016.
- [53] Erika Kawakami, Thibaut Jullien, Pasquale Scarlino, Daniel R. Ward, Donald E. Savage, Max G. Lagally, Viatcheslav V. Dobrovitski, Mark Friesen, Susan N. Coppersmith, Mark A. Eriksson, and Lieven M. K. Vandersypen. Gate fidelity and coherence of an electron spin in an Si/SiGe quantum dot with micromagnet. *Proceedings of the National Academy of Sciences*, 113(42):11738–11743, oct 2016.
- [54] KC Nowack, M Shafiei, M Laforest, GEDK Prawiroatmodjo, LR Schreiber, C Reichl, W Wegscheider, and LMK Vandersypen. Single-shot correlations and two-qubit gate of solid-state spins. *Science*, 333(6047):1269–1272, 2011.
- [55] M Veldhorst, C H Yang, J C C Hwang, W Huang, J P Dehollain, J T Muhonen, S Simmons, A Laucht, F E Hudson, K M Itoh, A Morello, and A S Dzurak. A two-qubit logic gate in silicon. *Nature*, 526(7573):410–414, oct 2015.
- [56] D. M. Zajac, A. J. Sigillito, M. Russ, F. Borjans, J. M. Taylor, G. Burkard, and J. R. Petta. Quantum CNOT Gate for Spins in Silicon. aug 2017.
- [57] Pascal Cerfontaine, Tim Botzem, David P. DiVincenzo, and Hendrik Bluhm. High-Fidelity Single-Qubit Gates for Two-Electron Spin Qubits in GaAs. *Physical Review Letters*, 113(15):150501, oct 2014.
- [58] Xian Wu, D R Ward, J R Prance, Dohun Kim, John King Gamble, R T Mohr, Zhan Shi, D E Savage, M G Lagally, Mark Friesen, S N Coppersmith, and M A Eriksson. Two-axis control of a singlet-triplet qubit with an integrated micromagnet. *Proceedings of the National Academy of Sciences*, 111(33):11938–11942, aug 2014.
- [59] M. D. Shulman, O. E. Dial, S. P. Harvey, H. Bluhm, V. Umansky, and A. Yacoby.

- Demonstration of Entanglement of Electrostatically Coupled Singlet-Triplet Qubits. *Science*, 336(6078):202–205, apr 2012.
- [60] John M. Nichol, Lucas A. Orona, Shannon P. Harvey, Saeed Fallahi, Geoffrey C. Gardner, Michael J. Manfra, and Amir Yacoby. High-fidelity entangling gate for double-quantum-dot spin qubits. *npj Quantum Information*, 3(1):3, dec 2017.
- [61] Dohun Kim, Zhan Shi, CB Simmons, DR Ward, JR Prance, Teck Seng Koh, John King Gamble, DE Savage, MG Lagally, Mark Friesen, et al. Quantum control and process tomography of a semiconductor quantum dot hybrid qubit. *Nature*, 511(7507):70–74, 2014.
- [62] Dohun Kim, Daniel R. Ward, Christie B. Simmons, Don E. Savage, Max G. Lagally, Mark Friesen, Susan N. Coppersmith, and Mark A. Eriksson. High-fidelity resonant gating of a silicon-based quantum dot hybrid qubit. *npj Quantum Information*, 1(1):15004, dec 2015.
- [63] R. Brunner, Y.-S. Shin, T. Obata, M. Pioro-Ladrière, T. Kubo, K. Yoshida, T. Taniyama, Y. Tokura, and S. Tarucha. Two-Qubit Gate of Combined Single-Spin Rotation and Interdot Spin Exchange in a Double Quantum Dot. *Physical Review Letters*, 107(14):146801, sep 2011.
- [64] Xuedong Hu and S. Das Sarma. Charge-Fluctuation-Induced Dephasing of Exchange-Coupled Spin Qubits. *Physical Review Letters*, 96(10):100501, mar 2006.
- [65] M. D. Reed, B. M. Maune, R. W. Andrews, M. G. Borselli, K. Eng, M. P. Jura, A. A. Kiselev, T. D. Ladd, S. T. Merkel, I. Milosavljevic, E. J. Pritchett, M. T. Rakher, R. S. Ross, A. E. Schmitz, A. Smith, J. A. Wright, M. F. Gyure, and A. T. Hunter. Reduced Sensitivity to Charge Noise in Semiconductor Spin Qubits via Symmetric Operation. *Physical Review Letters*, 116(11):110402, mar 2016.

- [66] Frederico Martins, Filip K. Malinowski, Peter D. Nissen, Edwin Barnes, Saeed Fallahi, Geoffrey C. Gardner, Michael J. Manfra, Charles M. Marcus, and Ferdinand Kuemmeth. Noise Suppression Using Symmetric Exchange Gates in Spin Qubits. *Physical Review Letters*, 116(11):116801, mar 2016.
- [67] Edwin Barnes, Mark S. Rudner, Frederico Martins, Filip K. Malinowski, Charles M. Marcus, and Ferdinand Kuemmeth. Filter function formalism beyond pure dephasing and non-Markovian noise in singlet-triplet qubits. *Physical Review B*, 93(12):121407, mar 2016.
- [68] Chengxian Zhang, Robert E. Throckmorton, Xu-Chen Yang, Xin Wang, Edwin Barnes, and S. Das Sarma. Randomized Benchmarking of Barrier versus Tilt Control of a Singlet-Triplet Qubit. *Physical Review Letters*, 118(21):216802, may 2017.
- [69] Xu-Chen Yang and Xin Wang. Suppression of charge noise using barrier control of a singlet-triplet qubit. *Physical Review A*, 96(1):012318, jul 2017.
- [70] Xu-chen Yang and Xin Wang. The magic angle for barrier-controlled double quantum dots. 1:1–8, jul 2017.
- [71] Yun-Pil Shim and Charles Tahan. Theory of barrier vs tilt exchange gate operations in spin-based quantum computing. pages 1–9, nov 2017.
- [72] Guido Burkard, Daniel Loss, and David P. DiVincenzo. Coupled quantum dots as quantum gates. *Physical Review B*, 59(3):2070–2078, jan 1999.
- [73] Qiuzi Li, Łukasz Cywiński, Dimitrie Culcer, Xuedong Hu, and S. Das Sarma. Exchange coupling in silicon quantum dots: Theoretical considerations for quantum computation. *Physical Review B*, 81(8):085313, feb 2010.

- [74] Sebastian Mehl, Hendrik Bluhm, and David P. DiVincenzo. Two-qubit couplings of singlet-triplet qubits mediated by one quantum state. *Phys. Rev. B*, 90:045404, Jul 2014.
- [75] Timothy Alexander Baart, Takafumi Fujita, Christian Reichl, Werner Wegscheider, and Lieven Mark Koenraad Vandersypen. Coherent spin-exchange via a quantum mediator. *Nature Nanotechnology*, 12(1):26–30, oct 2016.
- [76] X. Mi, M. Benito, S. Putz, D. M. Zajac, J. M. Taylor, Guido Burkard, and J. R. Petta. A Coherent Spin-Photon Interface in Silicon. pages 1–19, oct 2017.
- [77] V. Srinivasa, H. Xu, and J. M. Taylor. Tunable spin-qubit coupling mediated by a multielectron quantum dot. *Phys. Rev. Lett.*, 114:226803, Jun 2015.
- [78] X. G. Croot, S. J. Pauka, J. D. Watson, G. C. Gardner, S. Fallahi, M. J. Manfra, and D. J. Reilly. Device Architecture for Coupling Spin Qubits Via an Intermediate Quantum State. *arXiv preprint*, pages 1–6, jul 2017.
- [79] Filip Kazimierz Malinowski. Noise suppression and long-range exchange coupling for gallium arsenide spin qubits, 2017.
- [80] Filip K. Malinowski, Frederico Martins, Thomas B. Smith, Stephen D. Bartlett, Andrew C. Doherty, Peter D. Nissen, Saeed Fallahi, Geoffrey C. Gardner, Michael J. Manfra, Charles M. Marcus, and Ferdinand Kuemmeth. Spin of a multielectron quantum dot and its interaction with a neighboring electron. *arXiv preprint*, pages 1–20, oct 2017.
- [81] G. Goelman, S. Vega, and D.B Zax. Squared amplitude-modulated composite pulses. *Journal of Magnetic Resonance (1969)*, 81(2):423–429, feb 1989.

- [82] A. C. Riiser and F Ravndal. Behavior of the Lieb-Mattis spin-degeneracy theorem with periodic boundary conditions. *Phys. Rev. B*, 48(8):5648–5649, aug 1993.
- [83] Joshua A. Folk, C M Marcus, R Berkovits, I L Kurland, I L Aleiner, and B L Altshuler. Ground State Spin and Coulomb Blockade Peak Motion in Chaotic Quantum Dots. *Physica Scripta*, T90(1):26, 2001.
- [84] S. Lindemann, T. Ihn, T. Heinzel, W. Zwerger, K. Ensslin, K. Maranowski, and A. C. Gossard. Stability of spin states in quantum dots. *Physical Review B*, 66(19):195314, nov 2002.
- [85] Russell J. Boyd. A quantum mechanical explanation for Hund’s multiplicity rule. *Nature*, 310(5977):480–481, aug 1984.
- [86] Philippe Durand and Jean-Claude Barthelat. A theoretical method to determine atomic pseudopotentials for electronic structure calculations of molecules and solids. *Theoretica Chimica Acta*, 38(4):283–302, 1975.
- [87] Jean Paul Malrieu, Rosa Caballol, Carmen J. Calzado, Coen de Graaf, and Nathalie Guihéry. Magnetic Interactions in Molecules and Highly Correlated Materials: Physical Content, Analytical Derivation, and Rigorous Extraction of Magnetic Hamiltonians. *Chemical Reviews*, 114(1):429–492, jan 2014.
- [88] C. H. Yang, A. Rossi, R. Ruskov, N. S. Lai, F. A. Mohiyaddin, S. Lee, C. Tahan, G. Klimeck, A. Morello, and A. S. Dzurak. Spin-valley lifetimes in a silicon quantum dot with tunable valley splitting. *Nat. Commun.*, 4(May):1–17, jun 2013.
- [89] Stephanie M Reimann and Matti Manninen. Electronic structure of quantum dots. *Rev. Mod. Phys.*, 74(4):1283–1342, nov 2002.

- [90] Erik Nielsen, Edwin Barnes, J. P. Kestner, and S. Das Sarma. Six-electron semiconductor double quantum dot qubits. *Phys. Rev. B*, 88:195131, Nov 2013.
- [91] A. P. Higginbotham, F. Kuemmeth, M. P. Hanson, A. C. Gossard, and C. M. Marcus. Coherent Operations and Screening in Multielectron Spin Qubits. *Physical Review Letters*, 112(2):026801, jan 2014.
- [92] Yoko Hada and Mikio Eto. Electronic states in silicon quantum dots: Multivalley artificial atoms. *Phys. Rev. B*, 68(15):155322, oct 2003.
- [93] A linear geometry was the most practical choice to study the minimum conditions under which negative exchange energy occurs in a multielectron quantum dot. Alternatively, *a triangular system would have been more general from a theoretical point of view and could have led to interesting physics. However, the inclusion of an extra tunnel coupling would bring in additional effects such as superexchange that would likely obscure the negative exchange phenomenon that we are targeting in our analysis. Moreover, a system of three quantum dots with tunnel coupling between every pair of dots is not desirable from the point of view of quantum computing architectures, where square lattices are needed to implement quantum error correcting surface codes.*
- [94] Kuangyin Deng and Edwin Barnes. Interplay of exchange and superexchange in triple quantum dots. *Phys. Rev. B*, 102:035427, Jul 2020.
- [95] Takumi Ito, Tomohiro Otsuka, Takashi Nakajima, Matthieu R. Delbecq, Shinichi Amaha, Jun Yoneda, Kenta Takeda, Akito Noiri, Giles Allison, Arne Ludwig, Andreas D. Wieck, and Seigo Tarucha. Four single-spin rabi oscillations in a quadruple quantum dot. *Applied Physics Letters*, 113(9):093102, 2018.
- [96] T. F. Watson, S. G. J. Philips, E. Kawakami, D. R. Ward, P. Scarlino, M. Veldhorst, D. E. Savage, M. G. Lagally, Mark Friesen, S. N. Coppersmith, M. A. Eriksson, and

- L. M. K. Vandersypen. A programmable two-qubit quantum processor in silicon. *Nature*, 555(7698):633–637, 2018.
- [97] David M Zajac, Anthony J Sigillito, Maximilian Russ, Felix Borjans, Jacob M Taylor, Guido Burkard, and Jason R Petta. Resonantly driven cnot gate for electron spins. *Science*, 359(6374):439–442, 2018.
- [98] A. R. Mills, D. M. Zajac, M. J. Gullans, F. J. Schupp, T. M. Hazard, and J. R. Petta. Shuttling a single charge across a one-dimensional array of silicon quantum dots. *Nature Communications*, 10(1):1063, 2019.
- [99] AJ Sigillito, JC Loy, DM Zajac, MJ Gullans, LF Edge, and JR Petta. Site-selective quantum control in an isotopically enriched si 28/si 0.7 ge 0.3 quadruple quantum dot. *Physical Review Applied*, 11(6):061006, 2019.
- [100] W. Huang, C. H. Yang, K. W. Chan, T. Tantt, B. Hensen, R. C. C. Leon, M. A. Fogarty, J. C. C. Hwang, F. E. Hudson, K. M. Itoh, A. Morello, A. Laucht, and A. S. Dzurak. Fidelity benchmarks for two-qubit gates in silicon. *Nature*, 569(7757):532–536, 2019.
- [101] Yadav P Kandel, Haifeng Qiao, Saeed Fallahi, Geoffrey C Gardner, Michael J Manfra, and John M Nichol. Coherent spin-state transfer via heisenberg exchange. *Nature*, 573(7775):553–557, 2019.
- [102] Juan P. Dehollain, Uditendu Mukhopadhyay, Vincent P. Michal, Yao Wang, Bernhard Wunsch, Christian Reichl, Werner Wegscheider, Mark S. Rudner, Eugene Demler, and Lieven M. K. Vandersypen. Nagaoka ferromagnetism observed in a quantum dot plaquette, 2019.
- [103] W. I. L. Lawrie, H. G. J. Eenink, N. W. Hendrickx, J. M. Boter, L. Petit, S. V.

- Amitonov, M. Lodari, B. Paquelet Wuetz, C. Volk, S. G. J. Philips, and et al. Quantum dot arrays in silicon and germanium. *Applied Physics Letters*, 116(8):080501, Feb 2020.
- [104] J. J. Viennot, M. C. Dartiailh, A. Cottet, and T. Kontos. Coherent coupling of a single spin to microwave cavity photons. *Science*, 349(6246):408–411, 2015.
- [105] N. Samkharadze, G. Zheng, N. Kalhor, D. Brousse, A. Sammak, U. C. Mendes, A. Blais, G. Scappucci, and L. M. K. Vandersypen. Strong spin-photon coupling in silicon. *Science*, 359(6380):1123–1127, 2018.
- [106] X. Mi, M. Benito, S. Putz, D. M. Zajac, J. M. Taylor, Guido Burkard, and J. R. Petta. A coherent spin–photon interface in silicon. *Nature*, 555(7698):599–603, 2018.
- [107] A. J. Landig, J. V. Koski, P. Scarlino, U. C. Mendes, A. Blais, C. Reichl, W. Wegscheider, A. Wallraff, K. Ensslin, and T. Ihn. Coherent spin–photon coupling using a resonant exchange qubit. *Nature*, 560(7717):179–184, 2018.
- [108] Timothy Alexander Baart, Takafumi Fujita, Christian Reichl, Werner Wegscheider, and Lieven Mark Koenraad Vandersypen. Coherent spin-exchange via a quantum mediator. *Nature Nanotechnology*, 12(1):26–30, 2017.
- [109] X.G. Croot, S.J. Pauka, J.D. Watson, G.C. Gardner, S. Fallahi, M.J. Manfra, and D.J. Reilly. Device architecture for coupling spin qubits via an intermediate quantum state. *Phys. Rev. Applied*, 10:044058, Oct 2018.
- [110] Erik Nielsen, Ralph W Young, Richard P Muller, and MS Carroll. Implications of simultaneous requirements for low-noise exchange gates in double quantum dots. *Physical Review B*, 82(7):075319, 2010.
- [111] Qiuzi Li, Łukasz Cywiński, Dimitrie Culcer, Xuedong Hu, and S Das Sarma. Exchange

- coupling in silicon quantum dots: Theoretical considerations for quantum computation. *Physical Review B*, 81(8):085313, 2010.
- [112] Jesper Pedersen, Christian Flindt, Niels Asger Mortensen, and Antti-Pekka Jauho. Failure of standard approximations of the exchange coupling in nanostructures. *Phys. Rev. B*, 76:125323, Sep 2007.
- [113] M Stopa and CM Marcus. Magnetic field control of exchange and noise immunity in double quantum dots. *Nano letters*, 8(6):1778–1782, 2008.

Appendices

Appendix A

Single-particle densities and mediator detuning values

In this appendix, we show additional plots of the single-particle density for cases 2, 3 and 4, for both the lowest-energy singlet-like (S) and triplet-like (T) eigenstates with total spin projection $S_z^{total} = 0$. We also provide further details about the way we choose our potential cuts and detuning values Δ to guarantee the mediator contains the desired number of electrons in each case.

A.1 Triangular triple dot with two electrons (case 2)

In this case, the potential cut between D1 and D2 is always the half-line, $x = 0, y < y_0$, and the horizontal line, $y = y_0$. For the latter, we choose different values of y_0 depending on the angle we choose. For $\alpha = 30^\circ, 40^\circ, 45^\circ, 50^\circ$, we set $y_0 = 6, 10, 12, 15$ nm, respectively. For the larger angles, we do the following. First we choose the detuning, Δ , and then determine the equal-potential point on the line connecting D1 and D3. Due to symmetry, we can find a similar point on the line connecting D2 and D3. We then connect these two points by a line, which gives us the $y = y_0$ cut. The reason we do not use this procedure for smaller angles is because the big dot is very close to the x -axis, and the equal-potential point is too close to the small dots in these cases, and so placing the cut here would leave the small dots with

too much overlap in the big dot region.

We set the detuning on D3 to a high value, $\Delta = 20$ meV, to deplete the mediator as much as possible. The tolerance threshold for the electron number on D3 is set as discussed in Sec. 5.3. The corresponding single-particle density plots for several different angles are shown in Fig. A.1. The three dot potentials are marked by white and blue dashed circles, and the potential cut $y = y_0$ is indicated by a yellow dashed line. It is evident that the mediator remains empty in all cases.

A.2 Triangular triple dot with four electrons (case 3)

Here, we do the same potential cuts as in case 2. To determine appropriate choices for the detuning Δ , we perform a systematic scan over Δ values, in each case calculating how many electrons are in the big dot region above $y = y_0$. We find that the following values correspond to having two electrons in the big dot: $\Delta = 1.0, -1.0, -1.5, -2.0, 3.5, 4.0, 4.0, 4.0, 4.0, 4.0, 4.0, 4.0$ meV for $\alpha = 30^\circ, 40^\circ, 45^\circ, 50^\circ, 60^\circ, 64^\circ, 68^\circ, 70^\circ, 72^\circ, 74^\circ, 76^\circ, 80^\circ$, respectively.

We show several density plots for various values of α in Fig. A.2. The three dots are illustrated by the blue dashed circles, and the potential cut at $y = y_0$ is indicated by the yellow dashed line. One can see that the shifts in the positions of the electrons in the big dot are much larger at lower angles, which agrees with the analysis in Sec. 5.5 and Fig. 5.9.

A.3 Linear triple dot with four electrons (case 4)

In this case, we make two potential cuts ($x = \pm x_0$) parallel to the y -axis. To do this, we first choose the detuning Δ for D3, and then compute the equal-potential point $(x_0, 0)$ between

D2 and D3. Thus, we can separate the space into three parts using the two cuts $x = \pm x_0$.

To decide the detunings Δ , we again scan over a range of values and integrate the density to see how many electrons are in the big dot region (middle region). This process yields the following values at which two electrons are confined to D3: $\Delta = -0.5, 0.0, 0.0, 0.0, 0.0, 0.0, 2.0, 3.0, 3.5, 3.5, 3.5, 3.5$ meV for $\alpha = 30^\circ, 35^\circ, 40^\circ, 45^\circ, 50^\circ, 55^\circ, 60^\circ, 64^\circ, 68^\circ, 70^\circ, 72^\circ, 80^\circ$, respectively.

Single-particle density plots for several different values of α are shown in Fig. A.3. The three dots are illustrated by the blue dashed circles, and the potential cuts at $x = \pm x_0$ are indicated by the yellow dashed lines.

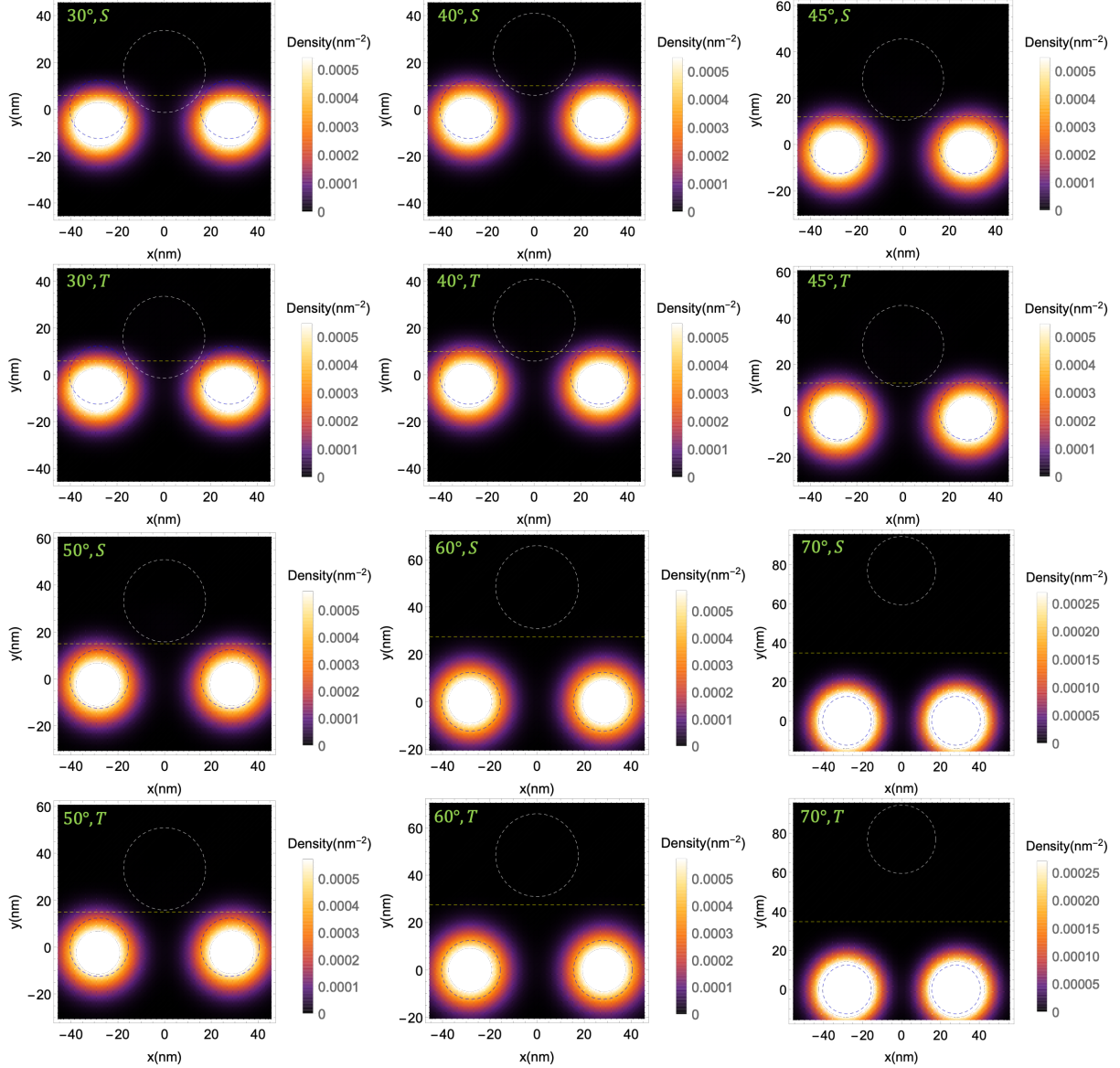


Figure A.1: Single-particle density plots for the triangular triple dot with two electrons (case 2) for $\alpha = 30^\circ, 40^\circ, 45^\circ, 50^\circ, 60^\circ, 70^\circ$ and for the lowest-energy singlet-like (S) and triplet-like (T) states. The white and blue dashed circles indicate the dot potentials, and the yellow dashed line is the potential cut (here we do not show the $x = 0$ cut in the plots). The big dot contains approximately zero electrons. At low angles, the two small dots move a little bit downward due to the large detuning of the big dot. At high angles, this effect is small because the dots are sufficiently far apart.

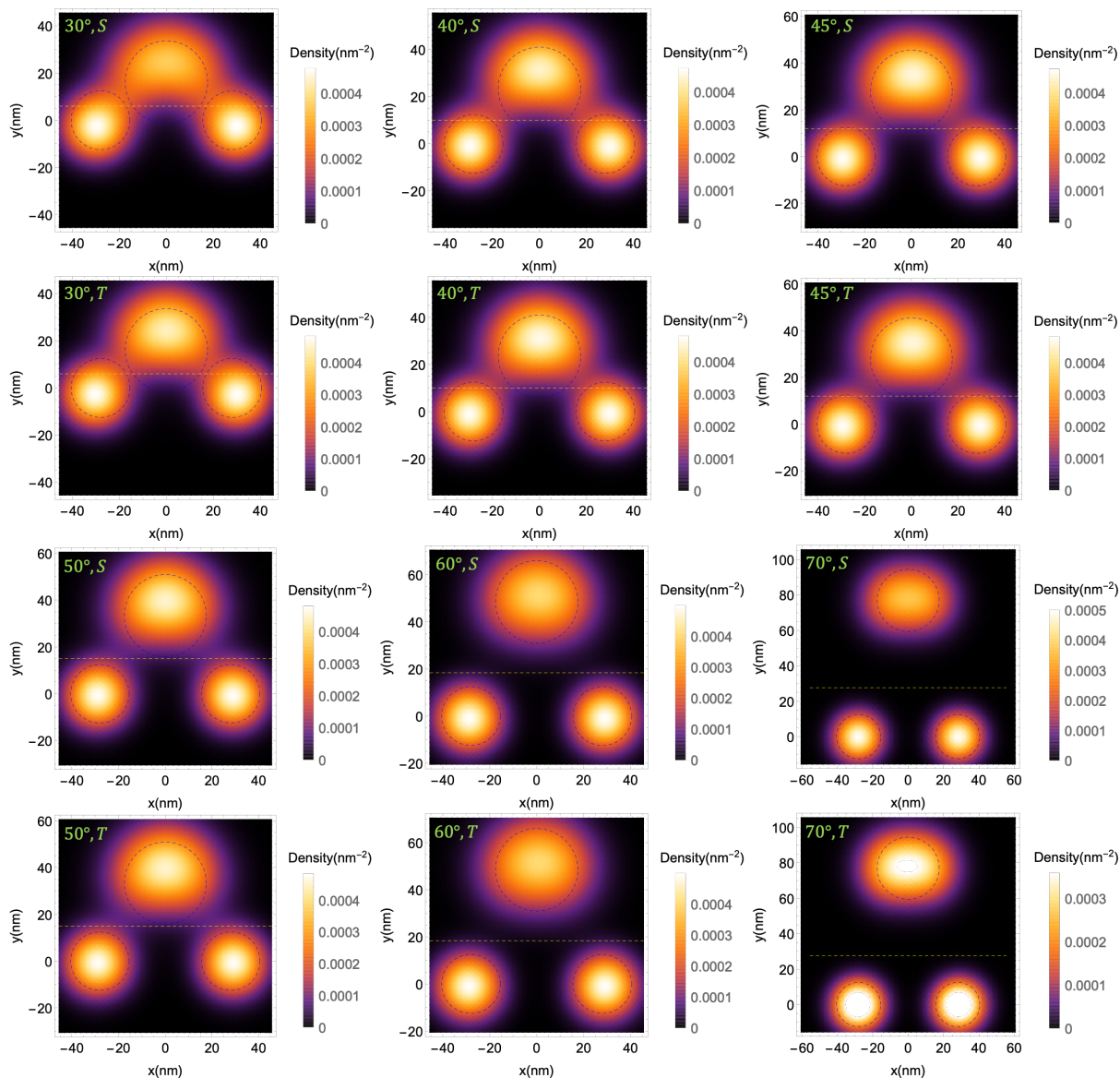


Figure A.2: Single-particle density plots for the triangular triple dot with four electrons (case 3) for $\alpha = 30^\circ, 40^\circ, 45^\circ, 50^\circ, 60^\circ, 70^\circ$ and for the lowest-energy singlet-like (S) and triplet-like (T) states. The white and blue dashed circles indicate the dot potentials, and the yellow dashed line is the potential cut (here we do not show the $x = 0$ cut in the plots). In each case, the big dot contains two electrons as can be confirmed by integrating the density over the upper region. The position shifts of the electrons in the big dot are significantly larger for smaller angles compared to larger angles, which confirms the results obtained in Sec. 5.5 and Fig. 5.9.

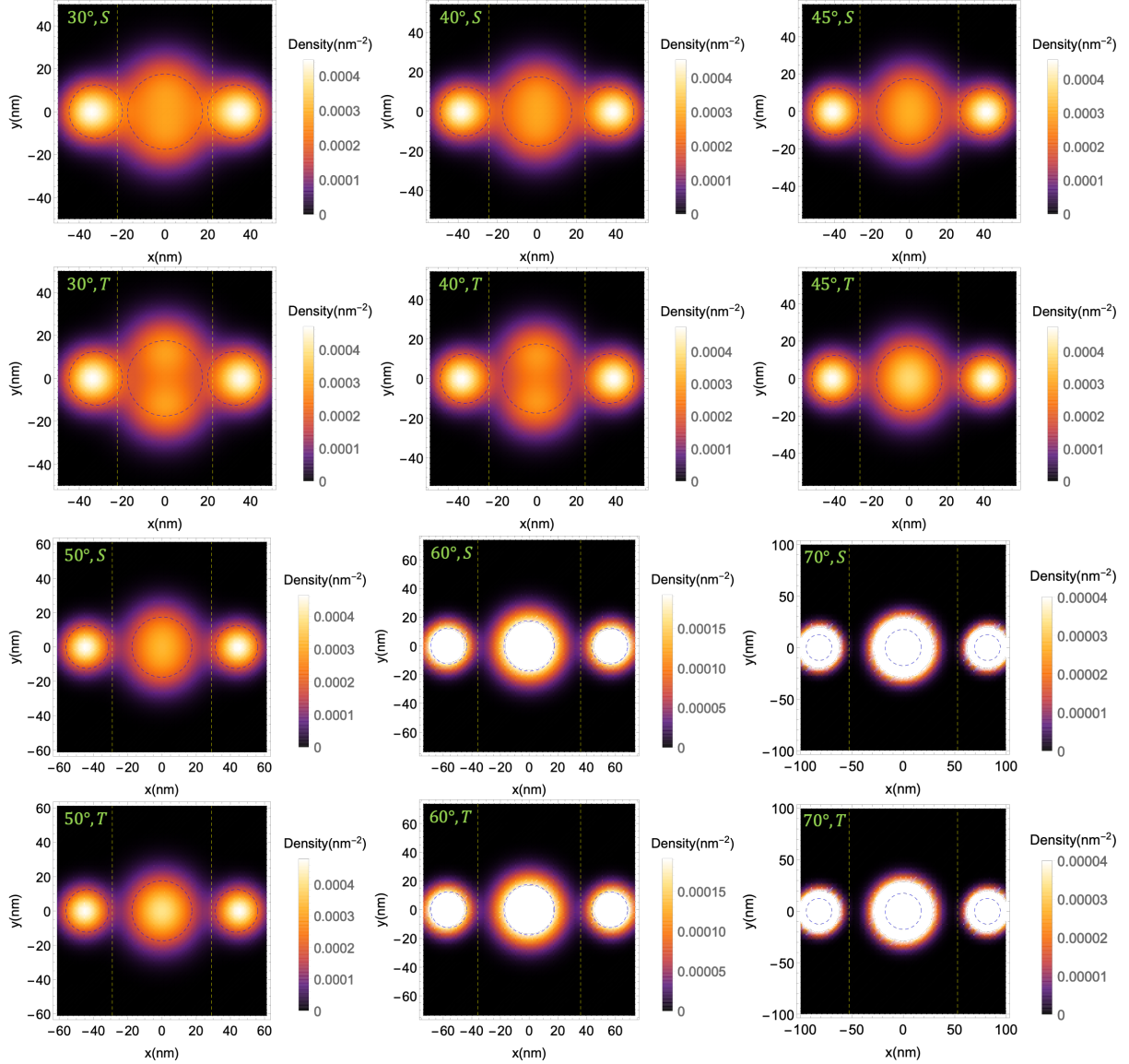


Figure A.3: Single-particle density plots for the linear triple dot with four electrons (case 4) for $\alpha = 30^\circ, 40^\circ, 45^\circ, 50^\circ, 60^\circ, 70^\circ$ and for the lowest-energy singlet-like (S) and triplet-like (T) states. The blue dashed circles indicate the dot potentials, and the yellow dashed lines are the potential cuts. The big dot contains two electrons as can be confirmed by integrating the density over the middle region.